Non-affine lattice dynamics of disordered solids

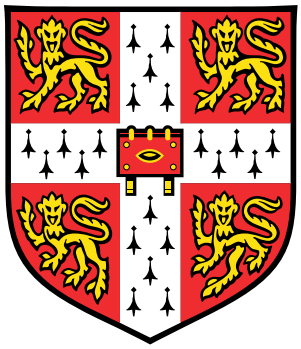

Johannes Krausser

Sidney Sussex College
University of Cambridge

This dissertation is submitted for the degree of
Doctor of Philosophy

November 2017

Declaration

This dissertation is the result of my own work and includes nothing which is the outcome of work done in collaboration except as declared in the Preface and specified in the text.

It is not substantially the same as any that I have submitted, or, is being concurrently submitted for a degree or diploma or other qualification at the University of Cambridge or any other University or similar institution except as declared in the Preface and specified in the text. I further state that no substantial part of my dissertation has already been submitted, or, is being concurrently submitted for any such degree, diploma or other qualification at the University of Cambridge or any other University or similar institution except as declared in the Preface and specified in the text It does not exceed the prescribed word limit of 65,000 words including appendices, bibliography, footnotes, tables and equations and has fewer than 150 figures.

1. J. Krausser, R. Milkus, & A. Zaccone, *Non-affine lattice dynamics of defective fcc crystals*, Soft Matter, 13, 6079-6089 (2017);

2. J. Krausser, R. Milkus, & A. Zaccone, *Elastic correlations in depleted spring networks with long-range interactions*, preprint (2017);

3. J. Krausser, V. Palyulin, R. Milkus, & A. Zaccone, *Approximation of the viscoelastic response of multicomponent disordered solids*, preprint (2017);

4. J. Krausser, K. Samwer, & A. Zaccone. *Interatomic repulsion softness directly controls the fragility of supercooled metallic melts* . Proceedings of the National Academy of Sciences, 112 (45), 13762-13767 (2015).

I have contributed to all aspects of research for papers 1-4. Paper 2 is also part of the PhD thesis of Rico Milkus submitted at the University of Cambridge. The simulations in Paper 3 were carried out by Vladimir Palyulin.

Johannes Krausser
November 2017

Abstract

This thesis provides a study of different aspects of the mechanical and vibrational properties of disordered and amorphous solids. Resorting to the theoretical framework of non-affine lattice dynamics the attention is focused on the analysis of disordered networks and lattices which serve as tractable model systems for real materials.

Firstly, we discuss the static elastic response and the vibrational spectra of defective fcc crystals. The connection to different types of microstructural disorder in the form of bond-depletion and vacancies is described within the context of the inversion symmetry breaking of the local particle configurations. We identify the fluctuations of the local inversion symmetry breaking, which is directly linked to the non-affinity of the disordered solid, as the source of different scalings behaviours of the position of the boson peak. Furthermore, we describe the elastic heterogeneities occurring in a bond-depleted two-dimensional lattice with long-range interactions. The dependence of the concomitant correlations of the local elastic moduli are studied in detail in terms of the interaction range and the degree of disorder. An analytical scaling relation is derived for the radial part of the elastic correlations in the affine limit. Subsequently, we provide an argument for the change of the angular symmetry of the elastic correlation function which was observed in simulations and experiments on glasses and colloids, respectively.

Moving to the dynamical behaviour of disordered solids, a framework is developed based on the kernel polynomial method for the approximate computation of the non-affine correlator of displacement fields which is the key requirement to describe the linear viscoelastic response of the system within the quasi-static non-affine formalism. This approach is then extended to the case of multicomponent polymer melts and validated against molecular dynamics simulations at low non-zero temperatures.

We also consider the dynamical behaviour of metallic glasses in terms of its shear elasticity and viscosity. A theoretical scheme is suggested which links the repulsive strength of the interatomic potential to the viscoelasticity and fragility in metallic glasses in the quasi-affine limit.

Table of contents

List of figures

List of tables

Chapter 1

Introduction

Understanding the physical mechanisms which govern the effect of disorder on the mechanical and vibrational properties of disordered solids, as supercooled liquids, defective lattices, and glasses remains a long-standing research effort. A comprehensive theoretical description of the transition from the rigid to the mechanically unstable state based on the microscopic dynamics is still lacking. The absence of long-range order and periodicity in these amorphous systems makes a theoretical description a formidable task. The situation for disordered lattice systems is slightly better. Theoretical tools like effective-medium theories, which aim to map the problem of describing the mechanical and vibrational properties of a disordered non-periodic lattice to a ordered, periodic lattice with a complex-valued elastic response, have proved very successful throughout the past decades. Even though there exists a large body of literature concerned with the study of the vibrational and elastic properties of disordered lattices, they remain a source of rich physical phenomena in terms of their vibrational dynamics, elastic response and elastic-to-plastic transition.

A more direct approach, based on characterising the microscopic particle trajectories in disordered solids under external stress was established about a decade ago [57]. This framework exhibits a remarkable strength in explaining physical phenomena observed in molecular-dynamics simulation and experiments of amorphous matter related to local particle displacements and rearrangements from a microscopic point of view. The starting point for describing the elastic response of a disordered particle system to external stress is the idea to distinguish two fundamentally different types of microscopic displacements. The first corresponds to homogeneous displacements as they would be observed in a uniform solid as a response to external stress which are therefore called affine displacements. The second form of displacements are deviations from these affine trajectories due to microscopic non-uniformities in the solid, which are connected to

collective rearrangements of particles eventually governing the pathways leading to plasticity. We will describe the mechanism behind these non-affine motions later in this chapter in more detail. A fundamental part in order to establish a theoretical framework for describing the non-affinity in a quasi-static zero-temperature setting is the harmonic approximation of the particle interactions in the disordered solid.

To the end of setting up the framework of non-affine particle trajectories and to work out the consequences for linear viscoelastic response of the disordered solid, we will start by reviewing the harmonic approximation of potentials with constitute the microscopic interaction between particles.

1.1 The harmonic approximation

Consider a system of N interacting particles in d dimensions. For the time being we make the assumption that the interactions between the individual particles are pair-wise and central-force interactions. The configuration of the systems is given by the positions $\boldsymbol{R} = \{\boldsymbol{r}_1, \ldots, \boldsymbol{r}_N\}$ and momenta $\boldsymbol{P} = \{\boldsymbol{p}_1, \ldots, \boldsymbol{p}_N\}$ of all particles. In order to write down the equation of motion of this system and describe its dynamics we have to specify the kinetic and potential energy of the system. This is done by writing down the Hamiltonian of the N-particle system [4], i.e.

$$\mathcal{H}(\boldsymbol{P}, \boldsymbol{R}) = \sum_i \frac{\boldsymbol{p}_i^2}{2m_i} + U(\boldsymbol{R}). \tag{1.1}$$

In the harmonic approximation we assume that the displacements of the particles from their equilibrium positions are small so that an approximation of the interaction energy up to second order in the particle displacements away from their equilibrium positions provides a valid description of the system. We will denote the position of the ℓ^{th} particles by $\boldsymbol{r}(\ell) = \boldsymbol{r}_{0,\ell} + \delta\boldsymbol{r}_\ell$. Here, $\boldsymbol{r}_{0,\ell} = \boldsymbol{r}_0(\ell)$ denotes the equilibrium position of the ℓ^{th} particle and its displacement from equilibrium is $\delta\boldsymbol{r}(\ell) = \delta\boldsymbol{r}_\ell$. The potential energy of the system is given in terms of the pair-wise central-force interactions between the particles

$$U(\boldsymbol{R}) = \frac{1}{2}\sum_{\langle i,j\rangle} V(r_{ij}) = \frac{1}{2}\sum_{\langle i,j\rangle} V(|\boldsymbol{r}_{0,i} - \boldsymbol{r}_{0,j} + \delta\boldsymbol{r}_i - \delta\boldsymbol{r}_j|) \tag{1.2}$$

where $\langle i,j\rangle$ denotes the summation over interacting pairs of particles and $r_{ij} = |\boldsymbol{r}_i - \boldsymbol{r}_j|$. In order to invoke the harmonic approximation we expand the interaction potential V with respect to the displacement fields and neglect all terms higher than second order.

The Taylor expansion of the interaction potential up to second order takes the form

$$V(\boldsymbol{r}_0 + \delta\boldsymbol{r}) = v(\boldsymbol{r}) + (\delta\boldsymbol{r} \cdot \nabla)\, V(\boldsymbol{r}_0) + \frac{1}{2}\,(\delta\boldsymbol{r} \cdot \nabla)^2\, V(\boldsymbol{r}_0) + \dots \tag{1.3}$$

which we use to obtain the harmonic approximation of the potential energy U as [4, 57]

$$U(\boldsymbol{R}) = U(\boldsymbol{r}_0) + \frac{1}{2}\sum_{\langle i,j\rangle} V'(r_{0,ij})\hat{\boldsymbol{n}}_{0,ij} \cdot \delta\boldsymbol{r}_{ij} + \frac{1}{4}\sum_{\langle i,j\rangle} \delta\boldsymbol{r}_{ij}\mathbf{M}_{ij}\delta\boldsymbol{r}_{ij} + \mathcal{O}(\delta\boldsymbol{r}^3) \tag{1.4}$$

where the $d \times d$ block matrix $\mathbf{M}_{ij}$ is given by

$$\begin{aligned} M_{ij} =& \left[V''(r_{0,ij}) - \frac{V'(r_{0,ij})}{r_{0,ij}}\right]\hat{\boldsymbol{n}}_{ij}^T\hat{\boldsymbol{n}}_{ij} + \frac{V'(r_{0,ij})}{r_{0,ij}}\mathbb{1} \\ =& \left[c_{ij} - \frac{t_{ij}}{r_{0,ij}}\right]\hat{\boldsymbol{n}}_{ij}^T\hat{\boldsymbol{n}}_{ij} + \frac{t_{ij}}{r_{0,ij}}\mathbb{1}. \end{aligned} \tag{1.5}$$

where we have introduced the bond tension t_ij the bond stiffness c_{ij} defined as

$$\begin{aligned} t_{ij} =& \left.\frac{\partial V(r_{ij})}{\partial r_{ij}}\right|_{r_{ij}=r_{0,ij}} = V'(r_{0,ij}) \\ c_{ij} =& \left.\frac{\partial^2 V(r_{ij})}{\partial r_{ij}^2}\right|_{r_{ij}=r_{0,ij}} = V''(r_{0,ij}). \end{aligned} \tag{1.6}$$

In the last step the unit bond vector $\hat{\boldsymbol{n}}_{ij} = \boldsymbol{r}_{0,ij}/r_{0,ij}$ was introduced. Since the matrix $\mathbf{M}_{ij}$ is symmetric we can simplify the above expression and obtain

$$U(\boldsymbol{r}) = U(\boldsymbol{r}_0) - \sum_i \boldsymbol{f}_i \cdot \delta\boldsymbol{r}_i + \frac{1}{2}\sum_{\langle i,j\rangle} \delta\boldsymbol{r}_i\mathbf{H}_{ij}\delta\boldsymbol{r}_j \tag{1.7}$$

where $\mathbf{H}$ represents the $dN \times dN$-dimensional Hessian or dynamical matrix given in terms of $\mathbf{M}$ as [57]

$$\mathbf{H}_{ij} = \delta_{ij}\sum_{k\neq i}\mathbf{M}_{ik} - \mathbf{M}_{ij} \tag{1.8}$$

and the force $\boldsymbol{f}_i$ acting on particle i is

$$\boldsymbol{f}_i = \sum_{j\neq i} V'(r_{0,ij})\hat{\boldsymbol{n}}_{ij} \tag{1.9}$$

which are zero in mechanical equilibrium. Effectively, the Hessian describes the local curvatures of the potential energy landscape of the system.

1.2 Normal modes and vibrational density of states

Having specified the Hamiltonian of the interacting particle system we can now write down the resulting Newtonian equation of motion for the displacement in the harmonic approximation

$$m_i \frac{\partial^2 \delta r_i^\alpha}{\partial t^2} = -\sum_{j,\beta} H_{ij}^{\alpha\beta} \delta r_j^\beta \tag{1.10}$$

With the expectation in mind that the displacements of the particles are oscillatory motions with a given frequency ω, we transform the equation of motion to mass-dependent displacement fields [12]

$$\delta r_i^\alpha = \frac{u_i^\alpha}{\sqrt{m_i}} \mathrm{e}^{i\omega t}, \tag{1.11}$$

thereby introducing the dynamical matrix

$$D_{ij}^{\alpha\beta} = \frac{H_{ij}^{\alpha\beta}}{\sqrt{m_i m_j}}. \tag{1.12}$$

In the transformed coordinate system the equation of motion Eq. (1.10) reduces to the eigenvalue problem [20]

$$\omega_p^2 u_{p,i}^\alpha = \sum_{j,\beta} D_{ij}^{\alpha\beta} u_{p,j}^\beta \tag{1.13}$$

where the eigenvalues $\lambda_p = \omega_p^2$ denote the eigenvalue of the dynamical matrix. Consequently, the normal modes $\boldsymbol{u}_p = (\boldsymbol{u}_{p,1}, \ldots, \boldsymbol{u}_{p,N})$ represent the vibrational modes a system can sustain at a given eigenfrequency ω_p. In crystalline systems without disorder, these normal modes correspond to plane-wave vibrational excitations called phonons.

The distribution of eigenfrequencies of the dynamical matrix $\mathbf{D}$, the vibrational density of states (vDOS) is defined as

$$\rho(\omega) = \frac{1}{dN} \sum_{p=1}^{dN} \delta(\omega - \omega_p) \tag{1.14}$$

In a crystalline system, the periodicity of the underlying lattice can be used to simplify the dynamical matrix from its full $dN \times dN$-dimensional form to its $d \times d$ periodic representation, from which for some lattice geometries the vDOS $\rho(\omega)$ can be calculated analytically [27]. However, in the presence of random disorder, for example a disordered

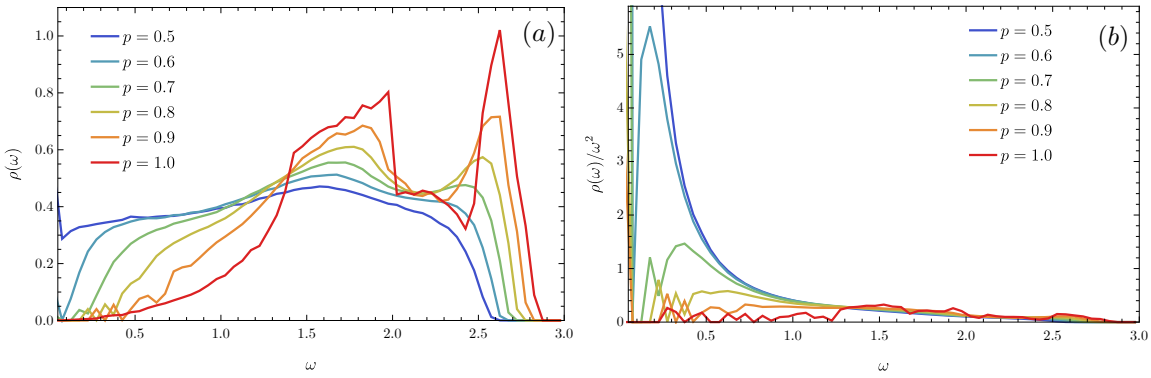

Fig. 1.1 (a) The vibrational density of states of a 3D fcc crystal as the average coordination is reduce as $\bar{Z} = pZ_0$. (b) The reduced density of states $\rho(\omega)/\omega^2$ for the same system showing clearly the excess of vibrational modes with respect to the Debye sclaing $\sim \omega^2$.

lattice, the periodicity of the lattice cannot be used. Therefore, in general, for a disordered solid an analytical solution of the eigenvalue problem s not possible and we have to resort to numerical methods to find the eigenfrequencies and eigenvectors of the disordered.

In Fig. 1.1 (a) we show the evolution of the vDOS of a three-dimensional fcc lattice under the influence of random bond cutting. In the perfect lattice each particle interacts with its $Z_0 = 12$ nearest neighbours. As bonds are randomly removed from the lattice with probability $1 - p$, the average number of neighbours, or coordination number, decreases to the value $\bar{Z} = pZ_0$. One of the striking feature of the vibrational density of states of a disordered system, termed the boson peak, is the excess of low-frequency modes with respect to the Debye scaling $\rho_{\mathrm{D}}(\omega) \propto \omega^2$, which is found to hold in the perfect fcc lattice at $p = 1$. This phenomenon is best visualised by considering the reduced density of states $\rho(\omega)/\omega^2$ as plotted in Fig. 1.1 (b). Evidently, the intensity of the peak of excess low-frequency modes strongly increases when decreasing p. The peak position of the boson peak moves to lower values linearly in p as more and more bonds are removed from the lattice. In addition, we can clearly see how the van Hove singularities are smoothed out by the presence of disorder.

1.3 Equations of motion of non-affine lattice dynamics

With a first look at the anomalous vibrational properties of disordered solids, we now want to focus the attention to the theoretical framework which we will use to describe the elastic properties of an amorphous or disordered system. We will see that the distribution

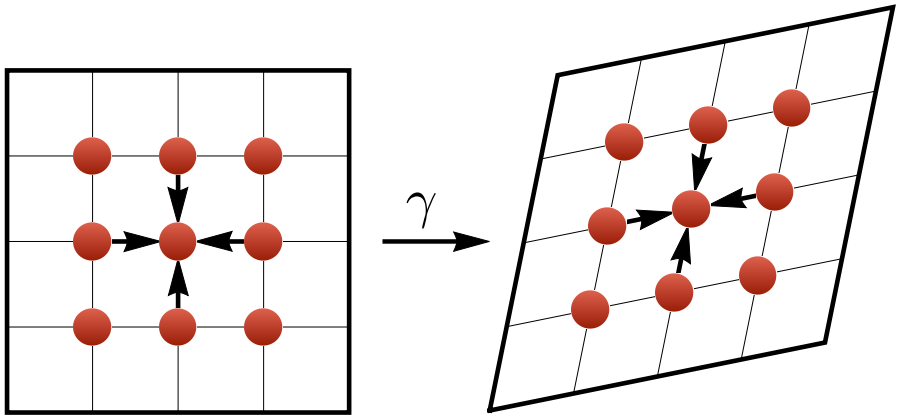

Fig. 1.2 Pure shear deformation of a inversion-symmetric crystalline lattice with shear angle γ.

of vibrational eigenfrequencies characterised by $\rho(\omega)$ plays a crucial role in understanding the elasticity of disordered solids.

If a perfectly crystalline system at zero temperature is subjected to a small external strain γ, such as shear or compression, the particles in the solid will undergo a homogeneous displacement following the external macroscopic strain. These displacements are called affine displacements.

Starting from some reference configuration, denoted as $\boldsymbol{r}_0$ and applying pure shear of angle γ, the coordinate transformation between the initial and final configuration can be written as $\boldsymbol{r}_i = \mathbf{F} \cdot \boldsymbol{r}_{0,i}$. The matrix $\mathbf{F}$ represents the deformation gradient tensor for pure shear and is defined as

$$\mathbf{F} = \begin{pmatrix} \cos(\gamma/2) & \sin(\gamma/2) & 0 \\ \sin(\gamma/2) & \cos(\gamma/2) & 0 \\ 0 & 0 & 1 \end{pmatrix}. \tag{1.15}$$

This situation in depicted in Fig. 1.2. Both the reference configuration $\boldsymbol{r}_0$ and the final affine configuration $\boldsymbol{r}$ are in mechanical equilibrium. The forces on each particle before and after the shear deformation are balanced out by virtue of the inversion symmetry of the underlying centrosymmetric lattice. If the same transformation $\mathbf{F}$ is applied to a disordered solid, where the particles do not align on an inversion-symmetric lattice, we encounter a different situation. As depicted in Fig. 1.3, initially the particles occupy random position are in mechanical equilibrium. This means that the forces acting on the central particle sum to zero in the disordered equilibrium configuration. Applying the pure shear transformation of the particle system displaces each particle to its affine position. However, the system is not in equilibrium anymore. In this new configuration

the forces on the central particle, for instance, do not cancel due to the lack of local particle symmetry. In order to reach the mechanical equilibrium of the deformed configuration these residual forces have to be relaxed. Consequently, the particles move away from the affine position and the system relaxes to its final equilibrium configuration. These equilibrium positions are the non-affine positions which in Fig. 1.3 are shown as dashed circles. Clearly, due to the randomness of the disordered configuration, the relaxation of the particles to the equilibrium positions cannot be described by the action of a linear map like the deformation gradient tensor $\mathbf{F}$, which is why they are called non-affine displacements.

We can set up the non-affine quasi-static formalism by considering the action of $\mathbf{F}$. After the shear deformation of the reference configuration $\boldsymbol{r}_0$, the affine configuration is given by $\boldsymbol{r}_i = \mathbf{F}(\gamma)\boldsymbol{r}_{0,i}$. Since we want to incorporate the resulting non-affine correction, we generalise this relation by making the reference configuration γ-dependent, i.e.

$$\boldsymbol{r}_i(\gamma) = \mathbf{F}(\gamma)\mathring{\boldsymbol{r}}_i(\gamma) \tag{1.16}$$

where the new variable $\mathring{\boldsymbol{r}}_i$ tracks the non-affine displacements in the undeformed configuration. This means that keeping $\mathring{\boldsymbol{r}}_i(\gamma)$ fixed and changing $\mathbf{F}(\gamma)$ corresponds to the affine part of the deformation, whereas keeping $\mathbf{F}(\gamma)$ constant and varying $\mathring{\boldsymbol{r}}_i(\gamma)$ results in the non-affine correction. The potential energy of the system is then a function of the shear angle γ and the non-affine coordinates $U(\boldsymbol{r}(\gamma)) = U(\mathring{\boldsymbol{r}}, \gamma)$. In order to set up an equation of motion, we can implicitly define the trajectories of the non-affine displacements under the condition of mechanical equilibrium by requiring that the force acting on the particle $\boldsymbol{f}_i$ is zero [57]. This means that we require for all particles that

$$\boldsymbol{f}_i = -\left.\frac{\partial U}{\partial \mathring{\boldsymbol{r}}}\right|_{\gamma} (\mathring{\boldsymbol{r}}, \gamma) = 0 \tag{1.17}$$

be fulfilled [61]. The derivative is taken at fixed γ. Differentiating this equation with respect to the shear angle γ we arrive at the expression

$$\frac{\partial^2 U}{\partial \mathring{\boldsymbol{r}}_i \partial \mathring{\boldsymbol{r}}_j} \cdot \frac{\mathcal{D}\mathring{\boldsymbol{r}}_j}{\mathcal{D}\gamma} + \frac{\partial^2 U}{\partial \mathring{\boldsymbol{r}}_i \partial \gamma} = 0. \tag{1.18}$$

where the summation over the index j is implied and the differential operator $\mathcal{D}$ denotes differentiation under the condition of mechanical equilibrium reflecting the adiabatic approximation. This equation is the formal representation of the secondary non-affine relaxation mechanism explained above. The system is subjected to a infinitesimally

small affine transformation $\mathrm{d}\gamma$ first, and then corrections $\mathcal{D}\mathring{\boldsymbol{r}}_i$ are added to bring the configuration to mechanical equilibrium where $\boldsymbol{f}_i = 0$ holds [62].

Since we want to obtain the linear response of the system to an infinitesimal strain $\mathrm{d}\gamma$, we evaluate the above relation in the limit $\gamma \to 0$ [57]. We recognise that in this limit the double derivative in the first term in Eq. (1.18) represents the Hessian matrix since

$$\mathbf{H}_{ij} = \left.\frac{\partial^2 U}{\partial \mathring{\boldsymbol{r}}_i \partial \mathring{\boldsymbol{r}}_j}\right|_{\gamma\to 0} = \left.\frac{\partial^2 U}{\partial \boldsymbol{r}_i \partial \boldsymbol{r}_j}\right|_{r\to r_0} \tag{1.19}$$

since $\mathring{\boldsymbol{r}}(\gamma)|_{\gamma\to 0} = \boldsymbol{r}_0$. The second term in Eq. (1.18) can be identified as the force which the i^{th} particle experiences as the consequence of an infinitesimal affine deformation γ [57]. We thus introduce the affine force field $\boldsymbol{\Xi}_i$ by setting

$$\boldsymbol{\Xi}_i = -\left.\frac{\partial^2 U}{\partial \mathring{\boldsymbol{r}}_i \partial \gamma}\right|_{\gamma\to 0}. \tag{1.20}$$

With these definitions we can rewrite Eq. (1.18) as

$$\mathbf{H}\cdot\left.\frac{\mathcal{D}\mathring{\boldsymbol{r}}}{\mathcal{D}\gamma}\right|_{\gamma\to 0} = \boldsymbol{\Xi} \tag{1.21}$$

which, after removing the zero-modes of the Hessian can be expressed as

$$\left.\frac{\mathcal{D}\mathring{\boldsymbol{r}}}{\mathcal{D}\gamma}\right|_{\gamma\to 0} = \mathbf{H}^{-1}\cdot\boldsymbol{\Xi}. \tag{1.22}$$

The solutions of this equation define the tangents along which the non-affine displacements will be directed [61]. This represents the non-affine linear response of the system to the extra forces which appear by the infinitesimal affine transformation characterised by γ. We can subsequently linearise the relation $\boldsymbol{r}_i(\gamma) = \mathbf{F}(\gamma)\cdot\mathring{\boldsymbol{r}}_i(\gamma)$ in the linear response regime, which yields [80]

$$\begin{aligned}\boldsymbol{r}_i(\gamma) =& \mathring{\boldsymbol{r}}_i(0) + \left.\frac{\mathcal{D}}{\mathcal{D}\gamma}\left(\mathbf{F}(\gamma)\mathring{\boldsymbol{r}}_i(\gamma)\right)\right|_{\gamma\to 0}\gamma + \mathcal{O}(\gamma^2)\\ =& \mathring{\boldsymbol{r}}_i(0) + \left(\frac{\mathcal{D}}{\mathcal{D}\gamma}\mathbf{F}(\gamma)\right)\mathring{\boldsymbol{r}}_i(\gamma)\Big|_{\gamma\to 0}\gamma + \mathbf{F}(\gamma)\left(\frac{\mathcal{D}}{\mathcal{D}\gamma}\mathring{\boldsymbol{r}}_i(\gamma)\right)\Big|_{\gamma\to 0}\gamma + \mathcal{O}(\gamma^2).\end{aligned} \tag{1.23}$$

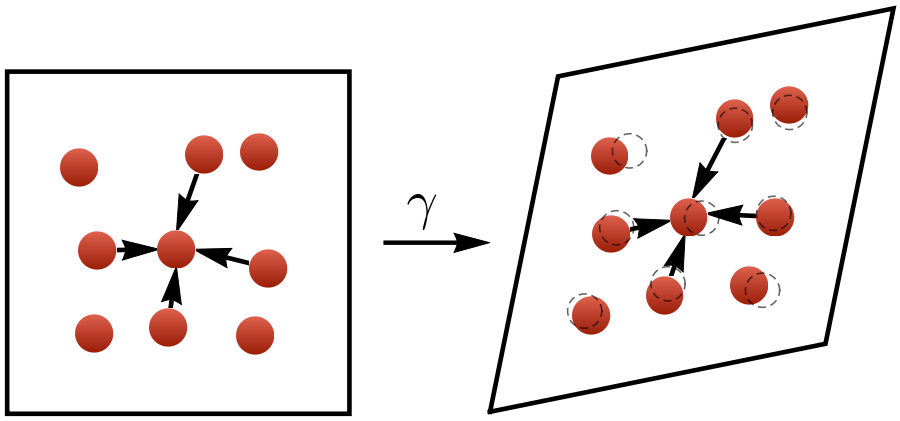

Fig. 1.3 Visualisation of the non-affine mechanism. Under a shear strain γ, the absence of local inversion symmetry leads to the appearance of excess forces which lead to non-affine displacements in addition to the affine deformation.

Using that $\mathbf{F}(0) = \mathbb{1}$ and $\mathring{\boldsymbol{r}}_i(0) = \boldsymbol{r}_{0,i}$ we have

$$\begin{aligned}\boldsymbol{r}_i(\gamma) &= \left(1 + \frac{\mathcal{D}}{\mathcal{D}\gamma}\mathbf{F}(\gamma)\Big|_{\gamma\to 0}\gamma\right)\boldsymbol{r}_{0,i} + \left(\frac{\mathcal{D}}{\mathcal{D}\gamma}\mathring{\boldsymbol{r}}_i(\gamma)\right)\Big|_{\gamma\to 0}\gamma + \mathcal{O}(\gamma^2). \\ &= \boldsymbol{r}_{\mathrm{A}} + \delta\boldsymbol{r}_{\mathrm{NA}}\,\gamma + \mathcal{O}(\gamma^2)\end{aligned} \tag{1.24}$$

where we identified the affine position after the application of the deformation gradient tensor $\boldsymbol{r}_{\mathrm{A},i} = \mathbf{F}(\gamma)\boldsymbol{r}_{0,i}$ and the non-affine correction given by $\delta\boldsymbol{r}_{\mathrm{NA},i}\ \gamma$ in the linear response regime which displaces the particles to their equilibrium positions.

In order to evaluate the linear non-affine elastic response of the solid we have to consider the derivative of the total potential energy with respect to the shear angle γ. The thermodynamic tension is defined as the first derivative with respect to γ as [57]

$$\begin{aligned}t =& \frac{1}{V}\frac{\mathcal{D}U}{\mathcal{D}\gamma}\Big|_{\gamma\to 0} \\ =& \frac{1}{V}\left(\frac{\partial U}{\partial\gamma} + \frac{\partial U}{\partial\mathring{\boldsymbol{r}}}\cdot\frac{\mathcal{D}\mathring{\boldsymbol{r}}}{\mathcal{D}\gamma}\right)\Big|_{\gamma\to 0} \\ =& \frac{1}{V}\frac{\partial U}{\partial\gamma}\Big|_{\gamma\to 0}\end{aligned} \tag{1.25}$$

where the last equality holds since we are the differentiating under the constraint of mechanical equilibrium $\frac{\partial U}{\partial\mathring{\boldsymbol{r}}} = 0$. The elastic moduli are defined as the second derivative

of the energy U with respect to the strain, where in particular the shear modulus is

$$G = \frac{1}{V}\frac{\mathcal{D}^2 U}{\mathcal{D}\gamma^2}\bigg|_{\gamma\to 0}. \tag{1.26}$$

Consequently, we evaluate the second derivative of U as [57]

$$\frac{\mathcal{D}^2 U}{\mathcal{D}\gamma^2}\bigg|_{\gamma\to 0} = \frac{\mathcal{D}}{\mathcal{D}\gamma}\frac{\partial U}{\partial \gamma}\bigg|_{\gamma\to 0} = \left(\frac{\partial^2 U}{\partial \gamma^2} + \frac{\partial^2 U}{\partial \mathring{\boldsymbol{r}}\partial\gamma}\cdot\frac{\mathcal{D}\mathring{\boldsymbol{r}}}{\mathcal{D}\gamma}\right)\bigg|_{\gamma\to 0}. \tag{1.27}$$

Using the definitions of the affine force field $\boldsymbol{\Xi}$ and the non-affnine displacement fields given in Eqs. (1.20) and (1.22), we conclude that the shear modulus can be written as [57]

$$G = \frac{1}{V}\left(\frac{\partial^2 U}{\partial\gamma^2}\bigg|_{\gamma\to 0} - \boldsymbol{\Xi}\cdot\mathbf{H}^{-1}\cdot\boldsymbol{\Xi}\right). \tag{1.28}$$

The first term in the above expression represents the variation of the thermodynamic stress with γ when the particles in the system are constrained not to relax into the non-affine equilibrium positions [62]. It therefore is the affine contribution to the shear elasticity, abbreviated with G_{A}, which corresponds to the result obtain by Born and Huang [11]. The second contribution gives the non-affine correction G_{NA} which arises due to the additional relaxation processes arising due to the lack of local particle symmetry in the system. Note that this contribution is always negative and therefore reduces the elastic constants.

We will now specialise these non-affine expressions to he case of the pair potentials, since the will appear frequently in the following chapters. To this end it is useful to introduce the Green-Saint Venant strain tensor $\boldsymbol{\eta}$ which is defined in terms of the deformation gradient tensor as [57]

$$\boldsymbol{\eta} = \frac{1}{2}\left(\mathbf{F}^T\mathbf{F} - \mathbb{1}\right). \tag{1.29}$$

which for the present case of pure shear, with the corresponding deformation gradient tensort $\mathbf{F}$ being defined in Eq. (1.15), takes the form

$$\boldsymbol{\eta} = \frac{1}{2}\begin{pmatrix} 0 & \sin(\gamma) & 0 \\ \sin(\gamma) & 0 & 0 \\ 0 & 0 & 0 \end{pmatrix}. \tag{1.30}$$

This representation of the strain tensor appears when describing change of the relative position between particles when the transformation $\boldsymbol{r} = \mathbf{F}\mathring{\boldsymbol{r}}$ is applied since

$$r^2 = \mathring{r}^2 + 2\,\mathring{\boldsymbol{r}}^T \cdot \boldsymbol{\eta} \cdot \mathring{\boldsymbol{r}} \tag{1.31}$$

where $r^2 = |\boldsymbol{r}|^2$ and $\mathring{r}^2 = |\mathring{\boldsymbol{r}}|^2$. Consequently, this definition of the strain tensor allows us to write the interaction potential $U(\boldsymbol{r}, \mathbf{F})$ in terms of the reference coordinate and $\boldsymbol{\eta}$ as $U(\mathring{\boldsymbol{r}}, \boldsymbol{\eta})$. This is useful since usually the elastic constants are computed in terms of derivates of the potential energy with respect to the strain tensor $\boldsymbol{\eta}$ instead of $\mathbf{F}$ [57]. If the interaction in the system are describe by a central-force pair potential $U(\boldsymbol{r}) = \frac{1}{2}\sum_{\langle i,j\rangle} V(r_{ij})$ we can explicitly write the affine force field in the case of pure shear as [57]

$$\boldsymbol{\Xi}_i = -\sum_j \left(c_{ij} r_{ij} - t_{ij}\right) n_{ij}^x n_{ij}^y \hat{\boldsymbol{n}}_{ij} \tag{1.32}$$

with the bond stiffness c_{ij} and bond tension t_{ij} as defined in Eq. (1.6). Furthermore, the unit bond vector is given by $\hat{\boldsymbol{n}}_{ij} = \boldsymbol{r}_{ij}/r_{ij}$, and n_{ij}^α with $\alpha = x,\, y$ are the respective cartesian components. Note that the summation in the above equation is restricted only to particles j which are interacting with particle i through the pair-potential $U(r_{ij})$. The affine shear modulus G_A can be expressed along the same lines as

$$G_\mathrm{A} = \frac{1}{V}\sum_{i,j} r_{ij}\left(c_{ij} r_{ij} - t_{ij}\right)\left(n_{ij}^x n_{ij}^y\right)^2 \hat{\boldsymbol{n}}_{ij} \tag{1.33}$$

which corresponds to the Born approximation of the elastic constants with central-force pair interaction [11].

1.4 Contribution to elasticity from different length scales

The result in Eq. (1.28) expresses to non-affine correction to the elastic moduli in terms of the Hessian matrix. This form suggests to employ a normal mode analysis to in order to achieve a characterisation of the non-affine displacements in terms of the eigenvalue spectrum of the system [57]. This will allow us to track the contributions to the non-affine elastic moduli coming from different frequency, or equivalently, length scales. Using the Dirac notation, we denote the eigenvectors of the Hessian as $|\boldsymbol{u}_{\boldsymbol{p}}\rangle = |\boldsymbol{p}\rangle$ which obey the eigenvalue problem $\mathbf{H}\,|\boldsymbol{p}\rangle = \lambda_p\,|\boldsymbol{p}\rangle$. Assuming that that all particles have the same mass,

i.e. $m_i = m \; \forall \, i$, the eigenvalues are given by $\lambda_p = m\omega_p^2$. We therefore expand the affine force field with respect to the eigenbasis as

$$\boldsymbol{\Xi} = \sum_p |\boldsymbol{p}\rangle\langle\boldsymbol{p}|\, \boldsymbol{\Xi}\rangle = \sum_p \widehat{\Xi}_p \, |\boldsymbol{p}\rangle \tag{1.34}$$

with the expansion coefficients given by $\hat{\boldsymbol{\Xi}}_p = \langle \boldsymbol{p}|\, \boldsymbol{\Xi}\rangle$. Employing the same expansion, the non-affine displacement fields can be written as

$$\begin{aligned} \delta \boldsymbol{r}_{\mathrm{NA}} = \left. \frac{\mathcal{D}\mathring{\boldsymbol{r}}}{\mathcal{D}\gamma} \right|_{\gamma \to 0} &= \mathbf{H}^{-1} |\boldsymbol{\Xi}\rangle \\ &= \sum_p |\boldsymbol{p}\rangle\langle\boldsymbol{p}|\, \mathbf{H}^{-1} |\boldsymbol{\Xi}\rangle \\ &= \sum_p \frac{\widehat{\Xi}_p}{\lambda_p} \, |\boldsymbol{p}\rangle \end{aligned} \tag{1.35}$$

where in the last step we made use of $\mathbf{H}^{-1} \, |\boldsymbol{p}\rangle = \lambda_p^{-1} \, |\boldsymbol{p}\rangle$. Note that the sum over p is subject to the condition that $\lambda_p \neq 0$. Subsequently, the non-affine contribution of the elasticity G_{NA} takes the form

$$G_{\mathrm{NA}} = \frac{1}{V} \langle \boldsymbol{\Xi}|\, \mathbf{H}^{-1} \, |\boldsymbol{\Xi}\rangle = \frac{1}{V} \sum_p \frac{\langle \boldsymbol{\Xi} \, |\boldsymbol{p}\rangle\langle\boldsymbol{p}|\, \boldsymbol{\Xi}\rangle}{\lambda_p} = \frac{1}{V} \sum_p \frac{\widehat{\Xi}_p \widehat{\Xi}_p}{\lambda_p}. \tag{1.36}$$

With this equation at hand we can obtain insights into the contributions to G_{NA} coming from the different eigenvalues $\lambda_p = m\omega_p^2$ corresponding to the vibrational eigenmodes of the Hessian $\mathbf{H}$. An essential observation to make at this point is that clearly the low-frequencies will provide the dominant contribution of the non-affine correction due to the fact that the eigenfrequencies enter in the denominator of the sum.

$$\rho(\omega) = \frac{1}{dN} \sum_{p=1}^{dN} \delta(\omega - \omega_p) \tag{1.37}$$

For the purpose of obtaining a continuum version of Eq. (1.36) in the thermodynamic limit where the particle number N and the system size V tend to infinity keeping the density N/V constant, it proves useful to rewrite G_{NA} in terms of contributions coming from small frequency neighbourhoods $\mathrm{d}\omega$ around the eigenfrequencies ω_p. For this reason

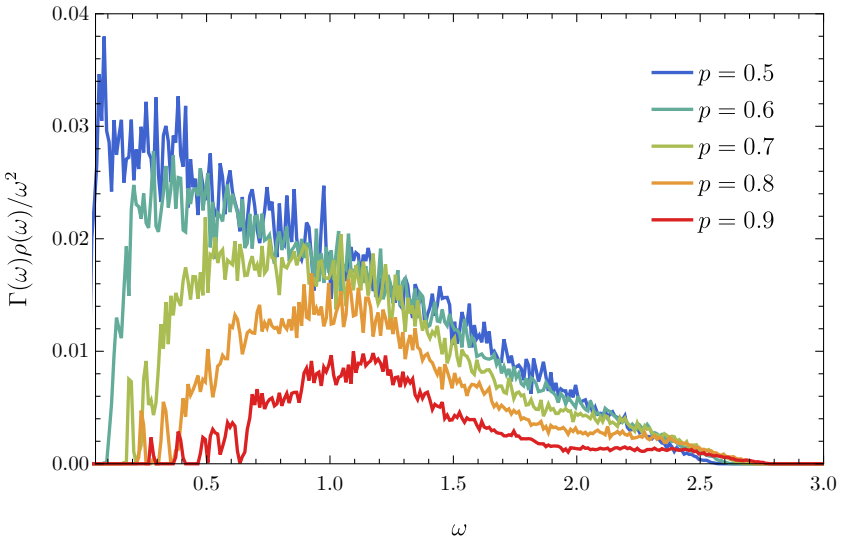

Fig. 1.4 The integrand of Eq. (1.39) for the bond-depleted fcc lattice, which represents the contribution to the non-affine correction to elasticity from different frequencies, or equivalently length scales.

we introduce the non-affine frequency correlator $\Gamma(\omega)$ defined as [57]

$$\Gamma(\omega) = \left\langle\!\!\left\langle \widehat{\Xi}_p \widehat{\Xi}_p \right\rangle\!\!\right\rangle_\omega \tag{1.38}$$

where the statistical average $\langle\!\langle \ldots \rangle\!\rangle_\omega$ is taken within the frequency shells $\omega_p \in [\omega, \omega + \mathrm{d}\omega]$. The affine force field $\boldsymbol{\Xi}$ itself directly depends on the randomness of the configuration of particles. Consequently, in the thermodynamic limit we transform the summation over p in Eq. 1.36 into an integral with respect to $\mathrm{d}\omega$ and write

$$G(\omega) = G_\mathrm{A} - \int_0^\infty \frac{\rho(\omega)\Gamma(\omega)}{m\omega^2}\,\mathrm{d}\omega. \tag{1.39}$$

In conclusion, the contribution originating from different frequency shells $d\omega$ to the non-affine correction is described in term of the function $\rho(\omega)\Gamma(\omega)/\omega^2$. We show the integrand of Eq. (1.39) for the three-dimensional bond-depleted crystal in Fig. 1.4. We can clearly observe the growing influence of the low-frequency modes when the disorder in the lattice is increased by removing bonds.

1.5 Linear viscoelastic response

So far we have considered the case of quasi-static deformations using Newtonian dynamics to describe the linear response of the system to the deformation induced by $\mathbf{F}$. By virtue

of the quasi-static assumption, the particle could follow the deformation imposed by the strain adiabatically, which means that the relaxation to the non-affine equilibrium was assumed to be much faster than the externally applied strain rate. We now want to consider the situation where the rate of the externally applied strain can vary and be comparable to the timescale of the non-affine relaxation. In contrast to the previous adiabatic case where the particle always remained at an energy minimum during the deformation, this now is no longer the case. Consequently, in this non-adiabatic case the externally applied force leads to an energy transfer, which means that we now have an energy dissipation mechanism which dissipates the energy which is injected through the external driving force [57]. We start the description of this physical situation from the damped and driven Newtonian equation of motion for the time-dependent displacement $\boldsymbol{x}_i(t) = \mathring{\boldsymbol{r}}_i(t) - \mathring{\boldsymbol{r}}_i$ of the i^{th} particle from its reference configuration which is given by [57]

$$m\frac{\mathrm{d}^2\boldsymbol{x}_i}{\mathrm{d}t^2} + \nu\frac{\mathrm{d}\boldsymbol{x}_i}{\mathrm{d}t} + \mathbf{H}_{ij}\boldsymbol{x}_j = \boldsymbol{\Xi}_i\eta \tag{1.40}$$

where the summation over the index j is implicit and where m and ν are the mass and the friction coefficient, here assumed to be equal for each particle. This equation of motion holds in the limit of infinitesimal strain, i.e. we assume $\|\mathbf{F} - \mathbb{1}\| \ll 1$. In order to solve the equation of motion we first decompose the displacements $\boldsymbol{x}_i$ into the eigenvectors of the Hessian $\mathbf{H}$, which means that $\boldsymbol{x}_i = \sum_p \widehat{x}_p \boldsymbol{u}_{p,i}$, where the expansion coefficients are $\widehat{x}_p = \boldsymbol{x}_i^T \cdot \boldsymbol{u}_{i,p}$.

Restricting the analysis to the case of an oscillatory shear strain of the form $\eta(t) = \tilde{\eta}\sin(\omega t)$, we apply a Fourier transformation, $\widetilde{\boldsymbol{x}}_i(\omega) = \sqrt{2\pi}^{-1}\int \boldsymbol{x}_i(t)\,\mathrm{e}^{i\omega t}\,\mathrm{d}t$, to write the damped equation of motion in frequency space as [57]

$$-m\omega^2\widehat{\widetilde{x}}_p + i\omega\widehat{\widetilde{x}}_p + m\omega_p^2\widehat{\widetilde{x}}_p = \widehat{\Xi}_p\tilde{\eta}. \tag{1.41}$$

After rearranging the terms, the solution in terms of the normal mode coefficients is

$$\widehat{\widetilde{x}}_p = -\frac{\widehat{\Xi}_p\,\tilde{\eta}}{m\omega^2 - m\omega_p^2 - i\omega\nu} \tag{1.42}$$

For the purpose of deriving an expression for the viscoelastic response, we consider the deviation the thermodynamic stress Δt_η in the configuration $(\mathring{\boldsymbol{r}}(t), \eta)$ from the reference configuration $(\mathring{\boldsymbol{r}}, 0)$. Therefore, we continue with

$$\Delta t_\eta = \frac{1}{V}\left(\frac{\partial U}{\partial\eta}(\mathring{\boldsymbol{r}}(t), \eta) - \frac{\partial U}{\partial\eta}(\mathring{\boldsymbol{r}}, 0).\right) \tag{1.43}$$

Since we treat the problem in the regime of small strain amplitudes, we expand the above terms in $\mathring{\boldsymbol{r}}$ and η which yields

$$\frac{\partial U}{\partial \eta}(\mathring{\boldsymbol{r}}(t),\eta) = \frac{\partial U}{\partial \eta} + \frac{\partial^2 U}{\partial \eta \partial \eta}\eta + \frac{\partial^2 U}{\partial \eta \partial \mathring{\boldsymbol{r}}}\mathring{\boldsymbol{r}}(t) + \mathcal{O}(\eta^2) \tag{1.44}$$

and

$$\frac{\partial U}{\partial \eta}(\mathring{\boldsymbol{r}},0) = \frac{\partial U}{\partial \eta} + \frac{\partial^2 U}{\partial \eta \partial \mathring{\boldsymbol{r}}}\mathring{\boldsymbol{r}} + \mathcal{O}(\eta^2). \tag{1.45}$$

Plugging these expressions back into Eq. (1.43) we obtain to first order in the strain η

$$\Delta t_\eta = \frac{1}{V}\left(\frac{\partial^2 U}{\partial \eta \partial \eta}\eta + \frac{\partial^2 U}{\partial \eta \partial \mathring{\boldsymbol{r}}}\boldsymbol{x}(t)\right) + \mathcal{O}(\eta^2). \tag{1.46}$$

Fourier transforming Δt_η to frequency space we obtain and making use of the result Eq. (1.43) we continue with

$$\begin{aligned}
\Delta\widetilde{t}_\eta(\omega) =& G_\mathrm{A}\widetilde{\eta} + \frac{1}{V}\sum_p \widehat{\Xi}_p \widehat{\widetilde{x}}_p(\omega) \\
=& G_\mathrm{A}\widetilde{\eta} + \frac{1}{V}\sum_p \frac{\widehat{\Xi}_p\,\widehat{\Xi}_p}{m\omega^2 - m\omega_p^2 - i\omega\nu}\widetilde{\eta} \\
=& G^*(\omega)\eta(\omega)
\end{aligned} \tag{1.47}$$

with the complex modulus given by

$$G^*(\omega) = G_\mathrm{A} + \frac{1}{V}\sum_p \frac{\widehat{\Xi}_p\,\widehat{\Xi}_p}{m\omega^2 - m\omega_p^2 - i\omega\nu}. \tag{1.48}$$

As for the static elastic response before, we can write the complex viscoelastic response of the system in the thermodynamic limit $N, V \to \infty$ as

$$G^*(\omega) = G_\mathrm{A} + \int_0^\infty \frac{\rho(\omega_p)\Gamma(\omega_p)}{m\omega^2 - m\omega_p^2 - i\omega\nu}\,\mathrm{d}\omega_p \tag{1.49}$$

where ω is the driving frequency of the applied oscillatory shear strain $\widetilde{\eta}$.

Chapter 2

Vibrational and mechanical properties of defective fcc lattices

A fundamental physical understanding of the mechanical properties of disordered materials at the level of their constituent building blocks has widespread applications, from metallurgy to relatively new fields such as photonic materials [13, 106]. To achieve this goal, it is important to identify suitable model systems where the atomic-scale or particle-scale physics can be described by means of theoretical frameworks to provide sufficiently general principles and insights. From this point of view, fcc crystals with point defects represent an ideal model system: they are amenable to theoretical approaches and at the same time are found in important technological applications. For example, photonic crystals made of colloidal particles are intensely studied for the opportunity they offer to control and manipulate light flow through a material, where the photonic band gap can be tuned by the particle size and lattice spacing [45, 74]. Stable colloidal crystal phases are most of the time fcc lattices with point defects, mostly vacancies, and are promising materials also for optical computing.

In fact, in a recent publication Zargar et al.studied disordered colloidal crystals in terms of their anomalous vibrational properties [104], observing excess vibrational modes in the form of a boson peak at low frequencies. Using confocal microscopy it is possible to track the colloidal particles and subsequently extract the vibrational density of states from the correlation matrix of the displacements of the individual particles. In this work, polycrystalline samples of colloidal packings of varying degrees of disorder were created, which made it possible to study the properties of the crystal in a well-defined dependence on the disorder concentration. Interestingly, the Voronoi tessellations obtained in this work for the crystalline samples of different degrees of disorder resemble regular lattices with vacancy defects. An example of such a structure is depicted below in

Fig. 2.7 for low and high defect concentration. As was recently discussed in Ref. [67], by relating the vibrational properties to the linear elastic response of crystals with randomly removed bonds simple relations between the elastic properties and the average number of neighbours in the lattice can be obtained. These results will be discussed in more detail below. Bearing in mind the structure of the different polycrystalline samples of the colloidal crystals in Ref. [104], it is therefore our goal to extend the prediction of elastic properties by means of the non-affine framework to crystals with vacancy defects.

In this chapter we apply the quasi-static athermal framework of non-affine lattice dynamics to connect the mechanical and vibrational properties with the microstructure and its symmetries resorting to the key concept of local inversion symmetry. Our focus will be on two types of disordered harmonic bead-spring networks:

1. fcc lattices with randomly removed springs – which we call bond-depleted, and
2. fcc lattices with randomly removed particles, i.e. with vacancies.

The first case of the fcc crystal with randomly removed bonds was discussed recently in Ref. [67]. In this work numerical computations were employed to compare the non-affine lattice dynamics of the bond-depleted fcc crystal and a random network glass, both in the harmonic approximation. The two model systems have a very different bond-orientational order due to the fact that one is a crystal with cut bonds and the other a structurally disordered glass. Nevertheless, both exhibit the same scaling of the boson peak frequency and shear modulus with the average coordination number of the underlying network. This similarity has been found to be reflected in a strong correlation with the degree of local inversion symmetry, which directly enters the non-affine shear modulus discussed in Chapter 1 through the square of the affine force field, i.e. $G_{\mathrm{NA}} \propto |\boldsymbol{\Xi}|^2$. This also suggests that in analogy to the non-affinity, in these systems the scaling of the boson peak frequency ω_{BP} with the average coordination number is dictated by the local inversion symmetry breaking (ISB) [67].

Here we demonstrate that both the harmonic fcc crystal with randomly cut bonds and randomly removed beads feature the same scaling of the shear modulus with respect to the inversion-symmetry breaking parameter, which shows that local inversion-symmetry breaking around defects is the universal root source of the non-affine softening of the shear modulus. This result allows us to derive analytical relations for the non-affine (zero-frequency) shear modulus as a function of vacancy concentration in excellent agreement with numerical simulations. Nevertheless, due to the different microstructural disorder, the spatial fluctuations of the local ISB parameter are different in the vacancy and bond-depleted case. The vacancy fcc exhibits comparatively a more heterogenous

microstructural disorder (due to the broader distribution of coordination number Z), which is reflected in a different scaling relation between boson peak frequency in the DOS and the average $\bar{Z}$. These differences are less important at low vacancy concentrations, where the vibrational density of states of the vacancy fcc can be well described theoretically by the coherent-potential approximation, presented here for the bond-depleted fcc lattice in three dimensions.

Disordered crystals with vacancies are directly relevant to applications, as discussed above, but at the same time less amenable to theoretical analysis. For this reason we would like to determine under which conditions and in what range of parameters the two systems can be described by similar theoretical approaches. In the present discussion of the problem we assume that particles on the lattice are interacting by means of a nearest-neighbour harmonic pair potential

$$U(\boldsymbol{r}) = \frac{1}{2}\sum_{\langle i,j\rangle} V(r_{ij}) = \frac{1}{2}\sum_{\langle i,j\rangle}\left[(\boldsymbol{r}_{ij} - \boldsymbol{r}_{0,ij})\cdot\hat{\boldsymbol{n}}_{ij}\right]^2 \tag{2.1}$$

where $\langle i,j\rangle$ denotes the restriction of the sum to nearest-neighbour pairs and $r_{0,ij} = |\boldsymbol{r}_{0,ij}|$ is the rest length of the harmonic bond. Furthermore, since the non-affine formalism is based on the assumption of zero temperature, we neglect thermal fluctuations and focus on the limit of athermal solids which allows us to more clearly disentangle the relationship between local lattice symmetry and emerging elastic and vibrational properties. Furthermore, the low-temperature limit, where the control parameter is the particle packing fraction (or its lattice analogue: the coordination number), instead of temperature, is directly relevant to the case of colloidal crystals.

In the following, we start by recalling the core concepts of the non-affine lattice dynamics framework. We then apply it to compare the two types of disordered fcc lattices with regard to their shear elasticity as a function of defect concentration. Then we consider the vibrational density of states for the two systems, both by numerically diagonalising the underlying Hessian of the configurations and by means of an effective medium approach based on the coherent potential approximation.

2.1 Non-affine lattice dynamics of defective fcc crystals

The starting point of non-affine lattice dynamics is the realisation that in a disordered solid the standard affine approximation of the Born-Huang lattice dynamics [11] breaks

down. In other words, applying a shear strain γ to a disordered solid leads, in addition to the affine displacement of the particles, which is directly proportional to the applied strain, to a non-affine contribution to the displacement fields.

In a perfectly centrosymmetric lattice, the particle en route towards this affine position receives forces from its nearest-neighbors which cancel each other out by symmetry, leaving the particle at equilibrium in the affine position. In a disordered lattice, however, due to the local breaking of inversion symmetry on the given particle, these forces do not cancel, and their vector sum yields a net force that brings the particle to a final (non-affine) position which differs from $\boldsymbol{r}_{A,i}$.

These forces, which bring the particle away from the affine position into the final non-affine position, can be written out within the harmonic approximation of the interaction potential V, as $\boldsymbol{\Xi}_i = \frac{\partial \boldsymbol{f}_i}{\partial \gamma}|_{\gamma\to 0}$. In the absence of internal stresses, which means all bonds are relaxed in the harmonic energy minimum, hence $t_{ij} = 0$, the affine force field defined in Eq. (1.32) can be expressed as

$$\boldsymbol{\Xi}_i = -\kappa r_0 \sum_j n_{ij}^x n_{ij}^y \hat{\boldsymbol{n}}_{ij}, \tag{2.2}$$

since the stiffness $c_{ij} = 1$ in the harmonic approximation. The affine part of the above shear modulus is the standard Born-Huang formula, i.e.

$$G_{\mathrm{A}} = \frac{1}{V}\frac{\partial^2 U}{\partial \gamma^2}\bigg|_{\gamma\to 0} = \frac{\kappa r_0^2}{2V}\sum_{ij}\left(n_{ij}^x n_{ij}^y\right)^2. \tag{2.3}$$

Since the non-affine contribution to the shear modulus is proportional to the vector $\boldsymbol{\Xi}_i$, it vanishes for a perfect centrosymmetric crystal: the sum of triplets $\sum_j \hat{\boldsymbol{n}}_{ij} n_{ij}^x n_{ij}^y$ is identically zero if the nearest-neighbours are arranged symmetrically around the atom i, as one can easily verify. In other words, this is reflects the fact that the affine force field $\boldsymbol{\Xi}_i$ is non-zero if and only if the local inversion symmetry is broken.

2.1.1 Static shear modulus of the ideal and bond-depleted fcc crystals

It will be instructive to use the above formalism and derive the shear modulus for a perfect three-dimensional fcc crystal. Realizing that under the application of a pure x-y shear strain γ only the four bonds lying in the x-y-plane contribute to the shear modulus G_{A}, we simply have to use Eq. (2.3) and evaluate the sum appearing there. The four

unit bond vectors in the x-y-plane which contribute to this sum are given by

$$\hat{\boldsymbol{n}}_1 = \frac{1}{\sqrt{2}}\begin{pmatrix}1\\1\\0\end{pmatrix}, \quad \hat{\boldsymbol{n}}_2 = \frac{1}{\sqrt{2}}\begin{pmatrix}-1\\1\\0\end{pmatrix}, \quad \hat{\boldsymbol{n}}_3 = \frac{1}{\sqrt{2}}\begin{pmatrix}1\\-1\\0\end{pmatrix}, \quad \hat{\boldsymbol{n}}_4 = \frac{1}{\sqrt{2}}\begin{pmatrix}-1\\-1\\0\end{pmatrix}. \tag{2.4}$$

Consequently, by virtue of Eq. (2.3) the shear modulus of the perfect fcc crystal is given by

$$G_{\mathrm{fcc}} = \frac{1}{2}\rho r_0^2 \kappa = \frac{\kappa}{a} \tag{2.5}$$

using $\rho r_0^2 = 2/a$, where a is the lattice constant of the fcc crystal, $\rho = N/V$ and r_0 the equilibrium bond length. We can extend this result to the case of a depleted fcc crystal, where bonds are randomly cut by evaluating the number of bonds that contribute on average to the x-y-plane as

$$G_{\mathrm{A}}^{\mathrm{depl}}(\bar{Z}) = \sum_{i=0}^{4} i \frac{\kappa}{4a} \frac{\binom{4}{i}\binom{8}{\bar{Z}-i}}{\binom{12}{\bar{Z}}} = \frac{\kappa}{a}\frac{\bar{Z}}{12}, \tag{2.6}$$

where $\bar{Z} \equiv \langle Z \rangle = \frac{1}{N}\sum_{i=1}^{N} Z_i P(Z_i)$ is the disorder-averaged connectivity. $P(Z_i)$ denotes the distribution of the local coordination numbers Z_i. In the above equation, the expression $\binom{4}{i}\binom{8}{\bar{Z}-i}/\binom{12}{\bar{Z}}$ represents the probability of having i bonds in the x-y-plane which depends on the total number of nearest-neighbour bonds $\bar{Z}$.

The shear modulus of a depleted fcc crystal vanishes at $\bar{Z} = 6$, the isostatic point of marginal stability, which can easily can be verified by Maxwell counting [23]. Using this fact, we have that $G(\bar{Z} = 6) = G_{\mathrm{A}}(\bar{Z} = 6) - G_{\mathrm{NA}}(\bar{Z} = 6) = 0$. The non-affine contribution exactly cancels the affine modulus at $\bar{Z} = 6$, which is a common feature of random central-force lattices [101]. In addition to that, G_{NA} should vanish for $\bar{Z} = 12$, i.e. for the case of an ideal fcc crystal the non-affine softening is absent. Assuming the linear behaviour of the non-affine contribution [67], which is justified a posteriori through numerics, G_{NA} can be written as the linear interpolation between the above two cases at $\bar{Z} = 6$ and $\bar{Z} = 12$, i.e.

$$G_{\mathrm{NA}}^{\mathrm{depl}}(\bar{Z}) = \frac{\kappa}{a}\frac{12 - \bar{Z}}{12}. \tag{2.7}$$

Subtracting the non-affine contribution from the affine shear modulus we arrive at a simple expression for the shear modulus of the bond-depleted fcc crystal

$$G^{\mathrm{depl}}(\bar{Z}) = G_{\mathrm{A}}^{\mathrm{depl}}(\bar{Z}) - G_{\mathrm{NA}}^{\mathrm{depl}}(\bar{Z}) \tag{2.8}$$

$$= \frac{\kappa}{a}\frac{\bar{Z}-6}{6}. \tag{2.9}$$

These results for the shear modulus have been obtained in Ref. [67] and are plotted in Fig. 2.1.

2.2 From the bond-depleted to the vacancy fcc

When considering bond-depleted systems it is natural to use the bond-occupation probability p as a control parameter. Therefore we set $p = \bar{Z}/Z_0$, where $Z_0 = 12$ is the number of nearest-neighbour bonds in the perfect fcc crystal. We now want to establish a connection between the physical properties of the bond-depleted case and a fcc crystal with vacancies where a certain fraction of particles is removed via the same random mechanism, thereby introducing defects. By randomly removing N' particles from the N lattice sites, we are left with $N - N'$ particles. In this sense, we want to describe the elastic and vibrational properties of a fcc crystal with vacancies as a function of the vacancy concentration $c = N'/N$ with a new particle density $\rho' = (N - N')/V$.

As we will see, it is possible to obtain the average connectivity $\bar{Z}$ present in a defected 3D fcc crystal of a given vacancy concentration c by means of a combinatorial argument. This is done by computing the average connectivity of one lattice site in the vacancy fcc via

$$\bar{Z} = \sum_{i=0}^{12} i \frac{\binom{12}{i}\binom{N-12}{N-N'-i}}{\binom{N}{N-N'}} = 12\left(1 - \frac{N'}{N}\right) = 12(1-c). \tag{2.10}$$

In terms of the bond occupancy probability $p = \bar{Z}/12$ this results in the simple relation $p = 1 - c$. Using an analogous combinatorial argument we can explicitly write down the fluctuation of the Z-distribution for the vacancy fcc as

$$\sigma_Z^2 = \langle Z^2\rangle - \langle Z\rangle^2 = 12\frac{\left(1-\frac{12}{N}\right)\left(1-\frac{N'}{N}\right)\frac{N'}{N}}{1-\frac{1}{N}}$$

$$\xrightarrow{N\to\infty} 12c(1-c) \tag{2.11}$$

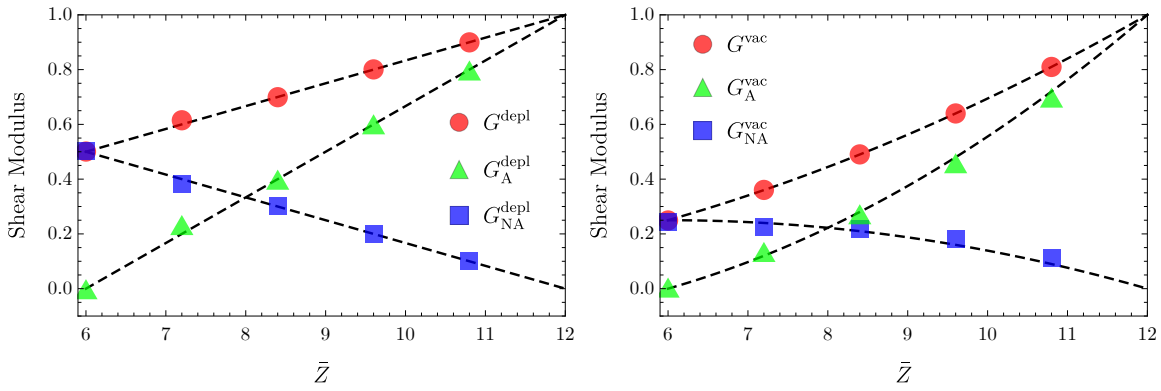

Fig. 2.1 Comparing the shear modulus of the 3D fcc crystal in the case of vacancy defects and bond depletion. The dashed lines are the shear moduli according to Eq. 2.8 in the left panel and Eq. 2.14 in the right panel. The left panel represents the findings from Ref. [67].

where in the last step $N'/N = c$ is kept constant. Consequently, this leads us to ask whether this simple analogy between the depleted and defective fcc carries over to the elasticity and the vibrational properties.

Substituting the relation $p = 1 - c = \bar{Z}/12$ and the resulting new number density $\rho' = \frac{N-N'}{V} = \frac{N}{V}(1-c) = \rho(1-c)$ into to the expression for the bond-depleted fcc shear modulus $G_{\mathrm{A}}^{\mathrm{depl}}$, we obtain the affine part of the shear modulus with vacancies

$$G_{\mathrm{A}}^{\mathrm{vac}} = \frac{\kappa}{2}\rho' r_0^2 \frac{\bar{Z}}{12} = \frac{\kappa}{a}(1-c)^2. \tag{2.12}$$

In the same way, we can transform the non-affine contribution of the bond-depleted fcc shear modulus $G_{\mathrm{NA}}^{\mathrm{depl}}$ and obtain

$$G_{\mathrm{NA}}^{\mathrm{vac}} = \frac{\kappa}{a}c(1-c), \tag{2.13}$$

such that the full vacancy shear modulus becomes

$$G^{\mathrm{vac}} = G_{\mathrm{A}}^{\mathrm{vac}} - G_{\mathrm{NA}}^{\mathrm{vac}} = \frac{\kappa}{a}(1-c)(1-2c). \tag{2.14}$$

In terms of the average coordination number $\bar{Z}$ this result reads

$$G^{\mathrm{vac}} = \frac{\kappa}{a}\frac{\bar{Z}}{12}\frac{\bar{Z}-6}{6} = \frac{\bar{Z}}{12}G^{\mathrm{depl}}. \tag{2.15}$$

In order to check the validity of formula (2.14) derived for the vacancy fcc shear modulus above, we now compare this prediction to the result of a numerical solution of the

non-affine lattice dynamics equations of the vacancy fcc crystal. The numerical solution of lattice dynamical equation for the shear modulus is based on initiating a perfect fcc crystal of a given density $\rho = N/V$ consisting of 4000 particles and interacting via a harmonic potential subject to periodic boundary conditions. Then bonds or particles are removed at random from the system to reach the desired bond-occupation p or, alternatively, vacancy concentration c, respectively. This is done by generating a perfect fcc lattice and consecutively connecting all nearest neighbours with springs. In the case of the depleted fcc lattice, bonds are then deleted uniformly at random from the list of all nearest neighbour bonds thereby invoking a disorder in the local coordination number [67]. In the case of the vacancy fcc particles are selected uniformly at random and are then removed together with all connected nearest neighbour springs. The resulting configuration is then used to solve the equations of motion of non-affine lattice dynamics [57] from which the shear modulus can be extracted.

In contrast to the case of a bond-depleted fcc crystal, where we can generate configurations with different distributions peaked around the average connectivity $\bar{Z}$, we have no such control over the Z-distribution in the defective crystal with vacancies. In particular, we generated a bond-depleted fcc crystal with a very narrow Z-distribution. In this narrow case the variance of the distribution of the average connectivity $P(Z)$ is 0.07, 0.23, 0.24, 0.24, 0.16 for $\bar{Z}$ =6, 7.2, 8.4, 9.6, 10.8, respectively.

The vacancy fcc crystal has a much broader Z-distribution. Its variance, which is analytically given by Eq. (2.11), is 2.95, 2.98, 2.54, 1.91, 1.07 for $\bar{Z}$ =6, 7.2, 8.4, 9.6, 10.8, see also Fig. 2.3. The trend of the distribution $P(Z)$ for the vacancy fcc towards smaller variances at smaller vacancy concentrations is due to the saturation of the distribution at $Z = 12$, i.e. particles cannot have more than 12 nearest neighbours. This also means that $P(Z)$ is not symmetric around $\bar{Z}$ for low vacancy concentrations. The numerical solution for the affine and non-affine shear modulus of the vacancy fcc shows very good agreement with numerical simulations over a broad range of the average coordination number $\bar{Z}$, as depicted in Fig. 2.1, where we plotted the affine and non-affine contributions separately.

2.3 Vibrational properties in the presence of vacancies

In this section we turn to the vibrational properties of the vacancy fcc crystal in order to compare it to the well-studied case of the bond-depleted fcc. We will see that the low-frequency properties of the vibrational density of states (vDOS) are closely related cases when the vacancy concentration is low. Both the vDOS of the vacancy and the

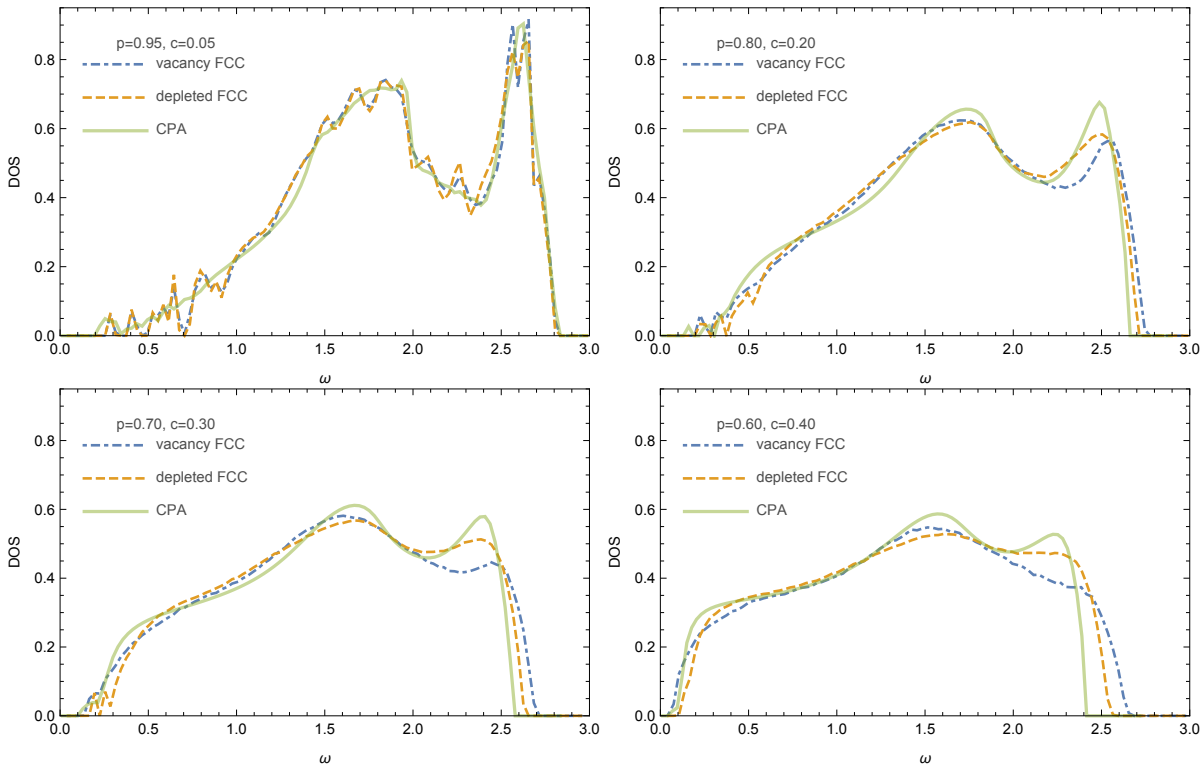

Fig. 2.2 Comparison of the DOS of the depleted fcc with narrow Z-distribution and the vacancy fcc to the DOS obtained from the solution of the EMT equations in the coherent potential approximation.

bond-depleted fcc were obtained from a direct numerical diagonalisation of the underlying Hessian matrix $\mathbf{H}$.

In addition to that we computed the DOS of the bond-depleted fcc in the coherent potential approximation (CPA) [32, 40, 22], which serves as a self-consistent effective-medium theory (EMT) description for the fcc with randomly cut bonds, characterised by the bond-occupation probability $p = \bar{Z}/12$.

The CPA is based on the idea to describe the inhomogeneous, disordered lattice with an effective lattice which is homogenous but with springs that may have complex-valued and frequency-dependent springs constants, which account for scattering and damping of vibrational excitations on the impurites of the lattice. The defining property of the CPA is, in order to self-consistently compute the properties of the effective medium, to require that the scattering matrix locally averages to zero [12]. More details on this and a formal derivation can be found in the Appendix A. There is very good agreement between the vacancy fcc, depleted fcc and the EMT solution across the whole frequency range for a low vacancy concentration. This is illustrated in Fig. 2.2 for the high bond-occupation probability $p = 0.95$, or alternatively the low vacancy concentration $c = 0.05$. Increasing

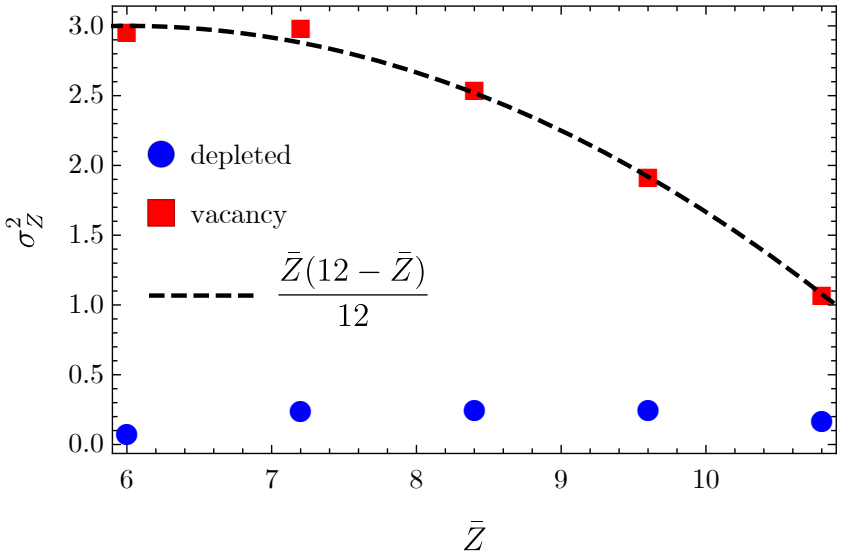

Fig. 2.3 The fluctuations of the Z-distribution for depleted and vacancy fcc vs $\bar{Z}$. This is in accordance with the prediction Eq. (2.11) shown as the dashed line.

c, or decreasing p, the agreement becomes less reliable. In fact, the DOS obtained by means of the coherent potential approximation does not precisely capture the form of the DOS of the bond-depleted fcc, despite the fact that the bond-depletion was carried out such that the Z-distribution is very narrow to resemble the effective-medium solution, which does not account for fluctuations in the connectivity. Partly this happens due to the fact that CPA does not properly account for scattering from pairs of defects, which means that effects due to correlations between scattering centres are not taken into account. The effective-medium description only is accurate when the separation between defects is large enough such that the amplitude of a scattered wave is negligible at the neighbouring defect [18], an assumption which gradually fails with increasing the overall number of defects in the lattice. In order to understand the precise physical nature of the deviations in different regions of the spectrum additional analysis would be required. However, since the non-affine correction to the elastic moduli is determined by the low-frequency part of the spectrum, where agreement between direct diagonalisation and CPA is good, this is left for future work.

2.3.1 Scaling of the boson peak frequency

A universal feature of the vibrational density of states $D(\omega)$ of disordered solids and glasses is the excess of low-frequency modes with respect to the Debye scaling $D(\omega) \sim \omega^2$, which manifests itself as a peak in the vibrational density of states, widely referred to as

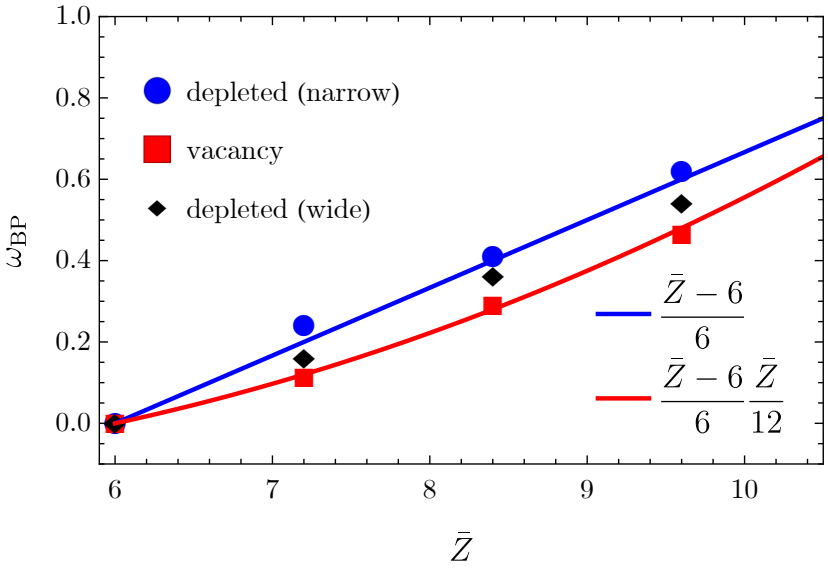

Fig. 2.4 Scaling of the boson peak frequency ω_{BP} with $\bar{Z}$ for the three model fcc crystals with different disorder.The value of ω_{BP} for the largest coordination number $\bar{Z} = 10.8$ is not included in the plot since the boson peak is not identifiable in the DOS.

the boson peak [8]. Since the appearance of the boson peak is a feature inherently rooted in the disorder in a physical system, the position of the boson peak in the vibrational spectrum (the boson peak frequency ω_{BP}) in disordered fcc crystals depends on the average coordination number $\bar{Z}$, which sets the magnitude of disorder. In particular, in the case of the bond-depleted fcc (and the random spring network) it is known to have the scaling $\omega_{BP} = \frac{(\bar{Z}-6)}{6}$ [67].

This numerically computed scaling of ω_{BP} for the bond-depleted fcc is plotted in Fig. 2.4. Interestingly, the same scaling does not hold true for the fcc crystal with vacancies. In fact, the boson peak frequency ω_{BP} of the vacancy fcc features a parabolic scaling with the average connectivity $\bar{Z}$, which is fitted well by $\omega_{BP} = \frac{\bar{Z}-6}{6}\frac{\bar{Z}}{12}$. It appears that for both the bond-depleted and vacancy fcc, the boson peak frequency exhibits the same scaling with $\bar{Z}$ as the respective shear modulus G with $\bar{Z}$, see Tab. 2.1. This, however, is not generally the case. To see this we generated a depleted fcc with a Z-distribution which is not δ-like, but reflects the distribution $P(Z)$ in the vacancy fcc, i.e. a higher degree of connectivity fluctuations is introduced. Specifically, as in the vacancy case the distribution of the local coordination number is prescribed to be Binomial, i.e.

$$P(Z_i) = \binom{12}{Z_i} p^{Z_i} (1-p)^{12-Z_i} \tag{2.16}$$

which leads to an average coordination number

$$\bar{Z} = \sum_{i=1}^{12} i \binom{12}{i} p^i (1-p)^{12-i} = 12p. \tag{2.17}$$

The shear modulus scaling in this wide-depleted case is still the same as in the δ-like depleted case, i.e. $G^{\text{wide,depl}} \sim \frac{\bar{Z}-6}{6}$. However, the scaling of the boson peak frequency ω_{BP} now is different, as can be seen in Fig. 2.4. This rules out the possibility that G and ω_{BP} generally scale in the same way in our defective fcc systems.

Taking all this into account, the transition between the scalings of $\omega_{\text{BP}}^{\text{depl}}$ and $\omega_{\text{BP}}^{\text{vac}}$ is not given by the density transformation $\rho' = \frac{\bar{Z}}{12}\rho$. In fact, we assert that the boson peak is not primarily controlled by the average coordination number $\bar{Z}$, as is the case for the shear modulus. Fluctuations of the coordination number distribution will be of importance here, i.e. the degree of heterogeneity of the underlying microstructure will influence the scaling of the boson peak with $\bar{Z}$. Directly comparing the two different depleted fcc models, we see that increasing the connectivity fluctuations pushes the boson peak frequency to lower values. We will shed further light on this in the next section.

2.4 Parametrising the asymmetry of local particle configurations

We observed that for both the bond-depleted and vacancy fcc crystal the scalings of the shear modulus with the average connectivity $\bar{Z}$ coincide, whereas the same cannot be concluded for the scaling of ω_{BP} for the two types of systems. This effect must in some way be connected to the microstructural differences which arise through the different implementations of disorder in the bond-depletion and vacancy situation. With the aim of bringing a physical justification to the two different scalings of the shear modulus and the boson peak frequency we need to quantitatively describe the degree of local microstructural disorder.

The starting point is defining a parameter which serves as a measure for the degree of local inversion symmetry, by which we mean the condition that each nearest neighbor of a reference particle has a mirror particle diametrically opposed. The squared amplitude of the affine force vector $|\boldsymbol{\Xi}_i|^2$ precisely serves this purpose, measuring the local deviations from the case of perfect inversion symmetry. It is identically zero in a centrosymmetric crystal, where in the affine configuration, the local structure of nearest neighbors around a particle is such that the positions of two opposing neighbors are symmetric with respect

to a reflection at the central particle. In this case the square of the affine force vector $|\boldsymbol{\Xi}|^2$ is exactly zero, as mentioned above. For the other limiting case where the system completely lacks local inversion symmetry, we chose a reference configuration to normalise the ISB parameter with the corresponding squared affine force field. For this reference configuration we require that there be no correlations between the orientations of the bonds [67]. In this way we obtain a measure for the local inversion symmetry which varies between zero and one.

The ISB parameter derived from $|\boldsymbol{\Xi}|^2$ should be independent of the direction of the applied shear stress, which means it has to be summed over all possible coordinate pairs as

$$|\boldsymbol{\Xi}|^2 := \sum_{\alpha,\beta\in[x,y,z]} |\boldsymbol{\Xi}_{\alpha\beta}|^2. \tag{2.18}$$

Following the exposition in Ref. [67], we define the parameter for measuring the local inversion symmetry breaking as

$$\begin{aligned} F_{\mathrm{IS}} =& 1 - \frac{\sum_{\alpha,\beta} |\boldsymbol{\Xi}_{\alpha\beta}|^2}{\sum_{\alpha,\beta} |\boldsymbol{\Xi}_{\alpha\beta}|^2_{\mathrm{ISB}}} \\ =& -\frac{1}{N\bar{Z}} \sum_{i=1}^{N} \sum_{j,k\ n.n.\ i} \cos^3 \alpha_{jk} \end{aligned} \tag{2.19}$$

where $\bar{Z}$ is the coordination number, α and $\beta \in [x, y, z]$, and α_{jk} denotes the angle between the i-j and i-k bonds with the corresponding summation going over nearest neighbours only. The quantity $|\boldsymbol{\Xi}_{\alpha\beta}|^2_{\mathrm{ISB}}$ represents the limiting case of a system with maximally asymmetric and uncorrelated bond orientations which was shown to be equal to $\kappa R_0^2 \sum_{ij} (n_{ij,\alpha} n_{ij,\beta})^2$ [67]. A more detailed derivation of the above expression can be found in Appendix B. We now proceed to evaluate the degree of local inversion symmetry breaking in the two fcc crystals with bond-depletion and vacancy induced disorder.

2.4.1 Inversion symmetry breaking in the depleted fcc

As it was demonstrated in earlier work [67], it is possible to derive a analytical expression for the ISB parameter in the case of the bond-depleted fcc, with the result

$$F_{\mathrm{IS}}^{\mathrm{depl}} = 1 - \frac{\sum_{\alpha,\beta} |\boldsymbol{\Xi}_{\alpha\beta}|}{R_0^2 \kappa^2 N \bar{Z}} = 1 - \frac{12 - \bar{Z}}{11} = \frac{\bar{Z} - 1}{11}. \tag{2.20}$$

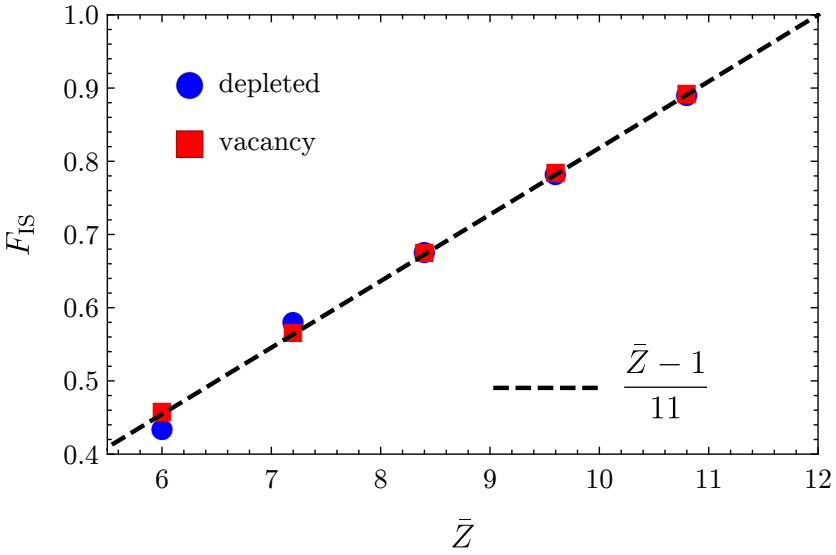

Fig. 2.5 Comparison between the average ISB parameter for the vacancy and depleted fcc

This perfectly aligns with the numerical evaluation of $F_{\mathrm{IS}}^{\mathrm{depl}}$, as can be seen from Fig. 2.5. From there we can also observe that the numerical computation of the inversion symmetry breaking parameter $F_{\mathrm{IS}}^{\mathrm{vac}}$ for the vacancy fcc yields virtually the same linear behaviour as in the depleted case. From a physical point of view, we can say that the average ISB parameter does not distinguish between vacancy and depleted fcc. This is because the ISB is defined in terms of the angles between nearest-neighbour particles in a unit cell. Hence, the average ISB being equal in the vacancy and depleted case means that the distribution of angles between next neighbours is the same on average. This is reasonable because particles or bonds are removed uniformly at random in both cases.

Naturally, this leads us to conjecture that the functional form in both cases is the same, i.e. $F_{\mathrm{IS}}^{\mathrm{depl}} = F_{\mathrm{IS}}^{\mathrm{vac}} = \frac{1}{11}(\bar{Z}-1)$. We have, however, not yet been able to verify this result analytically for the vacancy case. The physical picture behind this observation is as follows. The two different approaches of inducing disorder into the fcc crystal, i.e. by removing bonds or particles, produce a disordered microstructure in the crystal which on average exhibits the same degree of local inversion symmetry breaking. In fact, we can use this argument to justify why the shear moduli of the depleted and vacancy case differ only by the density correction due to the missing particles in the defected case.

When computing the elastic constants, only the average degree of disorder of the microstructure or, put differently, only the averaged degree of inversion symmetry breaking controls the shear modulus. Just as the ISB parameter, the non-affine contribution to

the shear modulus is proportional to the averaged squared amplitude of the affine force field $\boldsymbol{\Xi}$, i.e. $G_{\mathrm{NA}} \propto \langle |\boldsymbol{\Xi}_i|^2 \rangle$ [57, 67].

More specifically, for the computation of the zero-frequency shear modulus in the thermodynamic limit one needs to solve the integral [57]

$$G(\omega = 0) = G_{\mathrm{A}} - \frac{3N}{V} \int_0^\infty \mathrm{d}\omega' \frac{\rho(\omega')\Gamma(\omega')}{m\omega'^2} \tag{2.21}$$

where $\rho(\omega')$ is the density of states and $\Gamma(\omega')$ the correlator of the affine force fields between frequency shells. This correlator is defined as

$$\Gamma(\omega) = \langle\!\langle \boldsymbol{\Xi} \cdot \boldsymbol{u}_{\boldsymbol{p}}^2 \rangle\!\rangle_\omega \tag{2.22}$$

where $\boldsymbol{u}_p$ is the eigenvector of the Hessian $\mathbf{H}$, which belongs to the eigenfrequency ω_p. Since the density of states appears together with the non-affine correlator under the integral, similar features in the density of states are not sufficient to guarantee the same behaviour in terms of the elastic moduli. In this sense, the shear modulus is a coarse-grained, macroscopic physical quantity.

The physical mechanism responsible for the loss of mechanical stability, which fundamentally is based on the concept of local inversion symmetry is the same for both the depleted and vacancy fcc. We have seen above that the density enters as a prefactor into the formula of the shear modulus. By the above argument, the quantities inside the parentheses of Eq. (1.28), the full expression of the non-affine shear modulus as derived in Chapter 1, are the same for the bond-depleted and vacancy case, which leaves the corrected density as the only source of the different scaling of the shear modulus of the vacancy fcc.

2.4.2 Correlation of the boson peak with ISB fluctuations

As we have seen, the positions of the boson peak of the depleted and vacancy fcc generally show different correlations with the average connectivity $\bar{Z}$. But unlike in the case of the shear modulus scaling, the boson peak position cannot only depend on the density correction due to vacancies. This also indicates that the behaviour of ω_{BP} is not exclusively dictated by the average degree of inversion symmetry breaking. The shear modulus in contrast, being a macroscopic averaged quantity, is not sensitive to the fluctuations of the distributions $P(Z)$ and $P(F_{\mathrm{IS}})$ for the disordered fcc crystals.

To better understand the origin of the boson peak scaling we need to take these fluctuations into account. We numerically computed the distributions of the connectivity

and ISB parameter. The resulting widths of these distributions are plotted in Fig. 2.3 and Fig. 2.6. Naturally, the fluctuations of Z, i.e. the structural heterogeneity of the disordered fcc crystal, is directly linked to the fluctuations of F_{IS}. The δ-like distribution of the coordination number in the depleted fcc is linked to a microstructure which is less heterogenous when compared to the vacancy fcc.

Reducing the average connectivity towards the mechanical instability at Z_c, the fluctuations of the ISB monotonically increase. But for any given value of $\bar{Z}$, the fluctuations of the ISB are larger in the vacancy fcc. This behaviour is reflected in the fact that $P(F_{\mathrm{IS}})$ is a broader distribution in the vacancy case. This relative broadness goes hand in hand with a more asymmetric distribution: the vacancy $P(F_{\mathrm{IS}})$ has an excess at low values of the ISB parameter with respect to the depleted crystal case. Physically speaking, this means the vacancy fcc has an excess of sites with low inversion symmetry compared to the δ-like depleted fcc. So the higher fluctuations of F_{IS} in the vacancy fcc go along with a higher degree of asymmetry of $P(F_{\mathrm{IS}})$. As a consequence, the vacancy fcc develops highly undercoordinated sites much earlier than the bond-depleted fcc, when decreasing $\bar{Z}$. We can conclude that for the defective fcc crystals studied here that in the above sense structural heterogeneity modifies the boson peak via increased ISB fluctuations, such that ω_{BP} is pushed to lower frequencies. We have collected the scalings of the shear modulus and the ISB with $\bar{Z}$ in Tab. 1 for both the depleted and vacancy fcc.

In recent work [39, 38] a similar connection has been observed in a system where non-affine displacements are induced via thermal fluctuations instead of structural disorder, which complements our findings. The analytical and numerical results [37] show that if the non-affine displacements are enhanced via an external field there is an accumulation of low-frequency modes in the density of states, also linking non-affine fluctuations to the boson peak.

2.5 Application to colloidal crystals

Using the experimental input from Zargar et al. [104] we can obtain a numerical estimation for the absolute value of the shear modulus of a defective colloidal fcc crystals with vacancies. Two examples of configurations with a low ($c = 0.0167$) and high ($c = 0.169$) vacancy concentration are shown in Fig. 2.7. In these systems the defect concentration of a sample is determined using confocal microscopy.

To fix a numerical value of the shear modulus $G^{\mathrm{rvac}}(c)$ we also need the values of the lattice constant a of the colloidal crystal and its spring constant. In the experimental setup

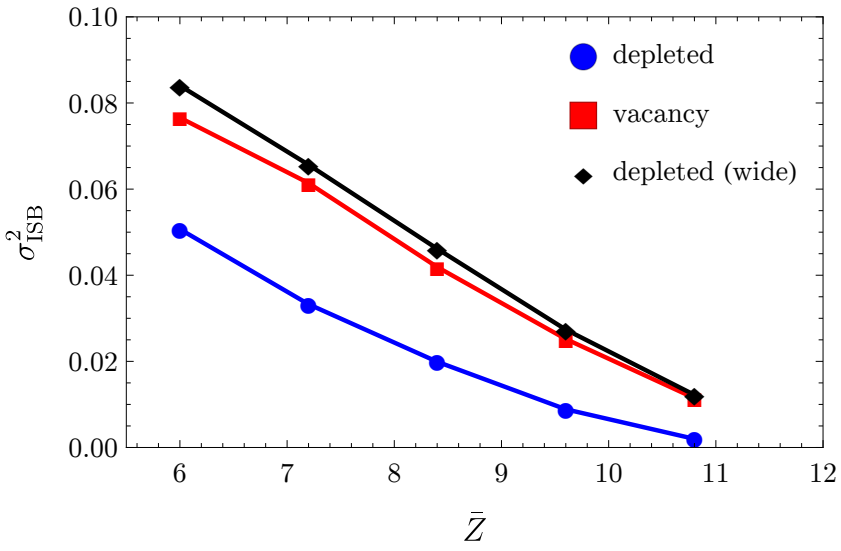

Fig. 2.6 Plot of the $\bar{Z}$-dependence of the variance of the distribution $P(F_{\mathrm{IS}})$.

of Zargar et al., a is given by 3.019 μm. The spring constant has to be estimated from the confocal microscopy data by determining the potential of mean force from the measured radial distribution function of the colloidal system in the liquid phase. The resulting main minimum of the potential of mean force is subsequently fitted with a harmonic potential, which in the present case fixes the spring constant to $\kappa = 9.24 \cdot 10^{-7} N/m$. Together with Eq. (2.14), we thus can estimate the vacancy shear modulus to be $G^{\mathrm{vac}}(c = 0) = 0.306$ Pa, $G^{\mathrm{vac}}(c = 0.0167) = 0.291$ Pa and $G^{\mathrm{vac}}(c = 0.169) = 0.168$ Pa. Thus, Eq. (2.14) predicts that the shear modulus of the crystal with vacancies should decrease by 50% when about 17% of the available lattice site are vacant. These estimates are qualitatively in agreement with the range of values measured experimentally for the shear modulus of colloidal suspensions at different volume fractions by Zargar et al. [103]. However, to the best of our knowledge there does not exist experimental data which systematically illustrates the relation between disorder concentration and resulting elastic properties for these colloidal crystals, so a direct comparison with the theoretically predicted values is not possible at this point in time. This is partly due to the fact that in oscillatory shear rheology experiments it is difficult to accurately control the defect concentration in the samples since the oscillatory perturbations can lead to the annealing of defects. This makes it necessary to use less intrusive approaches like measuring the propagation of shear waves in the sample or resorting to optical tweezers [personal correspondence with Prof. Joris Sprakel].

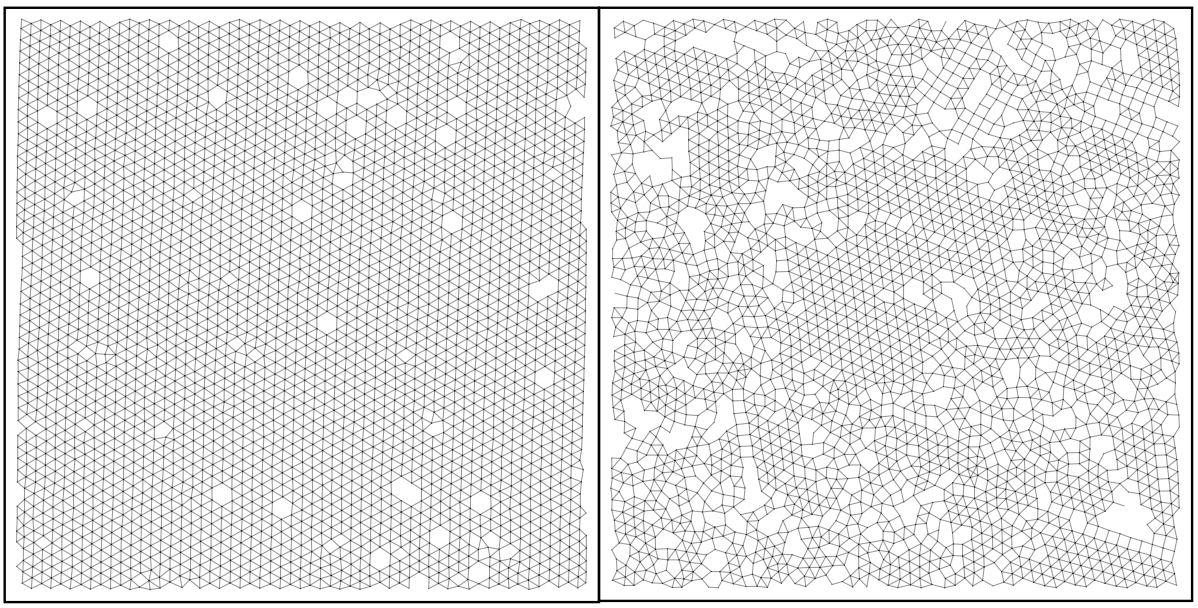

Fig. 2.7 Comparison of 2D slices of the vacancy fcc colloidal crystal prepared in Ref. [104] for low ($c = 0.0167$) and high ($c = 0.169$) vacancy concentration both at a volume fraction $\phi = 0.56$.

2.6 Conclusion

Using the non-affine lattice dynamical expressions and combinatorial bond counting, we found that the expressions for the shear moduli of bond-depleted and vacancy fcc crystals share an equivalent formal structure. They are connected via the transformation $p = 1 - c$ and a density rescaling proportional to $1 - c$, (where p is the fraction of depleted bonds and c the concentration of vacancies). This behaviour can be attributed to the fact that the average or global degree of inversion symmetry breaking controls the shear modulus of the disordered fcc crystal, and this inversion-symmetry breaking (ISB) parameter exhibits the exact same behaviour in the two systems under investigation (i.e. bond-depleted and vacancy lattice, respectively).

When describing the elastic properties of disordered solids, the equations of non-affine lattice dynamics reflect the fact that besides the standard Born-Huang affine contribution there is an additional non-affine contribution which leads to an effective elastic softening. This softening mechanism is closely related to the affine force field $\mathbf{\Xi}_i$ which represents the additional forces acting on a particle i due to the disorder-induced imbalance of forces, an effect rooted in the absence of local inversion symmetry in a disordered lattice.

In order to compute the non-affine correction to the shear modulus we have to average the affine force fields with respect to the disordered configurations of the crystal. So the shear modulus cannot depend on the local properties of the local degree of inversion

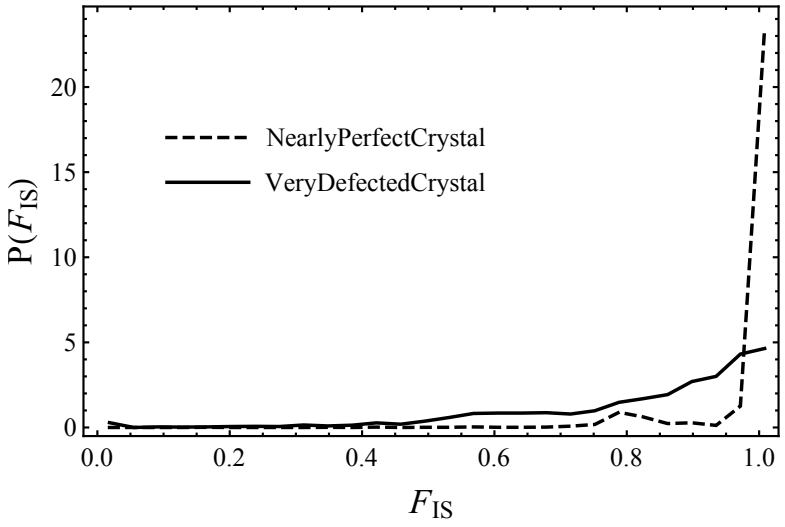

Fig. 2.8 The inversion symmetry parameter F_{IS} computed from the two 2D low and high vacancy concentration configurations shown in Fig. 2.7

symmetry breaking, because they are washed out by self-averaging in the process of taking the thermodynamic limit.

Furthermore, comparing the vibrational properties of the two disordered fcc crystals, we saw that the density of states of both systems are closely related up to high degrees of disorder. However, we also observed that the boson peak position ω_{BP} is generally shifted to lower frequencies in the case of the vacancy fcc. This is because the fluctuations of the ISB parameter, more than its mean value, control the behaviour of the boson peak. There are two closely linked quantities which account for the microstructure of

Table 2.1 Scaling of different physical quantities with $\bar{Z}$ for the depleted and vacancy fcc.

Quantity	Depleted	Vacancies
F_{IS}	$\frac{\bar{Z}-1}{11}$	$\frac{\bar{Z}-1}{11}$
G_{A}	$\frac{\bar{Z}}{12}$	$\frac{\bar{Z}^2}{12^2}$
G_{NA}	$\frac{12-\bar{Z}}{12}$	$\frac{\bar{Z}}{12}\frac{12-\bar{Z}}{12}$
G	$\frac{\bar{Z}-6}{6}$	$\frac{\bar{Z}}{12}\frac{\bar{Z}-6}{6}$
ω_{BP}	$\frac{\bar{Z}-6}{6}$	$\frac{\bar{Z}}{12}\frac{\bar{Z}-6}{6}$

the disordered fcc. The distribution of the connectivity Z can be intuitively understood. A narrowly peaked distribution, which was used for the bond-depleted fcc in this work, means that every particles in the system has approximately the same number of nearest

neighbours with a high probability. On the other hand, a broad Z-distribution tells us that the heterogeneity of the microstructure, and hence of the variation in the number of nearest neighbors, is large.

The connection to the inversion symmetry breaking parameter is made easily. A configuration with a large degree of Z spatial fluctuation directly leads to a heterogenous distribution of the ISB parameter. Highly coordinated sites retain most of their bond symmetry and lead to F_{IS} values close to one. A larger spread of local coordination numbers Z yields a broader distribution $P(F_{\mathrm{IS}})$. When the Z-fluctuations in the system are large we can conclude that we have a relative excess of low-coordinated particles with respect to a system with a narrower Z-distribution. Since these low-coordinated sites are connected to a smaller number of bonds, it takes a smaller amount of energy to excite vibrations at this site due to the fact that they effectively have a lower binding energy.

In turn, these low-energy excitations translate to an increased population of modes at low frequencies. Therefore, the low-frequency part of the DOS, together with the boson peak at ω_{BP}, moves to lower frequencies.

Following this argument, the boson peak of the vacancy fcc is always shifted to lower frequencies with respect to the depleted fcc due to larger fluctuations of the local degree of inversion symmetry. This behaviour is clearly seen from the numerical solution of the non-affine lattice dynamics of the depleted and vacancy fcc, which also holds true for the depleted fcc with a wide Z-distribution.

In conclusion, our analysis of the vibrational properties and shear elasticity within the framework of non-affine lattice dynamics, has made it possible to identify the microscopic source and the nature of the disorder and heterogeneous fluctuations that have served in previous theoretical studies based on fluctuating elasticity models [64, 77, 78] as the input to explain the boson peak in disordered solids and its link with soft elasticity. In addition to that, it will be interesting to see in future experimental studies what precise implications fluctuations in the degree of microstructural disorder have in terms of the vibrational properties and elastic response of colloidal suspensions and how they compare to the theoretical considerations laid out in this chapter.

Chapter 3

Elastic Correlations in disordered lattices with long-range interactions

3.1 Introduction

It is well known that introducing disorder into solids leads to the appearance of elastic heterogeneities which are spatial fluctuations of the local elastic moduli of a disordered solid. For instance, this phenomenon was characterised in term of the increasing local elastic fluctuations across an amorphisation transition in an fcc crystal [68]. Studying the fluctuation patterns of local elastic moduli naturally leads to the question if and how these fluctuations are correlated throughout in space and time. For example, the spatial elastic correlations in a 2D binary mixture of soft spheres and a 3D Lennard-Jones system were investigated via molecular dynamics (MD) simulations in Ref. [17]. The authors have shown that these systems exhibit long-range spatial stress correlations proportional to r^{-2} in the three-dimensional liquid state, where r represents radial distance. Similar findings have been brought forward for metallic glass systems [92], where elastic heterogeneities were observed experimentally. Going beyond the mere observation and description of correlations between elastic heterogeneities, a recent simulation study points to a striking physical consequence of them. In Ref. [42], simulations of a binary soft sphere glass were carried out to obtain equilibrated glassy configurations. These were then used as an input to study the propagation of vibrational excitations in the system by numerically solving the classical equation of motion. The solutions are then used to obtain the velocity autocorrelation function. Since the topology of underlying glassy configuration is disordered, the vibrational excitations experience scattering and subsequent damping characterised by the phonon damping coefficient $\Gamma(q)$, which can be obtain by fitting the oscillatory decaying velocity autocorrelation function. The main finding of this

study this that the phonon damping coefficient shows the scaling $\Gamma(q) \propto -q^{d+1} \log q$ at low wave vectors $q = |\boldsymbol{q}|$. This represents a striking deviation from the $\Gamma(q) \propto q^{d+1}$ scaling which is predicted for scattering of phonons at random impurities known as the Rayleigh scattering. The authors conclude that the presence of the above-mentioned inverse power-law elastic correlations leads to a modification of the mechanism which scatters phonons at very low-frequencies manifesting itself in a logarithmic enhancement of the wave-vector dependence of the Rayleigh scattering law.

Bearing in mind the interesting effects elastic correlations cause in terms of the scattering physics of phonons, we set out to systematically study how long-range elastic correlations develop in a simple model system in dependence on the degree of disorder and the range of the microscopic interactions. The central idea is to use a two-dimensional triangular central-force lattice subject to bond-depletion to introduce disorder. In the numerical and experimental systems referred to above, the underlying interaction of the investigated systems have a long-range character, either being a Lennard-Jones potential in the case of the MD simulation or a more complicated metallic interaction potential. For this reason we want to shed some light on the effect of the range of the interaction has on the elastic heterogeneities and its correlation structure. In a lattice systems like a triangular lattice it is quite simple to tune the range of the interaction just by introducing bonds which not only connect the nearest neighbours of the each particle, but also particles farther away, i.e. next-to-nearest neighbours and beyond. In this way we naturally introduce interaction shells into the lattice, as can be seen in Fig. 3.1.

3.2 Triangular lattice with long-range bonds

3.2.1 Model

In the case where only nearest-neighbour interactions are considered we only have one shell of interacting neighbours, which we will to refer as a $S = 1$ system. This shell is shown in red in Fig. 3.1. In the same way we consider the triangular lattice with longer-range interactions, where the particle interacting with the central particle are located on shells. The corresponding harmonic central-force interaction potential is given by

$$V_S(|\boldsymbol{r}|) = \frac{1}{2} \sum_{\langle i,j \rangle} \kappa_{ij} \Big[(\boldsymbol{u}_i - \boldsymbol{u}_j) \cdot \hat{\boldsymbol{n}}_{ij} \Big]^2 \tag{3.1}$$

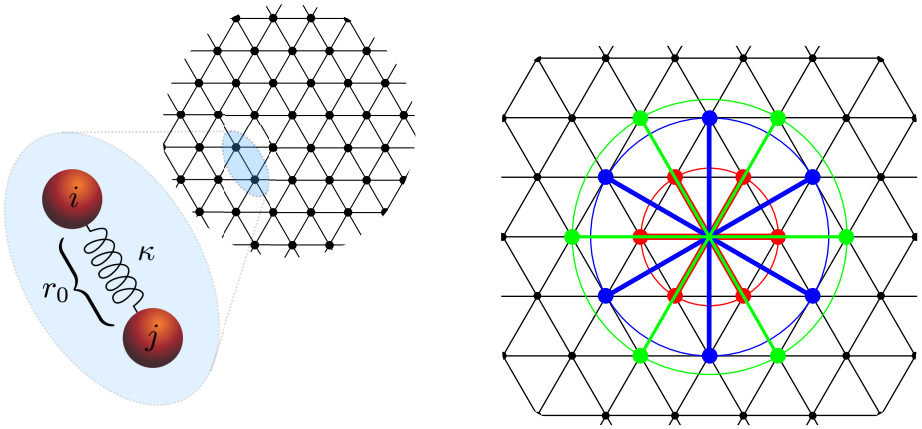

Fig. 3.1 Sketch of the triangular lattice which serves as the model system. The left panel shows a typical bonds of rest length r_0 and spring constant κ. The right panel shows the first three interaction shells in the lattice. Note that the radii of the shells are not equidistant.

where $\langle i, j \rangle$ denotes the summation over the bonds which are situated in the interaction shell S at distance $r_S = |\boldsymbol{r}_S|$ and κ_{ij} is the interaction strength depending on the distance between the two lattice sites. This means that, we write the full interaction potential of the lattice as a decomposition into the different interaction shells as

$$U_S(|\boldsymbol{r}|) = \sum_{s=1}^{S} V_s(|\boldsymbol{r}|) \tag{3.2}$$

where S is the maximal interaction range in the lattice. In the right-hand panel of Fig. 3.1 we show the first three interaction shells on the triangular lattice. For the numerical computations we use a 77×78 triangular lattice with $N = 6006$ particles with periodic boundary conditions.

The harmonic bonds in each shell have their individual rest length, so that there appear no internal stresses. Importantly, we now make the assumption that the interaction strength κ_{ij} depends on the radius of the interaction shells and decays as

$$\kappa_{ij}(|\boldsymbol{r}|) = \kappa(r_{ij}) = \frac{1}{|\boldsymbol{r}_i - \boldsymbol{r}_j|^{\alpha}} \tag{3.3}$$

For reasons that will become evident later in terms of the correlation structure, all numerical computations of physical quantities of the long-range triangular lattice were carried out with the power-law exponent $\alpha = 3$. A prerequisite for the analysis of elastic heterogeneities and correlations in the lattice is the implementation of disorder. We will achieve this by depleting the existing bonds in the lattice. A bond is chosen at random

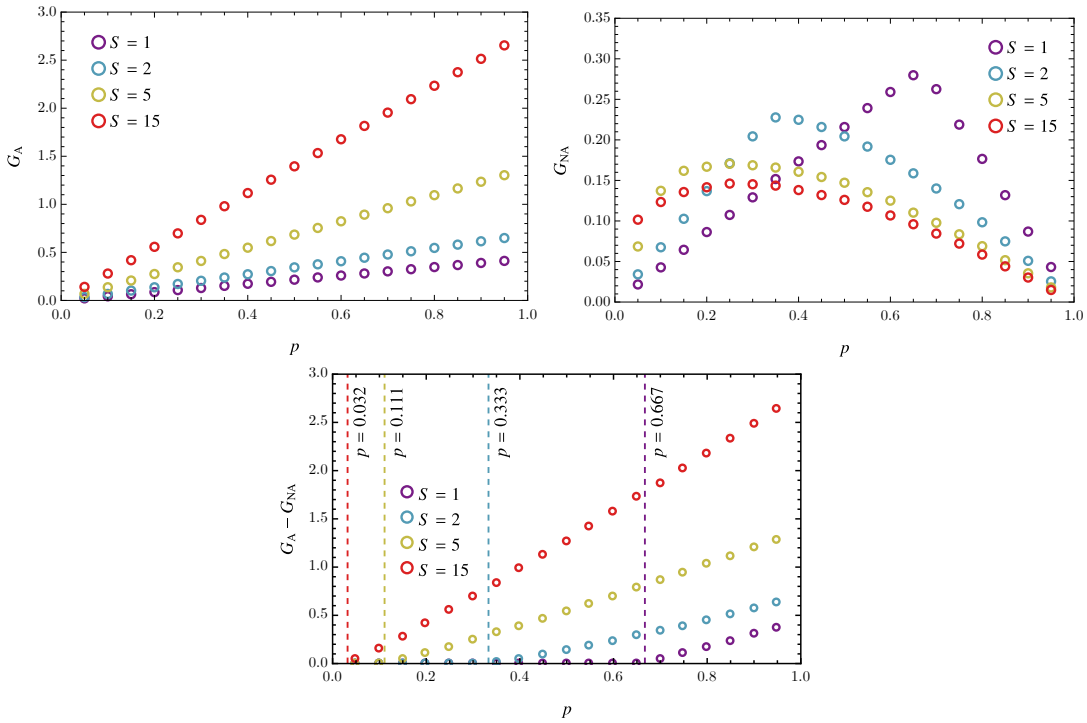

Fig. 3.2 The affine, non-affine and full shear moduli of the triangular for the four interaction ranges $S = 1$, 2, 5, and 15 plotted against the bond-occupation probability p. The dashed lines in the lower panel show the respective critical bond-occupation probabilities.

and subsequently cut with a probability $1 - p$ and left intact with probability p. Hence, a bond between two arbitrary sites i and j appear as a Bernoulli random variable.

Initially, the perfect lattice has an average coordination number $Z_{0,S}$, which depends on the number of interaction shells present in the lattice. The nearest-neighbour lattice $S = 1$ has $Z_{0,1} = 6$. In the case of $S = 2$ the coordination number consists of contributions from the first and second shell adding to a total of $Z_{0,2} = 12$ bonds. The random depletion of bonds means that a given site has the average local coordination number

$$\langle Z_S \rangle = \sum_{n=0}^{Z_{0,S}} n \binom{Z_{0,S}}{n} p^n (1-p)^{Z_{0,S}-n} = Z_{0,S} p \tag{3.4}$$

where $\binom{Z_{0,S}}{n}$ is the Binomial coefficient accounting for different ways of occupying n of the $Z_{0,S}$ bonds. It is in principle possible to deplete different shells with different depletion probabilities, which means that the rigidity transition where the shear modulus of the system vanishes is approached via different paths in the parameter space spanned by the shell-dependent depletion probabilities p_s. For a square lattice with next-to-nearest neighbour interactions this has been considered in Ref. [33].

3.2.2 Rigidity transition and long-range bonds

As we have seen in Chapter 1, where we discussed the non-affine quasi-static framework, the shear modulus can expressed in terms of the affine and non-affine contributions as $G = G_{\mathrm{A}} - G_{\mathrm{NA}}$. The results of the numerical computations of all contributions are plotted separately in Fig. 3.2. The most important characteristic to notice at this point is the movement of the critical bond-occupation probability p_c to lower values when the maximal interaction range S is increased. The point where the zero-frequency elastic moduli is also called the rigidity percolation threshold, or point of marginal stability [46]. It is the transition point where the lattice loses its mechanical stability and can no longer sustain external loads. For two-dimensional central-force networks this critical point is reached when the average connectivity $\langle Z \rangle = 4$, a result which is due to the classical Maxwell constraint counting argument. It says that the transition from a rigid to a floppy state in a central-force network occurs when the number of degrees of freedom, which in the central-force case is the space dimension d times the number of particles N, equals the number of constraints in the lattice [23]. The constraint in the lattice arise to the particles being linked by bonds, hence, the number of constraints in the nearest-neighbour case is given by $\langle Z \rangle N/2$. Equating these two expression we obtain the criterion for the critical point of the rigidity transition, which occurs at an average coordination number of $\langle Z \rangle = 2d$, which in the present case of the triangular lattice gives $\langle Z \rangle = 4$. The triangular lattice loses its mechanical stability when on average each particle is connected to four neighbouring particles.

In the language of the bond-occupation probability, this means that in the case of the nearest-neighbour triangular lattice, $S = 1$, the point of marginal stability is reached at $p_c = 2/3$, which is clearly seen in Fig. 3.2. Adding also next-to-nearest-neighbor bonds in the lattice leads to a shift of the critical value p_c to lower values. As discussed in [34] from the point of view of an effective-medium approach, the theoretically predicted mean-field value for the critical bond-occupation probability is $p_c = 1/3$. This is in agreement with our numerical calculation, shown in Fig. 3.2. Using the considerations which are presented in Ref. [33], we can determine the surface across which the rigidity transition takes place for central-force networks according to

$$\sum_{i}^{S} z_i p_{c,i} = 2d \tag{3.5}$$

where d is the dimension of the lattice under consideration and the sum extends up to the desired shell range. Since we choose to deplete all bonds irrespective of the bond

length, we set $p_{c,i} = p_c$. For $S = 2$, 5, and 15 using this relation we obtain $p_c = 1/3, 1/9$ and $2/63$.

3.3 Local elastic moduli

The analysis of elastic heterogeneities and their correlation structure requires a well-defined notion of the local elastic moduli. Since the underlying framework which we will be using for this analysis is non-affine lattice dynamics, we now introduce the locally defined affine and non-affine shear moduli. As introduced in Chapter 1, the affine contribution of the shear modulus for central-force lattices may be written as a sum over components of the unit bond vectors, i.e.

$$G_{\mathrm{A}} = \frac{1}{2V} \sum_i \sum_j \kappa_{ij} \left(r_{ij} n_{ij}^x n_{ij}^y \right)^2 \tag{3.6}$$

where the summation of the index j extends over all neighbours of the i^{th} particle. The local affine moduli at site i is then just the i^{th} partial sum in the above expression. Importantly, each contribution to the affine modulus corresponding to a particular bond in the system is weighted with the rest length and interaction strength of that particular bond.

For our description of the spatial elastic correlations in the lattice it is vital to also express the local contribution to the non-affine modulus. That is, as already pointed out above for the affine modulus, we want to split the non-affine modulus into contributions from each lattice site. Since we consider a disordered triangular lattice there will be a correction term to the elasticity which accounts for the deviations from the homogeneous pure shear deformations seen in the perfect lattice. We describe this non-affein correction in terms of the affine force field $\boldsymbol{\Xi}$ which arises due to the force imbalances in the disordered lattice configurations. These force fields drive the non-affine displacements of particles which are characteristic for the elastic response of disordered systems. Essentially, these additional displacements, or relaxations, lead to a weakening of the overall linear elastic response, which is summarised by the relation $G = G_{\mathrm{A}} - G_{\mathrm{NA}}$. In order to properly define the local contributions to the non-affine elasticity we recall the definition of the non-affine displacement fields provided in Eq. (1.24) as

$$\delta \boldsymbol{r}_{\mathrm{NA}} = \boldsymbol{H}^{-1} \boldsymbol{\Xi}. \tag{3.7}$$

This non-affine displacement vector has dN components and we straightforwardly obtain the local displacement field of particle i by only considering the components associated with the i^{th} particle. Making use of the Dirac notation we express the local non-affine displacement field of particle i by projecting $|\delta \boldsymbol{r}_{\text{NA}}\rangle$ onto the coordinate vector $|\boldsymbol{i}\rangle$, i.e.

$$\delta \boldsymbol{r}_{\text{NA,i}} = \langle \boldsymbol{i}| \, \delta \boldsymbol{r}_{\text{NA}}\rangle = \langle \boldsymbol{i}| \, \boldsymbol{H}^{-1} |\boldsymbol{\Xi}\rangle. \tag{3.8}$$

This is clearly nothing but defining a projection on the lattice sites by $|\boldsymbol{i}\rangle\langle\boldsymbol{i}|$, where $|\boldsymbol{i}\rangle$ denotes the dN-dimensional basis vector of the particle basis. In the particle or equivalently lattice site basis we then write the decomposition of the non-affine displacement field as

$$|\delta \boldsymbol{r}_{\text{NA}}\rangle = \sum_{i \in \text{sites}} |\boldsymbol{i}\rangle \left\langle \boldsymbol{i}| \, \boldsymbol{H}^{-1} \boldsymbol{\Xi} \right\rangle \tag{3.9}$$

such that the scalar product in the particle basis $\left\langle \boldsymbol{i}| \, \boldsymbol{H}^{-1} \boldsymbol{\Xi} \right\rangle$ is d-dimensional and represents the response to the affine force field acting at site i. Following the exposition in Chapter 1, the non-affine contribution to the modulus is then given by multiplying with $\boldsymbol{\Xi}$ from the left, i.e.

$$G_{\text{NA}} = \frac{1}{V} \langle \boldsymbol{\Xi}| \, \delta \boldsymbol{r}_{\text{NA}}\rangle = \frac{1}{V} \sum_{i \in \text{sites}} \langle \boldsymbol{\Xi} \, |\boldsymbol{i}\rangle \langle \boldsymbol{i}| \, \boldsymbol{H}^{-1} \boldsymbol{\Xi}\rangle. \tag{3.10}$$

Using the completeness of the eigenbasis of the Hessian, i.e. $\mathbb{1} = \sum_p |\boldsymbol{p}\rangle\langle\boldsymbol{p}|$, we can write the i^{th} contribution as

$$G_{\text{NA},i} = \frac{1}{V} \sum_p \frac{1}{\lambda_p} \langle \boldsymbol{\Xi}| \, \boldsymbol{i}\rangle \, \langle \boldsymbol{i}| \, \boldsymbol{p}\rangle \, \langle \boldsymbol{p}| \, \boldsymbol{\Xi}\rangle \tag{3.11}$$

where the scalar product $\left\langle \ldots | \, \boldsymbol{i} \right\rangle$ denotes the projection of the dN-dimensional onto the lattice site $\boldsymbol{i}$. The summation is carried out over all eigenmodes of the Hessian such that the eigenvalues fullfill $\lambda_p \neq 0$. Summing Eq. (3.11) over all lattice sites $\boldsymbol{i}$ returns the full non-affine shear modulus, as we would expect. In summary, the full locally-defined shear modulus is

$$G_i = G_{\text{A},i} - G_{\text{NA},i} \tag{3.12}$$

At this point it is crucial to note that even though we set out to define a local contribution to the non-affine shear modulus, it is not a truly local quantity like its affine counterpart.

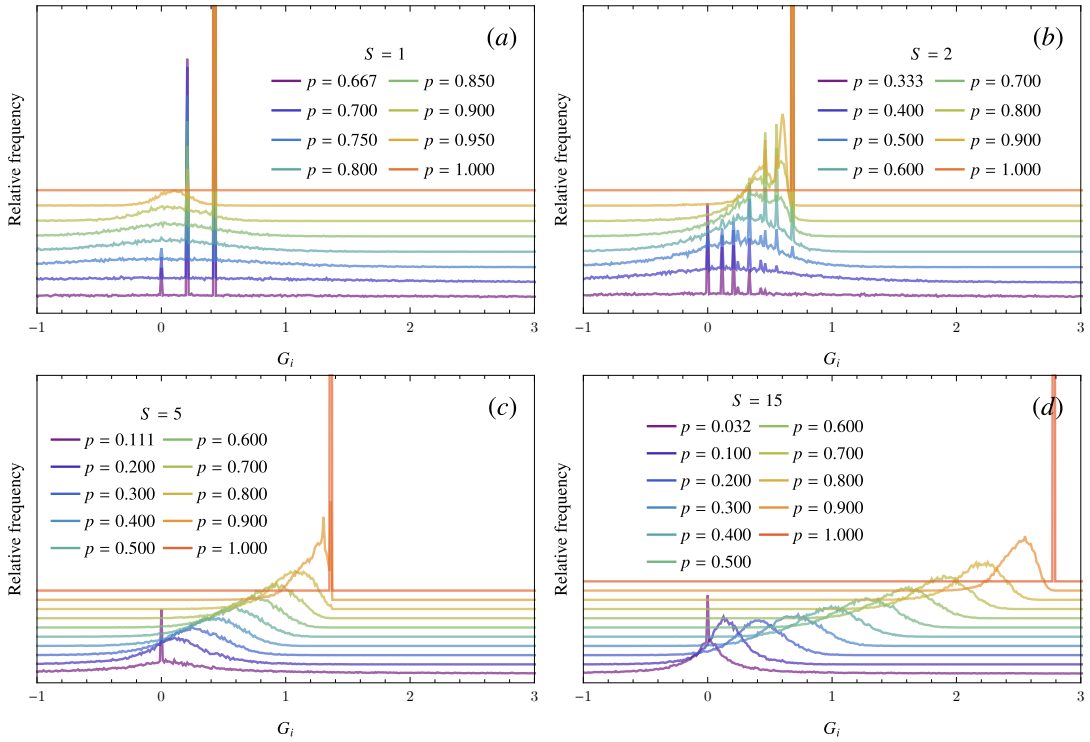

Fig. 3.3 Bond-depletion in the long-range triangular lattice leads to different distribution of the local shear moduli G_i depending upon the maximal interaction range of the bonds, which manifestly are elastic heterogeneities. The panels show the relative frequencies of local moduli in the triangular different maximum interaction ranges S =1, 2, 5, and 15. Curves for different values of p are shifted vertically for visual clarity.

In addition to the i^{th} component of the affine force field, the local non-affine modulus is multiplied with the projection of the full affine force field onto the eigenvector belonging to a certain mode. Clearly, this factor contains contributions from all sites in the system, and we therefore can say that $G_{\text{NA,i}}$ is a non-local quantity. From a physical point of view this is certainly not unreasonable. The non-affine displacements represent the onset of local rearrangements [62]. These particles can have large displacement vectors and as a result other particles would also have to undergo displacments to move out of the way to accommodate these rearrangements.

3.4 Appearance of elastic heterogeneities

Having studied the properties of the global averaged shear modulus of the lattice in terms the long-range interactions, it is now time to extend the analysis and look at

the distribution of the local elastic moduli to get insight into the nature of the elastic heterogeneities in the case where $\kappa(r_s) = r_s^{-3}$.

As evident from Fig. 3.3, in the perfect lattice, that is in the case where $p = 1$, all bonds are occupied, the distribution on local elastic moduli is represented by a single δ-peak. In the absence of disorder each lattice site has the same number of neighbours and the local moduli are given by $G_{\mathrm{A},i} = G_i$, since due to the full local inversion symmetry the non-affine moduli are zero everywhere. The value of $G_{\mathrm{A},i}$, which represents the position of the δ-peak in the local moduli distribution in Fig. 3.3, moves to higher value with increasing the maximum allowed bond length.

As the bond-occupation probability p is reduced, the evolution of the local moduli distribution starts to differ significantly for different shells values. In the nearest-neighbour case, $S = 1$, the single δ-peak at $G_{\mathrm{A},i} = \sqrt{3}/4$ remains for all p values. However, in addition two new δ-peaks develop when p is lowered. The strong dominance of the three discrete peaks reflects the fact that in the nearest-neighbour case only a small number of bond-configurations is possible for a given bond-occupation. Looking at the situation when long-range bonds are put into the lattice, the shape of the local moduli distribution starts to depart from the δ-shape drastically. From inspection of Fig. 3.3, we see that going to higher shell numbers, these discrete peaks are gradually washed out and a smoother distributions are obtained. In addition to that, the distribution of local shear moduli in Fig. 3.3 can be observed to spread into the negative domain in some cases. This means that as a consequence of randomly cutting bonds, at some lattice sites the local non-affine contribution becomes large enough to overwhelm its affine counterpart, leading to negative values of $G_i = G_{\mathrm{A},i} - G_{\mathrm{NA},i}$. The resulting negative local moduli are linked to local mechanical instabilities [98]. They represent a negative linear response to an applied stress and consequently the system can spontaneously relax via a locally confined non-affine displacement instead of resisting the applied stress as in the case of a positive local modulus. This phenomenon has been attributed to local plastic events [92, 71] potentially representing precursors to large-scale plastic rearrangements, which occur in real disordered materials and glasses. In order to quantitatively grasp the change of the local moduli distribution, it is instructive to describe the development of the distributions in term of their fluctuations, quantified by the variances $\mathrm{var}(G_{\mathrm{A}}) = \langle G_{\mathrm{A}}^2 \rangle - \langle G_{\mathrm{A}} \rangle^2$ and $\mathrm{var}(G_{\mathrm{NA}}) = \langle G_{\mathrm{NA}}^2 \rangle - \langle G_{\mathrm{NA}} \rangle^2$.

The variance of the affine local moduli distribution is characterised by a parabolic shape, as can be see from Fig. 3.4 (a). The variance $\mathrm{var}(G_{\mathrm{A}})$ is zero at $p = 1$ which corresponds to the δ-peak in the distribution of the local moduli G_i. This is also the case at $p = 0$ where all local affine moduli are zero in this situation. We can clearly

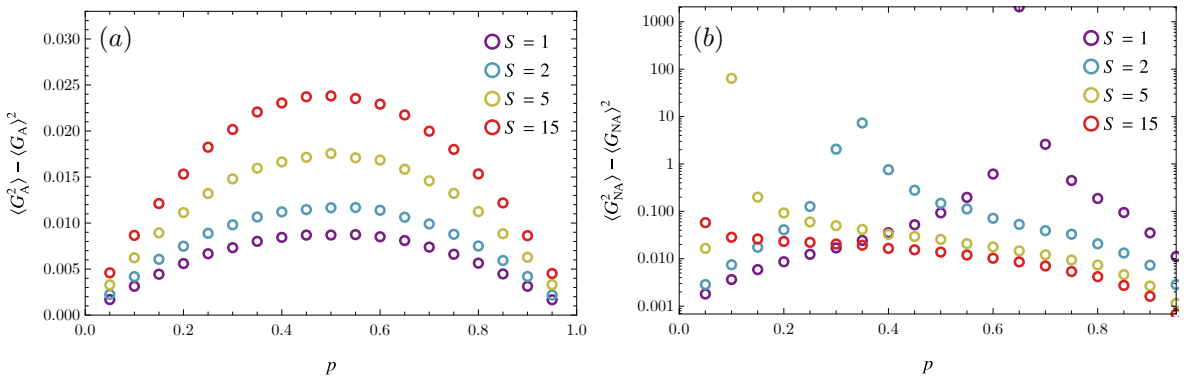

Fig. 3.4 The scaling of the variances of the distribution of the affine and non-affine local elastic moduli for the four interaction range under investigation. It is evident that var(G_{A}) is enhanced when increasing the maximal interaction range, whereas var(G_{NA}) experiences attenuation above p_c.

observe that the increase of the maximal interaction range in the lattice from $S = 1$ to $S = 15$ leads to an increase in the variance of the local moduli. The broadening of the distribution of $G_{\mathrm{A},i}$ with increasing S at fixed p results from the fact the average number of bonds per particle quickly increases with S. Consequently, the system has significantly more bond configurations to choose from.

Focusing on Fig. 3.4 (b), which is a logarithmic plot, it is directly evident that the fluctuations of the non-affine moduli behave quite differently. Firstly, we notice that var(G_{NA}) exhibits a divergence at the values of p which correspond to the respective isostatic points for the four different lattices with $S = 1$, $S = 2$, $S = 5$, and $S = 15$. Another main characteristic is that for fixed $p > p_c$ the fluctuations of the non-affine moduli experience an attenuation as S is increased. These opposing trends of var(G_{A}) and var(G_{NA}) which appear with varying the interaction range will become important later on and will have a direct impact on the spatial correlation structure.

3.5 Analytical scaling of the affine elastic autocorrelation

Having established the heterogeneities of the affine and non-affine local moduli in terms of their fluctuations, we now want to go further and study the spatial correlations of these fluctuations on the lattice. The affine local moduli are given in terms of the bond vectors and for this reason can be thought to represent the structural topology of the disordered lattice. This is in contrast to the non-affine modulus which involves the eigenvectors of

the full Hessian matrix. For this reason there is hope to obtain an analytical scaling relation for the radial part of the affine autocorrelation structure.

Since we need tools to characterise the correlation of the elastic heterogeneities in the long-range triangular lattice, we continue by reviewing the standard definitions of the correlation functions and the correlation coefficient. In particular, we are interested in the radial elastic autocorrelation function of the form

$$C(r) = \frac{\left\langle\!\left\langle G(0)G(r)\right\rangle\!\right\rangle - \left\langle\!\left\langle G(0)\right\rangle\!\right\rangle\left\langle\!\left\langle G(r)\right\rangle\!\right\rangle}{\left\langle\!\left\langle G(0)^2\right\rangle\!\right\rangle - \left\langle\!\left\langle G(0)\right\rangle\!\right\rangle^2} \tag{3.13}$$

where $r = |\boldsymbol{r}|$ denotes the norm of the distance vector between lattice site and with $\langle\!\langle \ldots \rangle\!\rangle$ we mean the lattice site and configurational disorder average defined on the triangular lattice with long-range interactions. This means we have to write the above expression as a sum over lattice sites.

Therefore, we consider the spatial autocorrelation function of a physical quantity f which is defined at each lattice site. Hence, with $f(i) = f_i$ we mean the value of the function f at lattice site i. The radial dependence of the spatial autocorrelation of f is then described by

$$C_f(r) = \frac{\frac{1}{N}\sum_{i,j=1}^{N}\Big(\left\langle f_i f_j\right\rangle - \left\langle f_i\right\rangle\left\langle f_j\right\rangle\Big)\Big|_{r=r_{ij}}}{\left\langle f^2\right\rangle - \left\langle f\right\rangle^2}. \tag{3.14}$$

In the above equation $\langle \ldots \rangle$ denotes the disorder average over different realisations. The summation over j is done under the requirement that $r = r_{ij}$ be fulfilled and subsequently the average over all lattice sites is carried out by summing over i. The mean $\langle f \rangle$ is obtained by the average taken over all lattices sites and configurations.

As we will see, it is possible to obtain an analytical scaling relation between the affine elastic correlations and the decay rate of the harmonic interaction strength with shell distance r_S. Specifically, we will derive that if the r-dependent stiffness $\kappa(r)$ decays as a power law of the radius of the shells of the long-range interaction leads to a power-law decay of the angular average of the affine elastic autocorrelation function Choosing a spring constant or interaction strength with a power-law decay, i.e. $\kappa \sim r^{-\alpha}$, the spatial correlation function of the affine shear modulus subsequently scales as $C_r \sim r^{4-2\alpha}$.

The central idea for achieving this result is to exploit the fact that on the lattice we can naturally split the contributions to G_A into the parts coming form the distinct shells. As discussed above, the six nearest-neighbour bonds are arranged on a circle of radius 1, the next-to-nearest-neighbour bonds can be found on a circle of radius $\sqrt{3}$ and

so on. Since the affine modulus is defined as a sum over the corresponding unit bond vectors $\hat{\boldsymbol{n}}_{ij}$, we can decompose G_{A_i} into distinct contribution from shells with given radii. For the remainder of this section we will drop the subscript in the notation of the affine modulus for visual clarity, and therefore identify $G_{\mathrm{A}} \equiv G$. We recall that the local affine elastic modulus is given by the expression

$$G_i = \frac{1}{2V} \sum_{j=1}^{N} \kappa_{ij} \left(r_{ij} n_{ij}^x n_{ij}^y \right)^2 \tag{3.15}$$

where $\kappa_{ij} = \kappa(r_{ij})$ is the distance-dependent spring constant specifying the strength of the harmonic interaction between particle i and j. Since the above sum runs over all neighbours connected to particle i, we decompose the summation into contribution from different interaction shells. Therefore we write

$$G_i = \sum_{s}^{S} G_{i,s} \tag{3.16}$$

such that $G_{i,s}$ is the contribution to the affine modulus at i coming from bonds which connect particle i with the particles in shell s at distance r_s. The first term we want to treat is $\langle G(0)G(r) \rangle$, where r is restricted to the interaction shell with index t at range r_t, i.e.

$$\begin{aligned} \langle G(0)G(r_t) \rangle =& \frac{1}{N} \sum_{i=1}^{N} \left\langle \frac{1}{N_t} \sum_{j=1}^{N_t} G_i G_j \right\rangle \Big|_{r_{ij}=r_t} \\ =& \frac{1}{N} \sum_{i=1}^{N} \frac{1}{N_t} \sum_{j=1}^{N_t} \sum_{s,s'}^{S} \langle G_{i,s} G_{j,s'} \rangle \Big|_{r_{ij}=r_t} \end{aligned} \tag{3.17}$$

noting that the summation over index j is restricted to $r_{ij} = r_t$. At this point we implicitly assume that N_t represents the average number of particles present in shell t, i.e. $\langle N_t \rangle = N_t$.

The crucial step in order to continue is now to split the sum over the two shell indices, s and s', into diagonal and off-diagonal parts. This means

$$\begin{aligned} \sum_{s,s'} G_{i,s} G_{j,s'} =& \sum_{s} G_{i,s} G_{j,s} + \sum_{\substack{s,s' \\ s \neq s'}} G_{i,s} G_{j,s'} \\ =& G_{i,t} G_{j,t} + \sum_{\substack{s \\ s \neq t}} G_{i,s} G_{j,s} + \sum_{\substack{s,s' \\ s \neq s'}} G_{i,s} G_{j,s'}. \end{aligned} \tag{3.18}$$

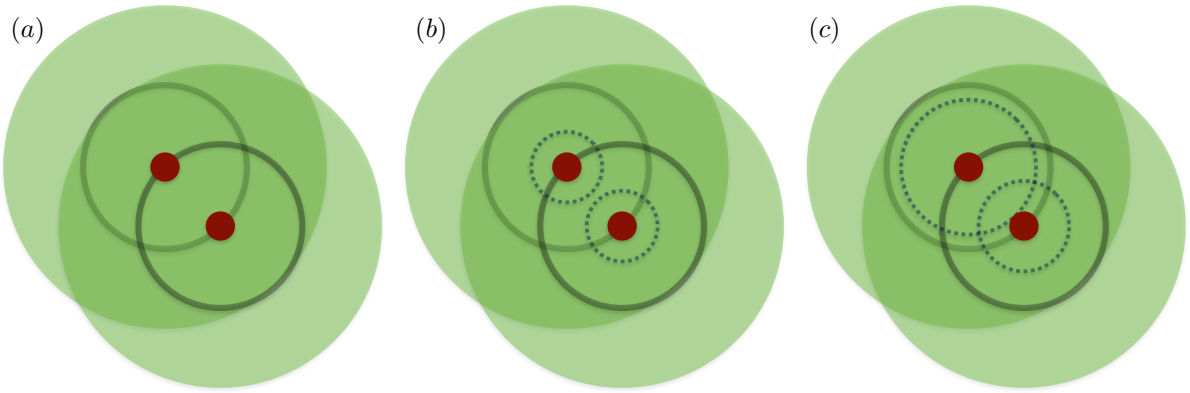

Fig. 3.5 Illustration of the three contribution when splitting the covariance $\langle G_i G_j \rangle$.

In terms of the physical picture, the first term in the above equation represents the special case where particle j is the t-shell of particle i and vice versa. Crucially, this means that in this case inevitably there is a direct bond between particle i and j. When taking the configurational disorder average of this term, and the shared bond between the two particles happens to be removed, this has the consequence that $G_{i,t}$ varies together with $G_{j,t}$. Or in other words, the two quantities are correlated. This situation is illustrated schematically in Fig. 3.5 (a). The second summand in Eq. (3.18), which is the rest of the diagonal contribution, contains the terms which account for the i and j moduli coming from equal interaction ranges. The two possibilities are that the index is too small for site i and j to share a bond with a third site k, since j is restricted by $r_{ij} = r_t$, as depicted in Fig. 3.5 (b). Alternatively, it can happen that i and j are both connected to a common site k. This for example happens when j is on the $t = 2$ shell of particle i, and we consider the $s = 1$ of the diagonal sum. This case is shown in Fig. 3.5 (c) However, again taking the disorder average, cutting the $i - k$ has no effect on the $k - j$ bond. Thus, these terms will not contribute to the correlation between site i and j. The same explanation carries over to the third summand in Eq. (3.18), with the difference that in this situation the bonds between i and k and k and j do not have the same length. The implication is that the statistical average of terms do not correlate, by which we mean that $\langle G_{i,s} G_{i,s'} \rangle = \langle G_{i,s} \rangle \langle G_{i,s'} \rangle$. Note that this is a consequence of the fact that we only consider bond-depletion as a mechanism to induce disorder in the lattice. In the case of positional disorder, for instance, the above line of reasoning would not be correct.

Taking this into account we conclude that Eq. (3.18) may be written as

$$\langle G(0)G(r_t)\rangle = \frac{1}{N}\sum_{i=1}^{N}\frac{1}{N_t}\sum_{j=1}^{N_t}\left[\langle G_{i,t}G_{j,t}\rangle + \sum_{\substack{s,s'\\ s\neq s'\neq t}}^{S}\langle G_{i,s}\rangle\langle G_{j,s'}\rangle\right]. \tag{3.19}$$

To continue, we have to discuss the product of the averages given by $\langle G(0)\rangle$ and $\langle G(r_t)\rangle$, which subtracts $\langle G(0)G(r_t)\rangle$ in the full expression of the elastic autocorrelation function. Employing the same shell-wise decomposition as before we have

$$\begin{aligned}\langle G(0)\rangle\langle G(r_t)\rangle =& \frac{1}{N}\sum_{i=1}^{N}\langle G_i\rangle\langle\frac{1}{N_t}\sum_{j=1}^{N_t}G_j\rangle\Big|_{r_{ij}=r_t}\\ =& \frac{1}{N}\sum_{i=1}^{N}\sum_{s}\langle G_{i,s}\rangle\frac{1}{N_t}\sum_{j=1}^{N_t}\sum_{s'}\langle G_{j,s'}\rangle\Big|_{r_{ij}=r_t}\\ =& \frac{1}{N}\sum_{i=1}^{N}\frac{1}{N_t}\sum_{j=1}^{N_t}\left[\langle G_{i,t}\rangle\langle G_{j,t}\rangle + \sum_{\substack{s,s'\\ s\neq s'\neq t}}^{S}\langle G_{i,s}\rangle\langle G_{j,s'}\rangle\right].\end{aligned} \tag{3.20}$$

At this point we recognise that the off-diagonal sums in brackets in both Eq. (3.19) and Eq. (3.20) are equivalent. Therefore, considering the difference of both expressions we obtain the intermediate result stating that

$$\begin{aligned}\langle G(0)G(r_t)\rangle - \langle G(0)\rangle\langle G(r_t)\rangle =& \frac{1}{N}\sum_{i=1}^{N}\frac{1}{N_t}\sum_{j=1}^{N_t}\left[\langle G_{i,t}G_{j,t}\rangle - \langle G_{i,t}\rangle\langle G_{j,t}\rangle\right]\\ =& \frac{1}{N}\sum_{i=1}^{N}\frac{1}{N_t}\sum_{j=1}^{N_t}\langle G_{i,t}G_{j,t}\rangle - \langle G_t\rangle^2\end{aligned} \tag{3.21}$$

since $\frac{1}{N}\sum_{i=1}^{N}\langle G_{i,t}\rangle = \frac{1}{N_t}\sum_{j=1}^{N_t}\langle G_{j,t}\rangle = \langle G_t\rangle$ holds in the thermodynamics limit where $N\to\infty$. The quantity $\langle G_t\rangle$ is the average contribution coming from shell t at distance r_t.

It now remains to evaluate the correlation term of the t-shell contributions between particle i and j. For this we again look at the situation that in the above summation the j^{th} particle lies on the t-shell of particle i. This means that the sum $\sum_{j=1}^{N_t}G_{j,t}$ contains all bonds which are included in the term $G_{i,t}$, because these bonds are shared between the two sites. In addition, $\sum_{j=1}^{N_t}G_{j,t}$ contains bonds which are non connected to the lattice site i, and thus cannot contribute to the overall correlation encoded in the summands

$\langle G_{i,t}G_{j,t}\rangle$. Formalising this idea, we write

$$\sum_{j=1}^{N_t} G_{j,t} = G_{i,t} + \sum_{j=1}^{N_t} R_j \tag{3.22}$$

where R_j represent the residual bonds connecting to the j sites which are not shared by the central site i. Considering the configurational average of the residual terms R_j we realise that on average the bond structure as seen from each j-site looks the same. This means averaging over all the bonds emanating from j-sites which are not shared with the central site i gives

$$\left\langle \sum_{j=1}^{N_t} R_j \right\rangle = (N_t - 1)\langle G_t\rangle. \tag{3.23}$$

We substitute this result into Eq. (3.21) and continue with

$$\begin{aligned}
\frac{1}{N}\sum_{i=1}^{N}\frac{1}{N_t}\sum_{j=1}^{N_t}\langle G_{i,t}G_{j,t}\rangle - \langle G_t\rangle^2 =& \frac{1}{N}\sum_{i=1}^{N}\frac{1}{N_t}\sum_{j=1}^{N_t}\Big\langle G_{i,t}\left(G_{i,t}+R_j\right)\Big\rangle - \langle G_t\rangle^2 \\
=& \frac{1}{N}\sum_{i=1}^{N}\frac{1}{N_t}\sum_{j=1}^{N_t}\Big[\langle G_{i,t}G_{i,t}\rangle + \langle G_{i,t}\rangle\langle R_j\rangle\Big] - \langle G_t\rangle^2 \\
=& \frac{1}{NN_t}\sum_{i=1}^{N}\langle G_{i,t}G_{i,t}\rangle + \frac{1}{NN_t}\sum_{i=1}^{N}\langle G_{i,t}\rangle(N_t-1)\langle G_t\rangle - \langle G_t\rangle^2 \\
=& \frac{1}{N_t}\Big[\langle G_t^2\rangle - \langle G_t\rangle^2\Big].
\end{aligned} \tag{3.24}$$

This result allows us to express the numerator of the spatial elastic autocorrelation function in terms of the elastic contribution stemming from bonds with the t-shell. The normalisation factor in the denominator of the autocorrelation function $C(r_t)$ can be evaluated in an analogous way, i.e.

$$\begin{aligned}
\langle G^2\rangle - \langle G\rangle^2 =& \left\langle\left(\sum_{s=1}^{S} G_s\right)\right\rangle^2 - \left\langle\sum_{s=1}^{S} G_s\right\rangle^2 \\
=& \left\langle\sum_{s=1}^{S} G_s^2 + \sum_{\substack{s,s' \\ s\neg s'}} G_sG_{s'}\right\rangle - \left(\sum_{s=1}^{S}\langle G_s\rangle^2 + \sum_{\substack{s,s' \\ s\neq s'}}\langle G_s\rangle\langle G_{s'}\rangle\right) \\
=& \sum_{s=1}^{S}\Big[\langle G_s^2\rangle - \langle G_s\rangle^2\Big].
\end{aligned} \tag{3.25}$$

Combining these two results we can express the spatial elastic autocorrelation in terms of the interaction shells as

$$C(r_t) = \frac{1}{N_t} \frac{\langle G_t^2 \rangle - \langle G_t \rangle^2}{\sum_{s=1}^{S} \left[\langle G_s^2 \rangle - \langle G_s \rangle^2 \right]}. \tag{3.26}$$

At this point, Eq. (3.26) still explicitly contains the angular structure of the spatial correlation by virtue of the angle dependence of the unit bond vector $\hat{\boldsymbol{n}}_{ij}$, which constitute the affine moduli. Since at this point we are only interested in the radial part of the autocorrelation function, we explicitly average over the angular distribution. This can be done by assuming an isotropic distribution of bonds which is formally correct only in the limit of large r_t. The full expression of the average contribution from the shell at distance r_t with bonds of stiffness κ_t is

$$\langle G_t \rangle = \left\langle \sum_{i=1}^{N_t} \frac{\kappa_t}{2} \left(r_t \hat{n}_{t,i}^x \hat{n}_{t,i}^y \right)^2 \right\rangle = N_t \frac{\kappa_t r_t^2}{2} \left\langle \left(\hat{n}_{t,i}^x \hat{n}_{t,i}^y \right)^2 \right\rangle \tag{3.27}$$

assuming that on average each of the N_t members on the t-shell has the same contribution. The bond length r_t and the stiffness $\kappa_t = \kappa(r_t)$ in the isotropic lattice do not depend on the angular distribution and hence are not affected by the angular average. Working with the isotropic assumption we uniformly distribute the bonds of the N_t neighbours in the t-shell over the full angle by specifying them in terms of the angular bond density $\rho(\varphi) = N_t f(\varphi) = N_t/(2\pi)$. Writing the unit bond vector in two-dimensional polar coordinates $(n_t^x, n_t^y) = (\cos\varphi, \sin\varphi)$ we express $\langle G_t \rangle$ as

$$\begin{aligned}
\langle G_t \rangle =& N_t \frac{\kappa_t r_t^2}{2} \int_0^{2\pi} \frac{1}{2\pi} \left(n_t^x n_t^y \right)^2 \mathrm{d}\varphi \\
=& N_t \frac{\kappa_t r_t^2}{2} \int_0^{2\pi} \frac{1}{2\pi} \Big(\sin(\varphi)\cos(\varphi) \Big)^2 \mathrm{d}\varphi \\
=& N_t \frac{\kappa_t r_t^2}{2} \int_0^{2\pi} \frac{1}{8\pi} \sin(2\varphi)^2 \, \mathrm{d}\varphi \\
=& N_t \frac{\kappa_t r_t^2}{16}.
\end{aligned} \tag{3.28}$$

In addition to the average $\langle G_t \rangle$ of the affine elastic contribution from the t-shell we also need the second moment $\langle G_t^2 \rangle$ in order to express the angular average of the elastic

autocorrelation. The mean square $\langle G_t^2 \rangle$ is explicitly given by

$$\langle G_t^2 \rangle = \left\langle \left(\sum_{i=1}^{N_t} \frac{\kappa_t}{2} \left(r_{t,i} \hat{n}_t^x \hat{n}_{t,i}^y \right)^2 \right)^2 \right\rangle = \frac{\kappa_t^2 r_t^4}{4} \left\langle \left(\sum_{i=1}^{N_t} \left(\hat{n}_{t,i}^x \hat{n}_{t,i}^y \right)^2 \right)^2 \right\rangle \tag{3.29}$$

which we can further evaluate by arranging the square of the sum into diagonal and off-diagonal contributions as

$$\sum_{i=1}^{N_t} \left(\hat{n}_{t,i}^x \hat{n}_{t,i}^y \right)^2 \sum_{j=1}^{N_t} \left(\hat{n}_{t,j}^x \hat{n}_{t,j}^y \right)^2 = \sum_{i=1}^{N_t} \left(\hat{n}_{t,i}^x \hat{n}_{t,i}^y \right)^4 + \sum_{\substack{i,j=1 \\ i \neq j}}^{N_t} \left(\hat{n}_{t,i}^x \hat{n}_{t,i}^y \hat{n}_{t,j}^x \hat{n}_{t,j}^y \right)^2 . \tag{3.30}$$

We now plug this expression into Eq. (3.29) and explicitly carry out the angular average and find that

$$\begin{aligned} \langle G_t^2 \rangle =& \frac{\kappa_t^2 r_t^4}{4} \left\langle \sum_{i=1}^{N_t} \left(\hat{n}_{t,i}^x \hat{n}_{t,i}^y \right)^4 + \sum_{\substack{i,j=1 \\ i \neq j}}^{N_t} \left(\hat{n}_{t,i}^x \hat{n}_{t,i}^y \hat{n}_{t,j}^x \hat{n}_{t,j}^y \right)^2 . \right\rangle \\ =& N_t \frac{\kappa_t^2 r_t^4}{4} \left[\left\langle (\hat{n}_t^x \hat{n}_t^y)^4 \right\rangle + (N_t - 1) \left\langle (\hat{n}_t^x \hat{n}_t^y)^2 \right\rangle^2 \right] \end{aligned} \tag{3.31}$$

where the unit bond vectors $\hat{\boldsymbol{n}}_t$ are distributed according to $f(\varphi) = 1/(2\pi)$. We have again resorted to the result that on average contributions from distinct bonds decorrelate in order to simplify the second term on the right-hand side. In order to compute the average of the first term we note that using polar coordinates it can be expressed as $(\hat{n}_t^x \hat{n}_t^y)^4 = (\sin\varphi \cos\varphi)^4 = \frac{1}{16} \sin^4(2\varphi)$. Bearing this in mind we continue by expressing the corresponding angular average in the continuum approximation as

$$\left\langle (\hat{n}_t^x \hat{n}_t^y)^4 \right\rangle = \int_0^{2\pi} \frac{1}{2\pi} \frac{1}{16} \sin^4(2\varphi) \, \mathrm{d}\varphi = \frac{3}{128}. \tag{3.32}$$

The result of the angular average appearing in the second term on the right-hand side of Eq. (3.31) is already known from the previous analysis to yield $(\langle \hat{n}_t^x \hat{n}_t^y)^2 \rangle = 1/8$. Combining these findings we can express the second moment $\langle G_t^2 \rangle$ as

$$\langle G_t^2 \rangle = N_t \frac{\kappa_t^2 r_t^4}{4} \left[\frac{3}{128} + (N_t - 1) \frac{1}{64} \right] = N_t \frac{\kappa_t^2 r_t^4}{4} \frac{2N_t + 1}{128}. \tag{3.33}$$

This now allows to to write the final result for numerator the angular average of the spatial elastic autocorrelation function $C(r_t)$ as

$$\begin{aligned}\langle G_t^2\rangle - \langle G_t\rangle^2 =& N_t \frac{\kappa_t^2 r_t^4}{4}\frac{2N_t+1}{128} - \left(N_t\frac{\kappa_t r_t^2}{16}\right)^2 \\ =& N_t \frac{\kappa_t^2 r_t^4}{4}\left[\frac{2N_t}{128}+\frac{1}{128}-\frac{N_t}{64}\right] \\ =& N_t \frac{\kappa_t^2 r_t^4}{512}.\end{aligned} \tag{3.34}$$

We recall that the denominator of $C(r_t)$ involves the summation of Eq. (3.34) over all interaction shells in the system up to the cutoff S. This means that the denominator yields a prefactor to the full expression of $C(r_t)$ which does not depend on the argument r_t. Put in other words, this means that the radial scaling of $C(r_t)$ is solely dictated by the numerator as given in the final expression of Eq. (3.34) and we can express the scaling as

$$C(r_t) \sim \frac{1}{N_t}\left[\langle G_t^2\rangle - \langle G_t\rangle^2\right] = \frac{\kappa_t^2 r_t^4}{512}. \tag{3.35}$$

Having this result at hand, we can now implement an assumption of the decay of the r-dependent stiffness κ_t. In particular, if we introduce an inverse power-law decay of the stiffness, i.e. $\kappa_t \sim r_t^\alpha$, we draw the conclusion that the radial decay of the affine elastic autocorrelation function has to obey the scaling

$$C(r) \sim r^{4-2\alpha}. \tag{3.36}$$

where we dropped the explicit shell label. We conclude from this results that choosing the exponent of the power-law decay of the interaction strength $\kappa_r \sim r^\alpha$ as $\alpha = 3$ we obtain a radial elastic correlation as $C(r) \sim r^{-2}$.

3.6 Numerical results of the elastic autocorrelation function

As pointed out in the introduction of this chapter, in many disorder condensed matter systems like Lennard-Jones glasses and lattices with thermally induced non-affinity have been observed to exhibit power-law correlation in the elastic autocorrelation characteristics. In the perfect lattice, where every bond is occupied and thus $p = 1$, we do

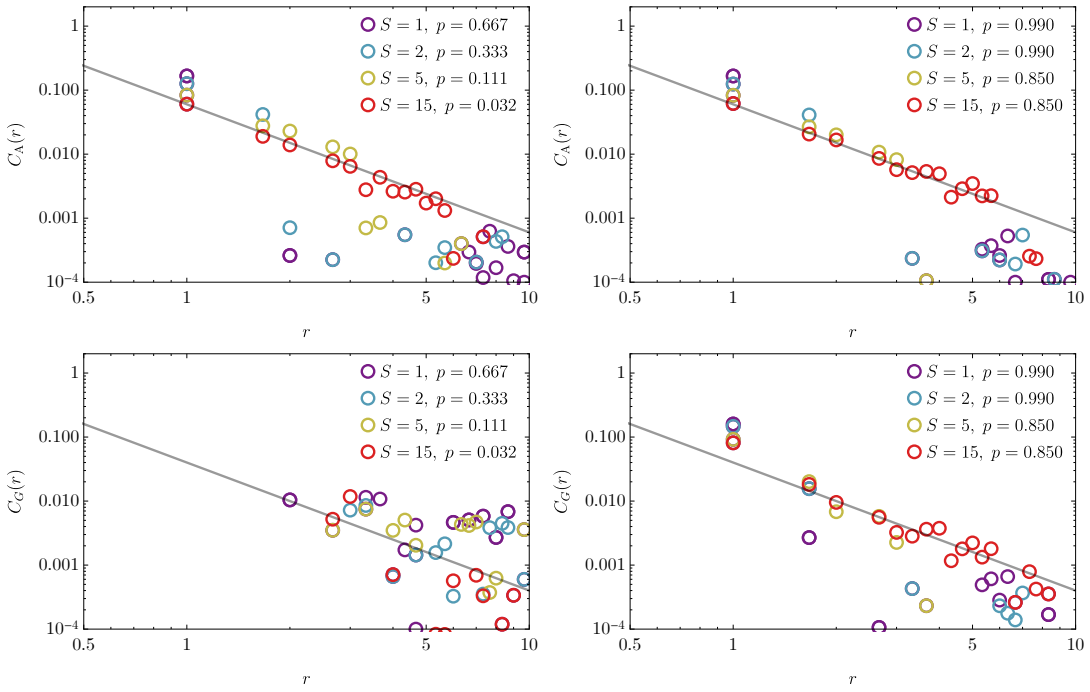

Fig. 3.6 Angular average of the elastic autocorrelation function. The first row shows the affine autocorrelation C_A both at the respective critical points for each interaction shell in the left panel, and at the high bond-occupation probabilities in the right panel. The second row shows the angular average of the full elastic autocorrelation C_G. The continuous line describes the r^{-2} scaling.

not expect the appearance of power-law correlations by virtue of the simple fact that the value of each $G_{A,i}$ is equal for all sites and the non-affine contribution is exactly zero. In order to account for the realistic scaling of the elastic autocorrelation function observed in MD simulations, which in two dimensions is $C(r) \sim r^{-2}$ [17], we choose the decay of the stiffness $\kappa(r)$ in our model as r^{-3}, as we have hinted before. Considering the scaling result in Eq. (3.36), this choice results in the desired scaling of the affine elastic autocorrelation function and provide the link to the results obtained for various disordered solids and glasses in the literature, as discussed in the introduction of this chapter.

Having the analytical scaling relation affine elastic autocorrelation at hand it is now time to compare the analytical against numerical results. For this purpose, we have numerically computed the angular average of the affine and full elastic autocorrelations function as shown in Fig. 3.6. We have chosen to depict the high p and critical p_c regimes for the four interaction ranges in question. As can be seen clearly in this double-logarithmic plot, both at the respective critical bond-occupation probabilities and at high values of p, the numerical data for the four different interaction ranges follows the

analytical scaling relation. As we can expect, the range of the power-law correlations depends on the interaction range. The numerical data for the $S = 1$ autocorrelation rapidly drops after $r = 1$, which signifies the radius of the nearest-neighbour interaction shell. With increasing S, this drop of the correlation function moves to higher values, as can be seen in Fig. 3.6. For example, we clearly can observe how $C_A(r)$ drops to very low values at a radial distance that corresponds to the radius of the $S = 15$ interaction shell, $r_{15} = 6$. Considering the radial scaling of the full elastic autocorrelation function $C_G(r)$ in the bottom row of Fig. 3.6, it becomes evident that at high p the r^{-2} still is maintained to a good agreement. The deviations come from the additional non-affine contribution. And as we see in the left panel of the bottom row, the power-law correlations disappear when the isostatic point is reached, and the non-affine fluctuations in the local moduli take over.

In conclusion, in the regime of high p, the angular average of the full elastic autocorrelation function $C_G(r)$ inherits the r^{-2} scaling of the its affine counterpart and the non-affinity induced deviations appear to be relatively small.

3.7 Effect of the non-affine contribution

Having described the scaling behaviour of the affine elastic autocorrelation, we established that the affine scaling approximately carries over to the scaling of the full shear modulus $G = G_{\mathrm{A}} - G_{\mathrm{NA}}$ if the bond disorder in the lattice is not too large. This raises the interesting question how the correlations of the full shear modulus with its two contributions G_{A} and G_{NA} develops when the bond-occupation in the system decreases further. The addition of disorder into the lattice locally breaks the inversion symmetry and leads to an increase non-affine correction to the shear elasticity, which leads us to expect that the non-affine contribution to the correlation should increase.

In order to obtain insights into the interplay between the affine and non-affine contribution we evaluated the Pearson correlation coefficients between the full shear modulus G and its affine and non-affine parts. The correlation coefficient between two random variable f and g is defined as defined as [84]

$$\rho_{X,Y} = \frac{\mathrm{cov}(XY)}{\sqrt{\mathrm{var}(X)\mathrm{var}(Y)}} \tag{3.37}$$

where $\mathrm{cov}(X,Y) = \langle XY\rangle - \langle X\rangle\langle Y\rangle$ and $\mathrm{var}(X) = \langle X^2\rangle - \langle X\rangle^2$ denote the covariance and variance of the random variables X and Y, respectively. Therefore, the correlation coefficient ρ_{XY} represents the covariance between the two random variables normalised

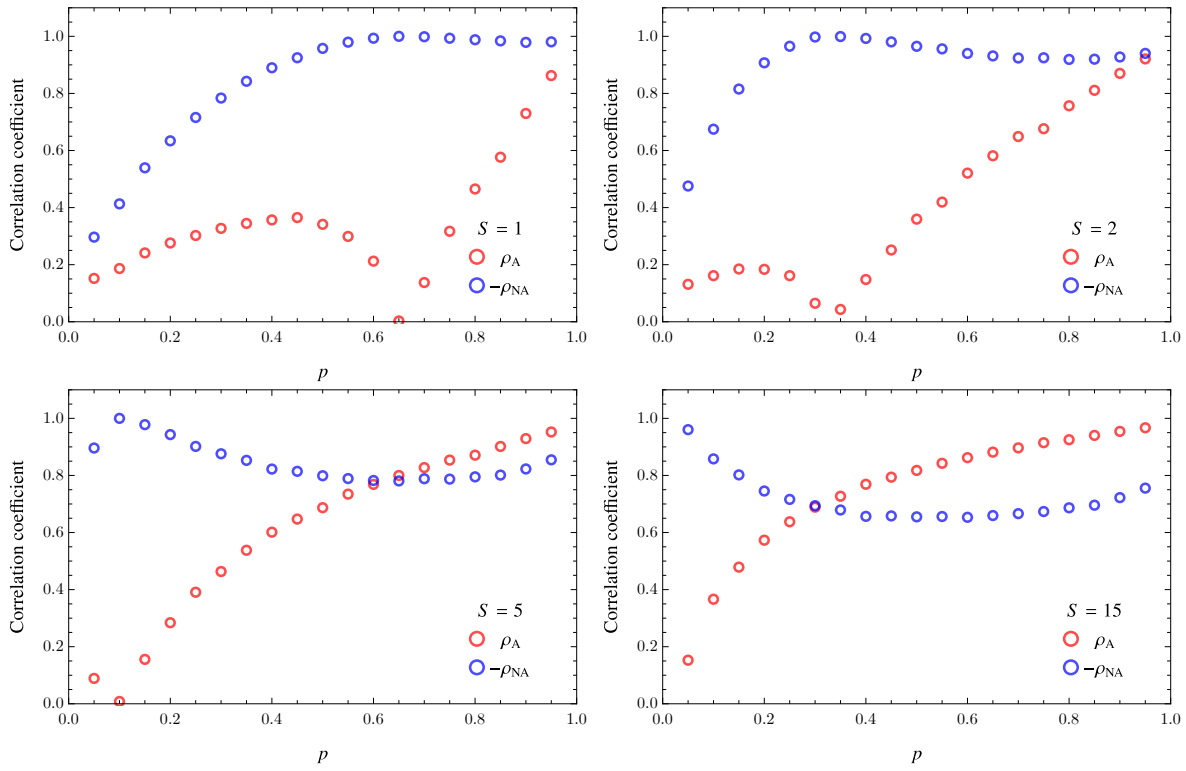

Fig. 3.7 The correlation coefficients for G and G_{A}, and G and G_{NA} for four different interaction ranges and $\kappa \propto r^{-3}$. Starting at $S = 5$, a crossover between the affine and non-affine regime can be clearly observed. Since the sign of the non-affine contribution is negative, the absolute value of the correlation coefficient between G and G_{NA}.

with the square root of the variance of each variable f and g. The squared coefficient ρ_{XY}^2 takes values in the interval $[0, 1]$, indicating the degree to which the two random variables are statistically correlated. A positive value of ρ_{XY} signifies positive correlation between X and Y, a negative sign means anti-correlation. The Pearson correlation coefficient is in principle the same object as the correlation function introduced earlier with the difference that the averages in numerator are evaluated over the full system and not restricted to a specific shell.

In Fig. 3.7 we present the results for the computation of the correlation coefficients between both the affine and non-affine contribution and the full shear modulus, respectively, for which we use the notation $\rho_{\mathrm{A}} = \rho_{GG_{\mathrm{A}}}$ and $\rho_{\mathrm{NA}} = \rho_{GG_{\mathrm{NA}}}$. Note that the non-affine correlation coefficient is plotted with a negative sign, since naturally G is expected to anticorrelate with G_{NA}.

We first want to explain the situation in the nearest-neighbour case $S = 1$. We observe that at a high bond-occupation probability, i.e. p close to 1, the value of the affine correlation coefficient ρ_{A} has its maximum. This corresponds to the situation of a

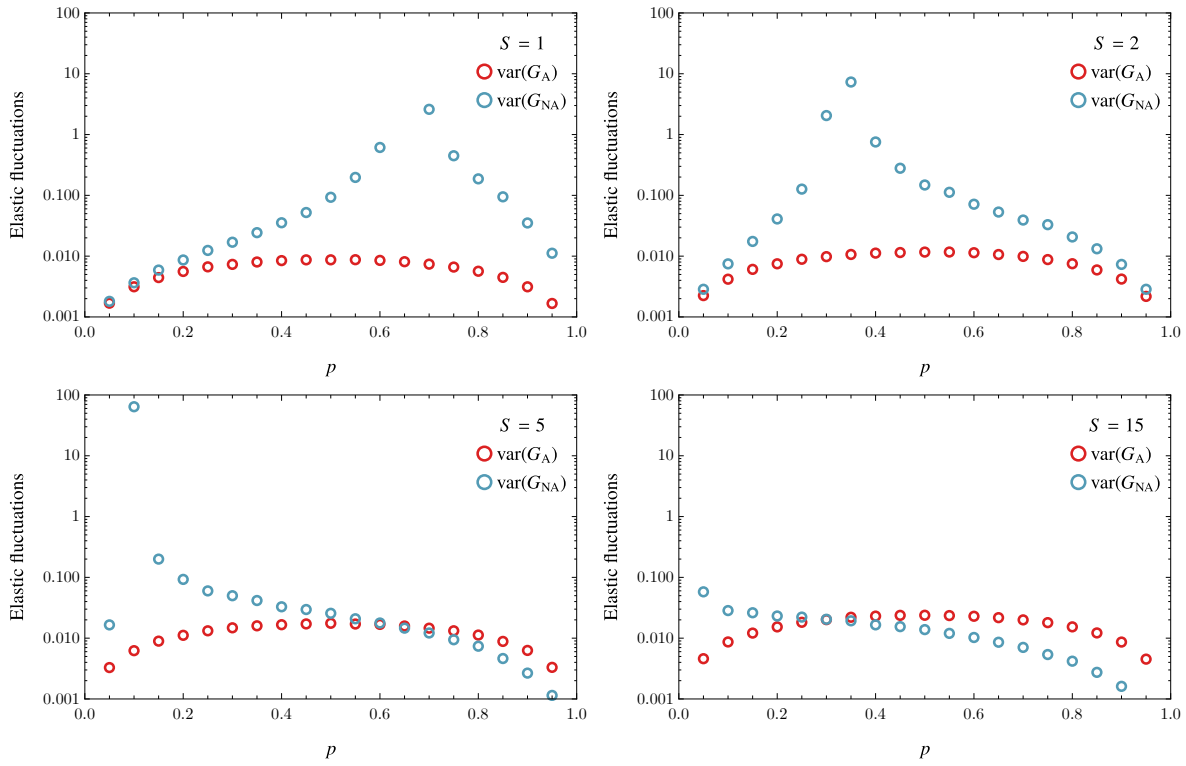

Fig. 3.8 The variance of the affine and non-affine local moduli for different interaction ranges S. Moving from $S = 1$ to $S = 15$, a crossover occurs as $\mathrm{var}(G_{\mathrm{NA}})$ is partly pushed below $\mathrm{var}(G_{\mathrm{A}})$.

lattice where most of the bonds are present, and consequentially the degree of non-affinity is relatively low. This makes the high value of ρ_{NA} seem out of place. However, we have to bear in mind that in the $S = 1$ lattice the distribution the local moduli is strongly discretised. At the full coordination number $Z_1 = 6$, the distribution of the local moduli is determined by the one δ-peak in the distribution of $G_{\mathrm{A},i}$. Reducing p to 0.95, the shape of the G_i distribution maintains this δ-like peak as the dominant contribution, accompanied by one smaller δ-like peak at lower value, which are exclusively due to the discretised $G_{\mathrm{A},i}$-distribution. In addition, the full distribution of the local moduli G_i develops a continuous component, as can be seen in Fig. 3.3. The shape of the continuous part is controlled by the distribution of the local non-affine moduli $G_{\mathrm{NA},i}$. Therefore, in the $S = 1$ case at p close to 1, both the affine and non-affine correlation coefficient, ρ_{A} and ρ_{NA} exhibit high values which trace back to the fact that the affine and non-affine distributions separately control the discrete and continuous part of the full distribution.

At the isostatic point of the nearest-neighbour triangular lattice, which is located at $p_c = 2/3$, where the lattice loses its mechanical stability, the correlation between the affine and full modulus breaks down. The vanishing of the correlation coefficient ρ_{A} is

due to the divergence of the fluctuations of the non-affine shear modulus at the critical point [14]. This behaviour of the fluctuations of the affine modulus becomes evident from the right panel in Fig. 3.4. Since the variance of the non-affine modulus appears in the denominator of the correlation coefficient in Eq. (3.37), the affine correlation coefficient is being suppressed at p_c. Naturally, this does not occur in the case of the non-affine correlation coefficient because there the fluctuations in the denominator and numerator are of the same order.

When the maximal interaction range of the lattice is increased, we can see that the position where the affine correlation coefficient ρ_{A} drops to zero moves to lower values in p, in accordance with the decreasing of the critical bond-occupation probability p_c when increasing S. Again this scaling behaviour is mirrored by the movement of the position where $\mathrm{var}(G_{\mathrm{NA}})$ diverges as we see in the right panel of Fig. 3.4.

The most prominent feature of the correlation coefficients depicted in Fig. 3.7 is the appearance of a crossover between the affine and non-affine correlation coefficient, ρ_{A} and ρ_{NA}, when S is increased. Introducing long-range bonds therefore leads to the emergence of two regimes where either the affine or non-affine correlations dominate. This crossover can be seen to appear in the $S = 5$ lattice at $p \approx 0.6$, and in the $S = 15$ lattice at $p \approx 0.3$.

We will now explain the appearance of the affine/non-affine crossover in terms of the fluctuation characteristics of the affine and non-affine local moduli. The general effect of increasing S is to increase the fluctuations of the local affine moduli over the entire range of the bond probability p, as evident from in Fig. 3.4 (a). The reason for this amplification clearly is the fact that at a given p, in number of bonds present in the lattice rapidly grows when long-range bonds are included. Having more possible values for the local coordination numbers means in turn that also $G_{\mathrm{A},i}$, which directly reflects the local coordination geometry, can take many more possible values.

The effect of the enhanced fluctuations of the affine local moduli distributions translates directly to the correlation coefficients. As S grows, the critical p_c gets pushed to lower values and the affine correlation function on the interval $[0, 1]$ is amplified. At the same time, due to the inclusion of the long-range bonds, the fluctuations of the non-affine local moduli experience an attenuation. These two counteracting effects can be clearly observed in Fig. 3.8. Where for $S = 1$ and $S = 1$ the non-affine elastic fluctuations, characterised by $\mathrm{var}(G_{\mathrm{NA}})$, are larger than the affine fluctuations on the full interval $p \in [0, 1]$, this ceases to be the case for the longer-range lattices $S = 5$ and $S = 15$. As the divergence of $\mathrm{var}(G_{\mathrm{NA}})$ is shifted to lower values of p, the larger number of connected neighbours constrains and reduces $\mathrm{var}(G_{\mathrm{NA}})$ below $\mathrm{var}(G_{\mathrm{A}})$ in the high p

regime. Therefore, we can infer that the affine/non-affine crossover manifested in the correlation coefficient is rooted in the counteracting trends of the affine and non-affine fluctuations that arises through the implementation of long-range interactions.

3.8 Spatial correlation structure

Having worked out a good understanding the radial dependence of the elastic autocorrelation function and the affine/non-affine crossover, we now set out to describe the spatial correlation characteristics in more detail. In particular, we will investigate how the crossover of the correlation coefficient between the affine and the non-affine regimes is reflected in the spatial structure of the autocorrelation functions C_G, G_{A} and C_{NA}.

To grasp the correlation structure across the regime crossover, as well as at the isostatic point, we will map out the functions C_G, G_{A} and C_{NA} at three representative values of the bond-occupation probability p. For $S = 1$, 2, 5 and 15 we specify a high and intermediate p regime, such that the different systems are well in the affine and non-affine-dominated parts, if the crossover exists, in view of the correlation coefficient in Fig. 3.7.

In addition, as a third value of the bond-occupation probability p, we will map out the correlation structure for each interaction range at the respective isostatic points. To achieve a good visual representation of the spatial autocorrelation functions, we mapped out separately the affine, non-affine and full shear modulus autocorrelations by projecting the contribution from each individual site onto a central site, thereby creating the density plots presented in this section. As the plot legends show, in all correlation maps in this chapter, blue signifies no correlation, and the tendency to red and black shows positive and negative correlation in respectively.

Before starting the detailed discussion of the spatial correlation structure and how it evolves with the interaction range in the lattice, we point out the three principal patterns that we will encounter in the following analysis. Firstly, the affine autocorrelation function generally exhibits the typical positive correlation along the diagonals of the lattice. As we can anticipate from the preceding analysis, the length of these positive correlation lobes increases with the range of the interaction as given by the maximal shell size S. In addition to that, we conclude from the numerical analysis that the geometrical structure of the affine autocorrelation function C_{A} is practically not affected by the bond-depletion parameter p. This aligns with the analytical prediction for the scaling of C_{A}, which we found not to explicitly depend on p. An example of this behaviour of the affine elastic

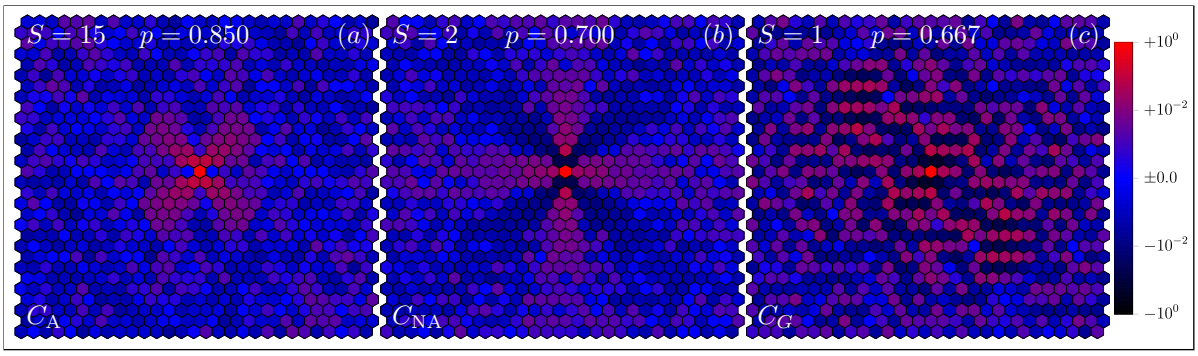

Fig. 3.9 The three main patterns of the elastic autocorrelation functions as explained in the text. From left to right depicted: pattern of C_A with positive correlation along the diagonals, pattern of C_{NA} with negative correlation along the diagonals and positive correlation along x and y axes, highly fluctuating pattern of C_G at the isostatic point.

autocorrelation is depicted in Fig. 3.9 (a) for the system $S = 15$ with $p = 0.850$. Note that the plots do not show the full system butt merely a 30×30 sector.

The second recurring pattern is that typical of the non-affine autocorrelation function C_{NA}. The lobes of C_{NA} tend to be aligned with with both the x and y-axes of the lattice. Along the diagonal, C_{NA} exhibits anti-correlation as shown in Fig. 3.9 (b). In contrast to the affine autocorrelation function, the range of these lobes decreases with increasing the interaction range S. The third distinct correlation pattern we observe, appears in the case when neither the affine nor the non-affine lobe patters appear clearly. This occurs to a varying degree when the lattice reaches the isostatic point at the bond-occupation probability $p = p_c$, where moduli correlations are seen to fluctuate strongly over a large region of the lattice, compared to the non-critical correlations. The degree to which these fluctuations of the elastic autocorrelation permeate the system depends on the interaction range. The instance of the nearest-neighbour lattice $S = 1$ at the isostatic point $p = 2/3$ is depicted in Fig. 3.9 (c).

We will start the analysis of the spatial correlation structure with the case of the high-p regimes for all four interaction ranges. As we have already observed in Fig. 3.7, we expect the crossover between the affine and non-affine regime to takes place here.

3.8.1 Correlation structure at high p

The behaviour of the three autocorrelation functions C_A, C_{NA} and C_G in the high-p regime is summarised in Fig. 3.10.

The first row shows the change the affine autocorrelation undergoes when increasing the maximal interaction range S. Starting with the nearest-neighbour case, as expected,

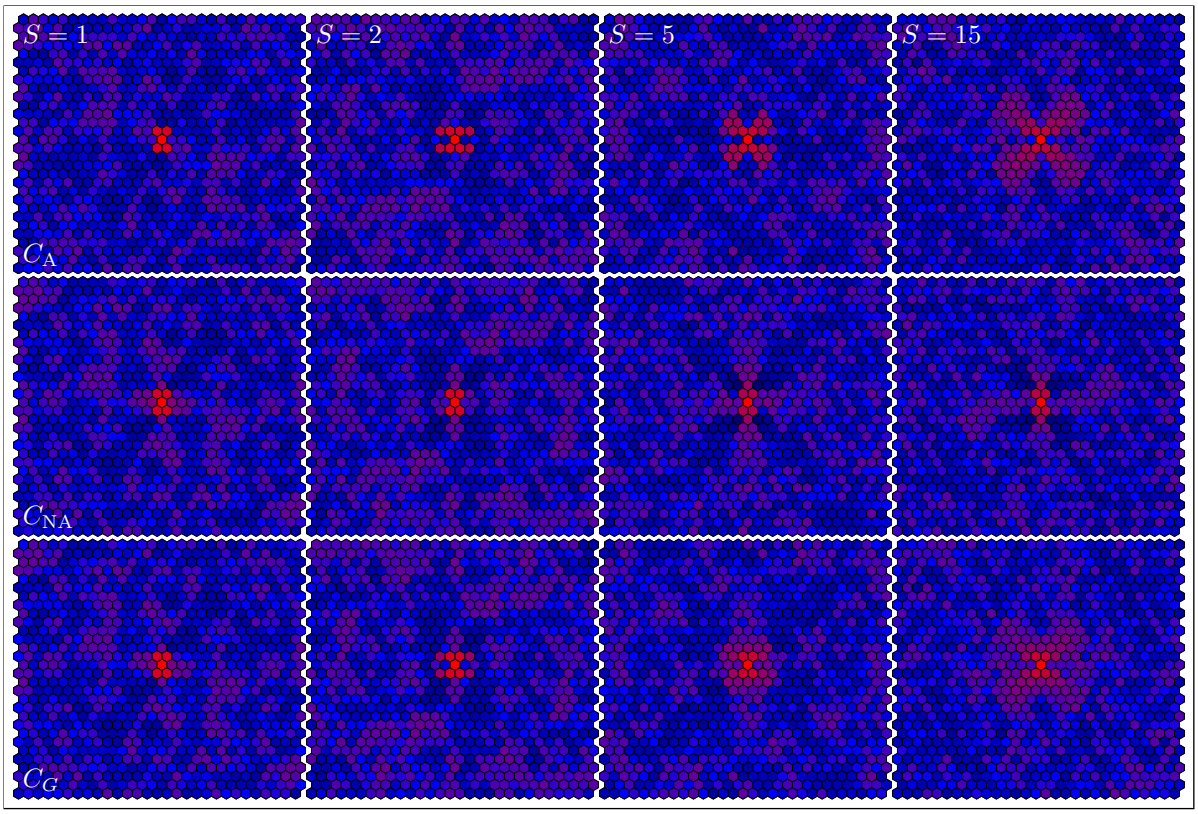

Fig. 3.10 The spatial autocorrelation structure for the high bond-occupation probabilities $p = 0.990$ for $S = 1, 2$ and $p = 0.850$ for $S = 5, 15$. The affine, non-affine and full elastic autocorrelations are shown separately for all interaction ranges under investigation.

C_{A} exhibits significant positive correlation only with the four neighbours which contribute to the mechanical stability under the x-y shear in the first shell. The same pattern continues to the $S = 2$ case, where the affine autocorrelation has a positive contribution at four additional lattice sites, which are the four mechanically stable bonds added into the second shell. Further increasing the maximal interaction range to $S = 5$ and $S = 15$ we observe that the range of the affine correlation function increases proportional to the shell range in correspondence to the behaviour described above in terms of the angular average of C_{A}.

In the second row of Fig. 3.10 we find evidence for the emergence of the two main characteristic of the non-affine autocorrelation function. Firstly, as mentioned above, the non-affine autocorrelation function exhibits positive correlation lobes along the x and y-axes in physical space. The trend of the range of the positive non-affine correlation lobes clearly is seen to increase with the interaction range cutoff S.

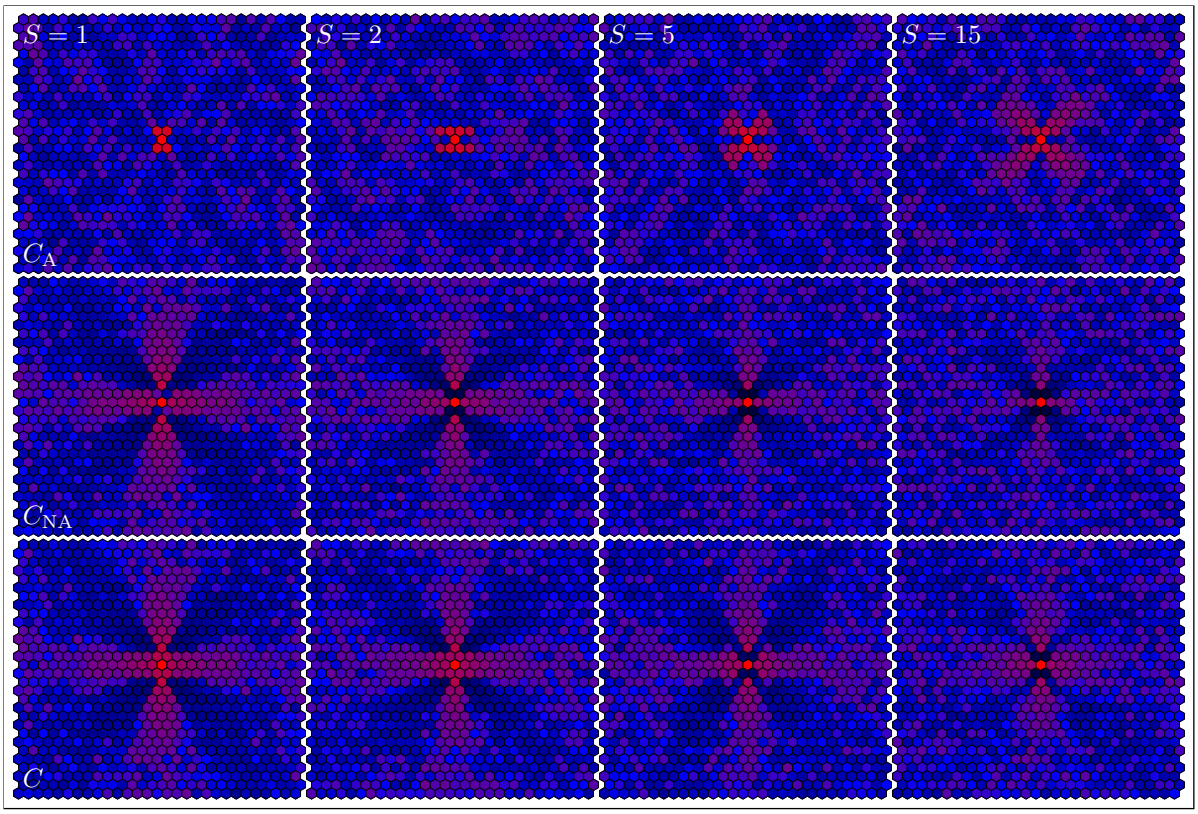

Fig. 3.11 The spatial autocorrelation structure for the intermediate bond-occupation probabilities $p = 0.850$ for $S = 1$, $p = 0.700$ for $S = 2$, $p = 0.400$ for $S = 5$, and $p = 0.200$ for $S = 15$. The affine, non-affine and full elastic autocorrelations are shown separately for all interaction ranges under investigation.

The spatial autocorrelation structure of the full shear modulus C_G. Recalling the results on the behaviour the affine and non-affine correlation coefficients, it is possible to observe interplay between the relative strengths of ρ_{A} and ρ_{NA} in the spatial correlation patterns. For the $S = 1$ case with a fraction of $p = 0.990$ bonds present, both correlation coefficients are close to one. And in fact, we can verify that the corresponding C_G is a mixture of both C_{A} and C_{NA}. This pattern of the autocorrelation function C_G is even clearer in the $S = 2$ lattice with $p = 0.990$. The situation is very different in the longer-range lattices with interaction cutoff $S = 5$ and $S = 15$ both at $p = 0.850$. Even though the non-affine autocorrelation appears longer ranged both in the positive and negative correlation lobes, we can in this instance observe the crossover to the affine regime predicted earlier. The $S = 15$ elastic autocorrelation function C_G clearly predominantly inherits the affine diagonal lobes of C_{A}. This trend decreases going to lower S, as we would expect. The $S = 5$ and $S = 15$ full elastic autocorrelations exhibit predominantly

affine characteristics, where the $S = 1$ and $S = 2$ cases have clear contributions from the non-affine positive and negative correlation lobes.

3.8.2 Correlation structure at intermediate p

Consider the autocorrelation function maps at the intermediate choices for the bond probability p the situation is different. The choices for the intermediate bond-occupation probabilities are such that all four lattices are in the in the regime where the non-affine correlation coefficient dominates. This readily translates to the C_G correlation maps of plotted in the third row of Fig. 3.11. We can clearly see that all four predominantly controlled by the non-affine autocorrelations.

It is noteworthy, that in contrast to the high p situation, the non-affine autocorrelation function C_{NA} exhibits stronger anticorrelations for all interaction ranges than in the high-p regime. In particular, we can observe in Fig. 3.11 that the range of these anti-correlations increases when going from $S = 15$ to $S = 1$. The particular choice of the bond-occupation probabilities for the S has the consequence that the relative strength of the affine correlation coefficient ρ_{A} with respect to the non-affine correlation coefficient ρ_{NA} for $S = 1$ and $S = 2$ is significantly higher than for $S = 5$ and $S = 15$, as seen in Fig. 3.7. This is reflected in the spatial correlation patterns C where for $S = 1$, 2 the short-range positive correlation is present at the distance of the first and second shell, respectively. This positive correlation ring is followed by the anticorrelations along the diagonals which is characteristic for C_{NA}. This behaviour cannot be observed for $S = 5$, 15 where at $p = 0.850$ the relative strength of ρ_{A} is too low, despite the fact that the correlation length of C_{A} is increasingly larger than for $S = 1$, 2.

3.8.3 Correlation structure at the critical point p_c

Firstly, as expected from the aforementioned analytical result for C_{A}, we can observe in Fig. 3.12 that also at the respective critical bond-occupation probabilities the affine autocorrelations practically exhibits the exact same form as for high and intermediate p. In addition to that we also anticipate from the fact that the non-affine fluctuations var(G_{NA} show a divergence at the critical p_c that the full elastic autocorrelation function should be dominated by contributions from the non-affine part C_{NA}. In fact this is the behaviour we see in the spatial plots of C, C_{A} and C_{NA} shown in Fig. 3.12. The full elastic autocorrelation feature the long-range, highly fluctuating patterns mentioned above. The nearest-neighbour lattice has the longest-range and strongest elastic autocorrelation pattern of the four interaction ranges. We notice that the correlation pattern is oscillatory

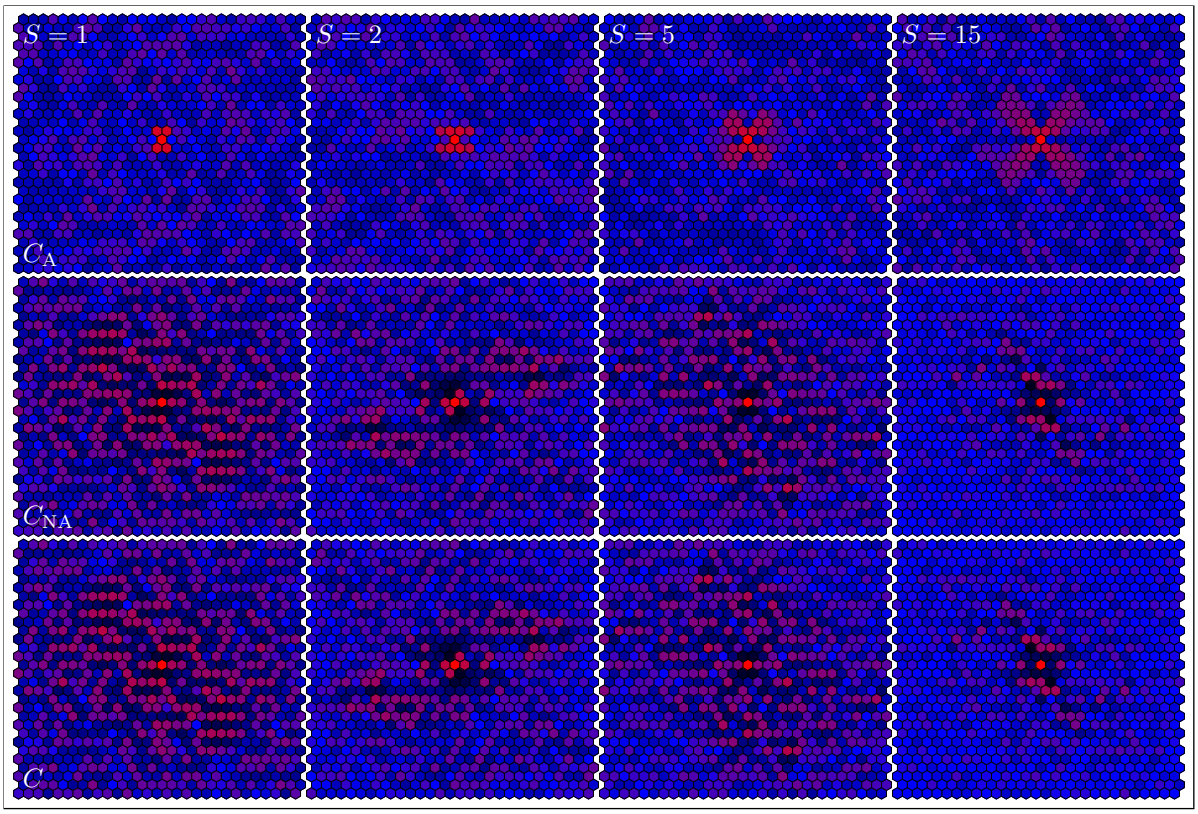

Fig. 3.12 The spatial autocorrelation structure for the critical bond-occupation probabilities $p = 0.667$ for $S = 1$, $p = 0.333$ for $S = 2$, $p = 0.111$ for $S = 5$, and $p = 0.032$ for $S = 15$. The affine, non-affine and full elastic autocorrelations are shown separately for all interaction ranges under investigation.

changing between positive and negative correlation. These kind of oscillations have been observed for example in Ref. [38]. The range of the critical elastic correlations reduces as the interaction range increases. We can observe an anomalous change in the shape at $S = 2$, since $S = 1$ and $S = 5$ bear more resemblance in their correlation with each other than with $S = 2$. The cause for this is not know at this point. The attenuation of the critical fluctuations as seen in Fig. 3.12 can be explained again by the fact that the non-affine fluctuations $\mathrm{var}(G_{\mathrm{NA}})$ get damped in amplitude by the inclusion of more bonds.

3.8.4 The mechanisms controlling the elastic autocorrelation

We first want to explain the quadrupolar angular pattern we have observed for the affine autocorrelation function C_{A}. Going back to the definition of the local affine modulus in Eq. (3.6), we see that the contribution to the angular dependence of the affine modulus

from the bond between site i and j is proportional to $\left(n_{ij}^x n_{ij}^y\right)^2 = \sin^2(\varphi_{ij})$ by writing the unit bond vector in polar coordinates. The characteristic angular pattern of the affine elastic correlation function threfore stems from the fact that a typical contribution of has the form

$$C_{\mathrm{A}} \sim \left(n_{ij}^x n_{ij}^y\right)^4 \sim \sin^4(2\varphi_{ij}) \tag{3.38}$$

where φ_{ij} denotes the bond angle of the bond between particle i and j. The physical picture of the diagonal alignment of the positive correlation lobes is provided by the fact that the system is subject to a shear deformation. In the continuum picture of elasticity, applying an external shear strain to the solid leads to regions of elongation and compression (we can think of the simple analogy of a rubber band elongating and compression in different directions when stretched) along the diagonals of the system. The result of this is that the affine shear modulus becomes biased along the diagonal axes and therefore positively correlated. This precisely reflects the action of the deformation gradient tensor $\mathbf{F}$ for pure shear.

In contrast to the affine elastic autocorrelation function, C_{NA} cannot be simply written as a summation over the bonds in the lattice. Understanding the origin of the lobe structure of the C_{NA} and its evolution with changing parameters therefore is not as straightforward as with C_{A}.

We recall that the local non-affine modulus is defined in terms of the non-affine displacement fields and the affine force field as

$$G_{\mathrm{NA},i} = \frac{1}{V}\, \boldsymbol{\Xi}_i \cdot \delta \boldsymbol{r}_{\mathrm{NA},i}. \tag{3.39}$$

where the local non-affine displacement fields where defined in Eq. (3.8) as $\delta \boldsymbol{r}_{\mathrm{NA},i} = \langle \boldsymbol{i}|\, \boldsymbol{H}^{-1}|\boldsymbol{\Xi}\rangle = \sum_p \lambda_p^{-1} \langle \boldsymbol{i}\,|\boldsymbol{p}\rangle\langle \boldsymbol{p}|\,\boldsymbol{\Xi}\rangle$. For this reason, it should be possible to gain some understanding about the origin of the spatial patterns of the non-affine autocorrelation C_{NA} by studying the autocorrelations of the local affine force field $\boldsymbol{\Xi}_i$ and the local non-affine displacement fields $\delta \boldsymbol{r}_{\mathrm{NA},i}$. We first consider the affine force field correlations, since as in the case of C_{A} we expect from the definition of $\boldsymbol{\Xi}_i$ that the geometry of the bond configuration is responsible for the correlation structure. The local affine force field is defined as

$$\boldsymbol{\Xi}_i = \sum_j \kappa_{ij} r_{ij} n_{ij}^x n_{ij}^y \hat{\boldsymbol{n}}_{ij} \tag{3.40}$$

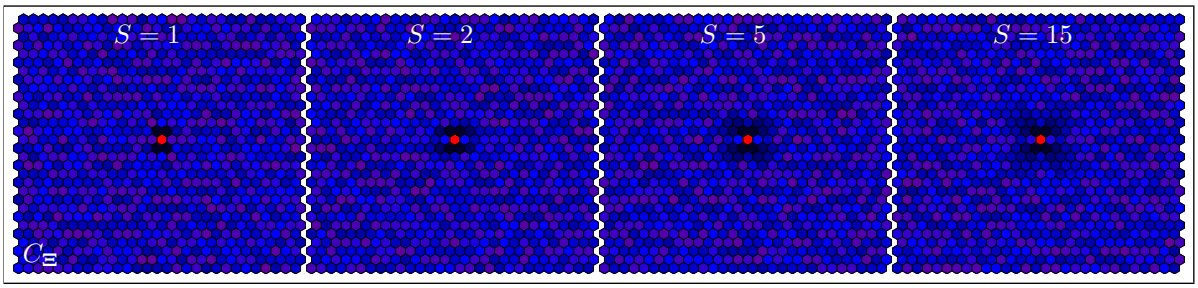

Fig. 3.13 The spatial patterns of the affine forcefield autocorrelation function $C_{\boldsymbol{\Xi}}$ depicted for the four interaction ranges $S = 1$, 2, 5, and 15 in their respective high p regimes.

where the summation over the index j is restricted to the sites connected to i with a bond of stiffness κ_{ij} and bond length r_{ij}. Consequently, we compute the associated autocorrelation function by projecting the local affine force field at site i onto that at site j. The resulting contribution to the autocorrelation function $C_{\boldsymbol{\Xi}}$ is given by

$$\Big[C_{\boldsymbol{\Xi}}(\boldsymbol{r})\Big]_{ij} = \frac{\langle \boldsymbol{\Xi}_i \cdot \boldsymbol{\Xi}_j \rangle - \langle \boldsymbol{\Xi}_i \rangle \langle \boldsymbol{\Xi}_j \rangle}{\langle \boldsymbol{\Xi}^2 \rangle - \langle \boldsymbol{\Xi} \rangle^2}. \tag{3.41}$$

Due to the fact that the affine force field is essentially an sum over bonds, its spatial correlation structure behaves similarly to the affine modulus correlation function, with the difference that instead of the diagonal positive correlation lobes we now find diagonal anti-correlation. We can see this behaviour in Fig. 3.13. The $S = 1$ affine force field correlations shows clear negative correlation with the four mechanically contributing neighbours, indicated by the black colour coding of the sites. The trend towards anti-correlations can be understood in the following way. Imagine that particle j is situated in the $S = 1$ shell of particle i. In the case, where all six bonds are present, the affine force field is zero locally. However, if the bond between site i and j is cut, Eq. (3.40) will yield a non-vanishing contribution. To be specific, assuming the ij-bond, which is cut, lies along the direction $(1/2, \sqrt{3}/2)$, the resulting affine force field at site i will point along the opposite direction, i.e. $\boldsymbol{\Xi}_i \propto (-1/2, -\sqrt{3}/2)$, as can easily be checked. Viewed from site j, of course, the cutting of the bond will yield an affine force field which point in the opposite direction. So effectively, $\boldsymbol{\Xi}_i \propto -\boldsymbol{\Xi}_j$, which is the reason for the tendency of negative correlations of the affine force field along the directions $(\pm 1/2, \pm\sqrt{3}/2)$. Moving to the higher interaction range cutoffs, more and more sites along their associated unit bond vector tend to anti-correlate with the affine force field at the central site, and as a consequence the range of the anti-correlation lobes in $C_{\boldsymbol{\Xi}}$ grows, which is evident from Fig. 3.13.

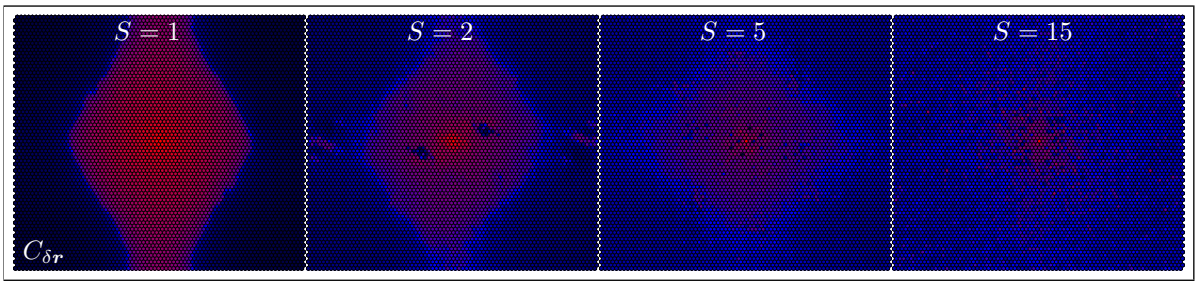

Fig. 3.14 The spatial structure of the non-affine displacement correlation function at the critical point for different interaction ranges.

Resorting to the representation of the unit bond vectors in polar coordinates we can express $\langle \boldsymbol{\Xi}_i \cdot \boldsymbol{\Xi}_j \rangle$, i.e. the term which appears as the covariance in the autocorrelation between site i and j, in terms of the bond angle φ_{ij}. Considering the configurational average of $\boldsymbol{\Xi}_i \cdot \boldsymbol{\Xi}_j$, only the bond between i and j directly contributes to the correlation. For this reason, by only retaining this contribution we write

$$\boldsymbol{\Xi}_i \cdot \boldsymbol{\Xi}_j \propto \sum_k n_{ik}^x n_{ik}^y \hat{\boldsymbol{n}}_{ik} \sum_l n_{jl}^x n_{jl}^y \hat{\boldsymbol{n}}_{jl} \sim n_{ij}^x n_{ij}^y n_{ji}^x n_{ji}^y \hat{\boldsymbol{n}}_{ij} \cdot \hat{\boldsymbol{n}}_{ji}. \tag{3.42}$$

Since $\hat{\boldsymbol{n}}_{ij} = -\hat{\boldsymbol{n}}_{ji}$ and $\hat{\boldsymbol{n}}_{ij} = (\cos\varphi_{ij}, \sin\varphi_{ij})$ in terms of the bond vector we obtain

$$\boldsymbol{\Xi}_i \cdot \boldsymbol{\Xi}_j \propto -\left(\sin\varphi_{ij}\right)\cos\varphi_{ij})\big)^2 = -\sin^2\left(\varphi_{ij}\right) \tag{3.43}$$

which describes the quadrupolar anticorrelation lobes seen in Fig. 3.13.

Alongside the affine force field $\boldsymbol{\Xi}$, the second physical quantity controlling the non-affine shear modulus G_{NA} is the non-affine displacement field $\delta\boldsymbol{r}_{\mathrm{NA}}$. The field $\delta\boldsymbol{r}_{\mathrm{NA}}$ appears as the linear response of the lattice to the force field $\boldsymbol{\Xi}$ [57]. In order to understand the influence of the addition of interaction shells into the lattice we probed the autocorrelation function of the local displacement fields $\delta\boldsymbol{r}_{\mathrm{NA},i}$ at the isostatic point. To simplify the notation, we set $\delta\boldsymbol{r} = \delta\boldsymbol{r}_{\mathrm{NA}}$ and $C_{\delta\boldsymbol{r}}(\boldsymbol{r}) = C_{\delta\boldsymbol{r}_{\mathrm{NA}}}(\boldsymbol{r})$. Then the contribution to the displacement field autocorrelation function between site i and j is defined as

$$\Big[C_{\delta\boldsymbol{r}}(\boldsymbol{r})\Big]_{ij} = \frac{\langle \delta\boldsymbol{r}_i \cdot \delta\boldsymbol{r}_j \rangle - \langle \delta\boldsymbol{r}_i \rangle \cdot \langle \delta\boldsymbol{r}_j \rangle}{\langle \delta\boldsymbol{r}^2 \rangle - \langle \delta\boldsymbol{r} \rangle^2} \tag{3.44}$$

which serves as a measure of both the alignment of the displacement fields at the two sites and their magnitude. In Fig. 3.14 we show the spatial pattern of $C_{\delta\boldsymbol{r}}(\boldsymbol{r})$ for the four interaction ranges $S = 1$, 2, 5, and 15 the their respective critical bond-occupation probabilities. The plots show the full lattices and are not zoomed in. The first striking

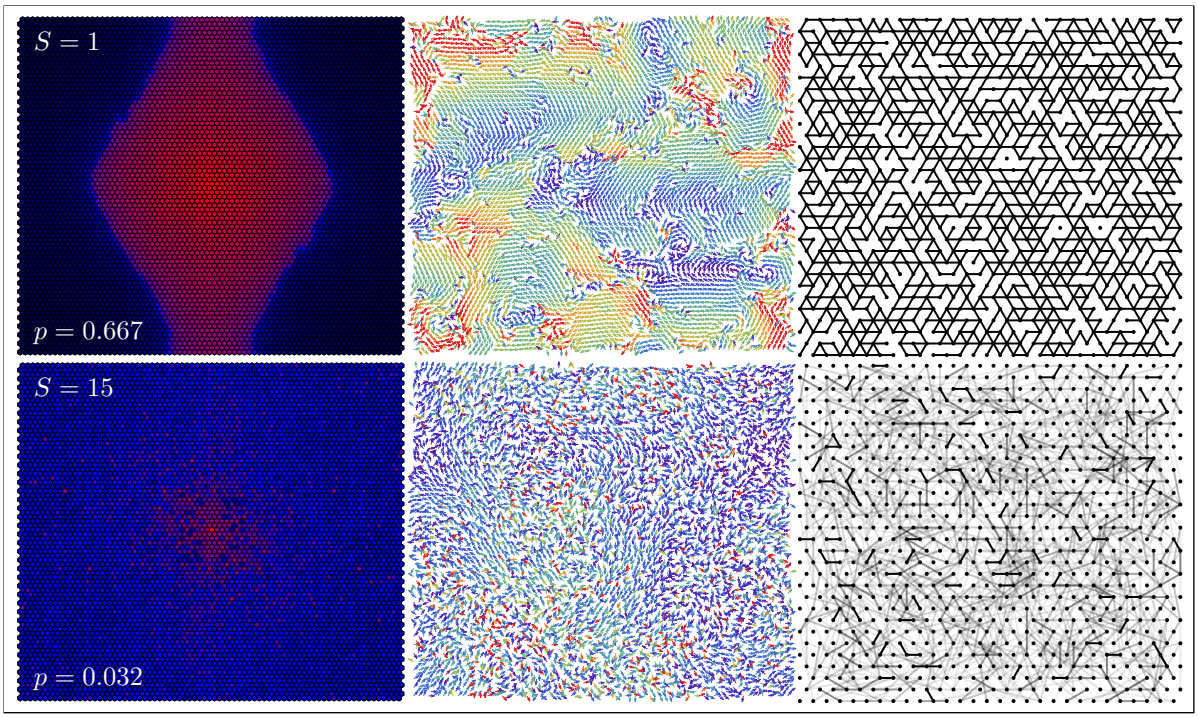

Fig. 3.15 Comparison of the non-affine autocorrelation function C_{NA} (left column), the displacement field of one configuration (centre column), and the bond structure of both the $S = 1$ and $S = 15$ at their respective isostatic points.

observation we make is that the non-affine displacement autocorrelation function for the nearest-neighbour lattice $S = 1$ permeates the full lattice in the vertical direction. A diamond-shaped boundary separates the region of position correlation from the region of negative correlation, with a thin boundary layer, shown in light blue. At this point it is important to note that this form of $C_{\delta \boldsymbol{r}}(\boldsymbol{r})$ arises by the superposition of several patterns which depend on the actual random configuration from which the autocorrelation is computed by statistical averaging. Typically, $C_{\delta \boldsymbol{r}}(\boldsymbol{r})$ completely reaches through the full lattice either from left to right or top to bottom, respecting the periodic boundary conditions. This means that the non-affine particle motion preferentially correlates along the directions $(1, 0)$ and $(0, 1)$, reflecting the structure of the correlation lobes observed in C_{NA}. Interestingly, non-affine displacement correlation which reach through the entire system were observed experimentally in quasi-statically sheared colloidal glasses [16]. When the interaction cutoff is increased, the range of the autocorrelation function $C_{\delta \boldsymbol{r}}$ decreases, while simultaneously diminishing in magnitude.

At $S = 15$, the displacement-displacement correlation pattern is of circular shape.

In order to further understand the development of $C_{\delta \boldsymbol{r}}$ from diamond-like to the circular pattern we compare the two cases at $S = 1$ and $S = 15$. At the isostatic point, both the $S = 1$ and the $S = 15$ lattice have the same average number of neighbours $\langle Z_1 \rangle = \langle Z_2 \rangle = 4$. However, since in the $S = 15$ case, there are 15 different interaction shells from which bonds can be depleted, the resulting bond structure is strikingly different than in the nearest-neighbour lattice. In the right-hand column of Fig. 3.15, we compare the two situations. The bonds of length one, which by virtue of the r^{-3} scaling of the interaction strength are both the shortest and strongest bond, are shown in black. The bonds of longer range in the $S = 15$ lattice are shown as translucent, where the opacity inversely scales with the bond length. As a consequence of the presence of the many long-range bonds and the uniform depletion mechanism, only a very small fraction of strong bonds remain in the case $S = 15$, as can be seen in Fig. 3.15. The distribution of bond orientations is much more isotropic due to the broader distribution of bond angles. In terms of the bond structure we can conclude that the $S = 1$ has a strong backbone of $r_1 = 1$ bonds, whereas in the $S = 15$ consists of a sea of weak bonds with a few localised regions of strong nearest-neighbour bonds. The consequence of this disparate bond topology is that in nearest-neighbour $S = 1$ lattice the influence of disorder-induced non-affine displacements can easier travel trough the lattice. If at one site a particle undergoes a non-affine displacement, it exerts forces on its neighbouring particle which leads to another non-affine displacement, eventually leading to a cooperative effect. As hinted earlier, we know that the non-affine shear modulus and the corresponding non-affine displacements are a non-local quantity since the contain the full eigenvector of the system. This explains why the correlation function $C_{\delta \boldsymbol{r}}$ spans a large portion of the entire lattice. This strong force correlation along the nearest-neighbour bond evidently is not possible in the $S = 15$ lattice. The forces locally arises from a non-affine displacement are distributed much more isotropically and are suppressed by virtue of the r^{-3} scaling of the interaction strength.

This behaviour is also clearly reflected in the actual displacement fields. The central column of Fig. 3.15 shows the local displacement fields $\delta \boldsymbol{r}_i$. The colour gradient used in this plot shows large magnitude displacements in red and small displacements in purple. Specifically, the part of the colour gradient is reached when the displacement field exceeds twice the value of the mean displacement field in the system. We can see that the spatial structure of the displacement vector field shows large regions where many particles cooperatively move in the same direction with a relatively high amplitude. These correspond to precursors of plastic rearrangements in the system which eventually give rise to the yielding of the system under the external shear stress [86]. Also visible

are vortex-like patterns which are characteristic of non-affine displacement fields [62]. In contrast, the displacement fields in the case of the longest interaction cutoff $S = 15$ does not show these patches of large and small displacements. We observe that the displacement vector pattern is much more homogenous than in the $S = 1$ case. Here, the non-affine displacements $\delta\boldsymbol{r}$ are of comparatively smaller amplitude and exhibit a more isotropic distribution in terms the directions of the displacements. Clearly, these aspects can be identified as the cause for the shorter range and more isotropic shape of the displacement correlation function $C_{\delta\boldsymbol{r}}$ in the $S = 15$, also shown in Fig. 3.15.

3.9 Concluding remarks

In summary, using a triangular lattice as a model system we have analysed its elastic heterogeneities and the concomitant spatial elastic correlations to systematically map out the influence of long-range bond and degree of disorder in the lattice, characterised by the shell number S and bond-occupation probability p, respectively. Separately computing the spatial elastic autocorrelation functions of both the affine and non-affine shear moduli, we found that the interplay of bond-depletion and increasing interaction range leads to the appearance of two regimes where the full elastic response is predominantly correlated with either its affine or non-affine contribution. This crossover behaviour can be traced back to the different trends of the fluctuations of the distribution of the local affine and non-affine elastic moduli. We established that a power-law decay of the harmonic interaction with distance leads to power-law decay of the affine elastic autocorrelation function, which at high enough bond-occupation probabilities carries over to the full elastic autocorrelation function. Furthermore, we investigated the spatial structure of the elastic correlation. The quadrupolar shape of affine elastic autocorrelations can be fully explained by the bond-structure and the shear deformation protocol. In addition, we explained the changes of the non-affine elastic autocorrelation patterns in terms of the of the correlations of the affine force and the non-affine displacement fields which constitute G_{NA}.

In particular, we see that the diagonal anticorrelation part of the non-affine elastic autocorrelation function C_{NA} arises due to the affine force field correlations. The positive correlation lobes along the x- and y-axes are caused by the non-affine displacement field $\delta\boldsymbol{r}_{\mathrm{NA}}$ and its correlation structure. The long-ranged correlation lobes of the non-affine elastic autocorrelation C_{NA} stem from the long-range character of $C_{\delta\boldsymbol{r}}$. In the intermediate-p regime we saw that the non-affine elastic correlation lobes become stronger when S is decreased, which is explainable by the stronger relative influence of the nearest-

neighbour backbone in the lattice. Similar elastic correlation pattern have been described in the literature in the framework of the continuum theory of Eshelby [97]. Interestingly, experiments with slowly sheared colloidal glasses in Ref. [16] show elastic correlation patterns resembling the patterns we found. In particular, the same change of symmetry of the elastic autocorrelation was found. The quadrupolar pattern along the x- and y-axes, which we found for example for $S = 1$, $p = 0.850$, was associated to a region of the colloidal glass which behaves solid-like and shows little shear banding. The change from this quadrupolar shape of $C_G(\boldsymbol{r})$ to the isotropic case, very similar to the shape we saw for $S = 15$, $p = 0.032$, was attributed to regions in the colloidal glass of high mobility, where the transition from a solid-like to a liquid-like response has occurred [16]. Despite the fact that our systems harmonic lattices, where of course there is no viscous, liquid-like behaviour possible, these observations align phenomenologically with the physical response expected from our system. At the critical point, the lattice is at the threshold of losing its mechanical stability, where many non-affine displacements occur, which are interpreted as precursors to irreversible plastic rearrangements leading to macroscopic shear flow [62].

3.10 Consequences for the propagation of vibrational excitations

The existence of defects has important consequences for the propagation dynamics of vibrational excitations through the disordered system. In a perfectly crystalline system, vibrational excitations travel as plane wave phonons. The introduction of defects, for example in the form of bond-depletion, inevitably leads to deviations from the phonon-like behaviour, since the waves associated to the vibrational excitations are scattering by the disorder. Instead of remaining extended phononic modes, the vibrations becomes localised in this case.

This can be clearly in Fig. 3.16, which shows the dispersion relation $\omega(\boldsymbol{q})$ obtained from computing the dynamic structure factor $S(\boldsymbol{q}, \omega)$ using the kernel polyomial method, which we introduce in the next chapter. The peak positions of $S(\boldsymbol{q}, \omega)$ define the dispersion relation. The top left panel of Fig. 3.16 shows a clear dispersion, which means that vibrational excitations of a given frequency have a well-defined wave vector. This characterise phononic vibrational modes. Introducing disorder strongly changes the dispersion relation. Vibrational modes no longer can be described as phonons because the dispersion relation experiences significant broadening. This is shown of Fig. 3.16, which depicts $S(\boldsymbol{q}, \omega)$ for the $S = 15$ at increasing degrees of disorder.

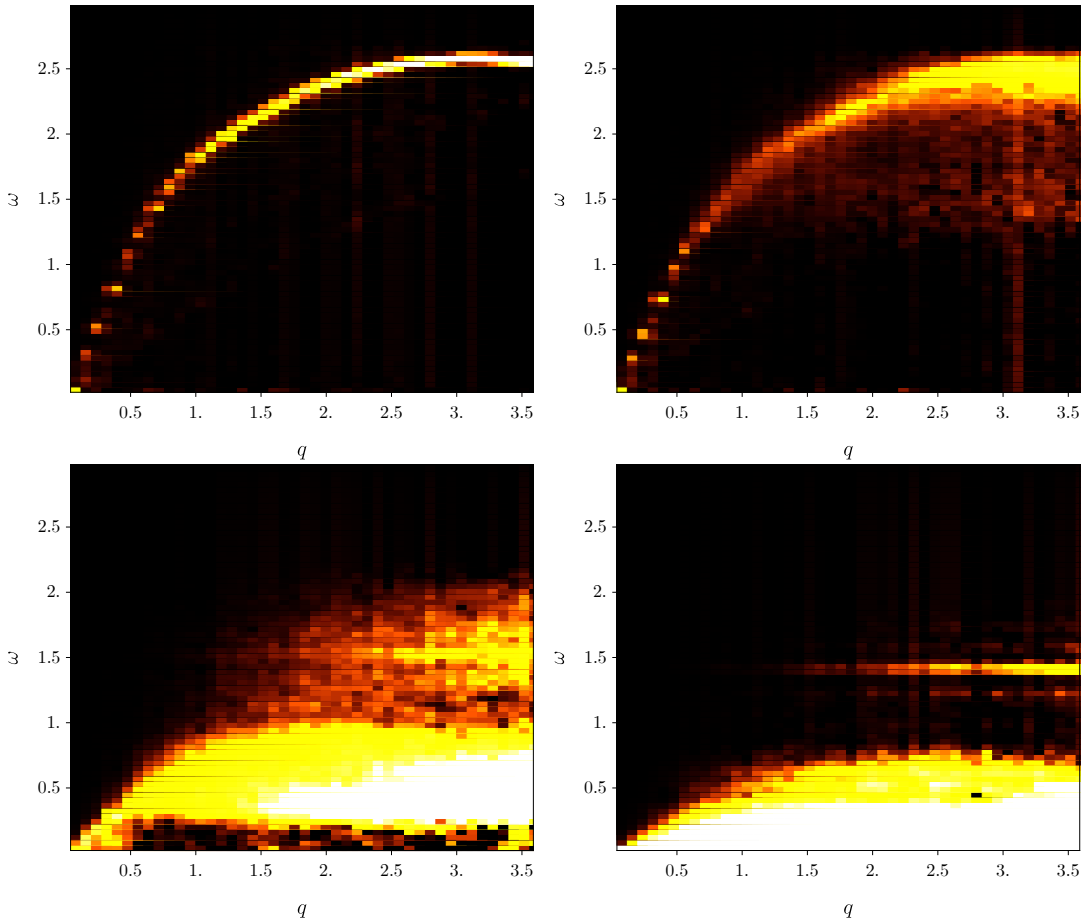

Fig. 3.16 The dispersion $\omega(\boldsymbol{q})$ of the triangular lattice with interaction range $S = 15$. The panels show bond-occupation probabilities $p = 1$, $p = 0.85$, $p = 0.2$, and $p = 0.032$.

In order to characterise the localisation of vibrational modes in the triangular lattice with long-range interactions qualitatively we have computed the participation ratio, which is defined as [66]

$$\mathcal{P}(\omega_p) = \frac{1}{N} \frac{\left(\sum_{i=1}^{N} \boldsymbol{u}_{p,i}^2(\omega_p)\right)^2}{\sum_{i=1}^{N} \boldsymbol{u}_{p,i}^4(\omega_p)} \tag{3.45}$$

where $\boldsymbol{u}_{p,i}^2$ represent the eigenvector components of particles. For extended vibrational excitations $\mathcal{P}(\omega)$ is of order one, whereas for localised excitations the participation ratio scales as $1/N$ where N is the particle number. The results for the model system of this chapter can be seen in Fig. 3.17. It can be clearly seen that the introduction of long-range bonds into the lattice has a significant effect on the localisation of vibration modes. At larger interaction ranges, there is a larger portion of delocalised modes present which hints at a stronger quasi-periodic bond backbone. It also appears that the point of the

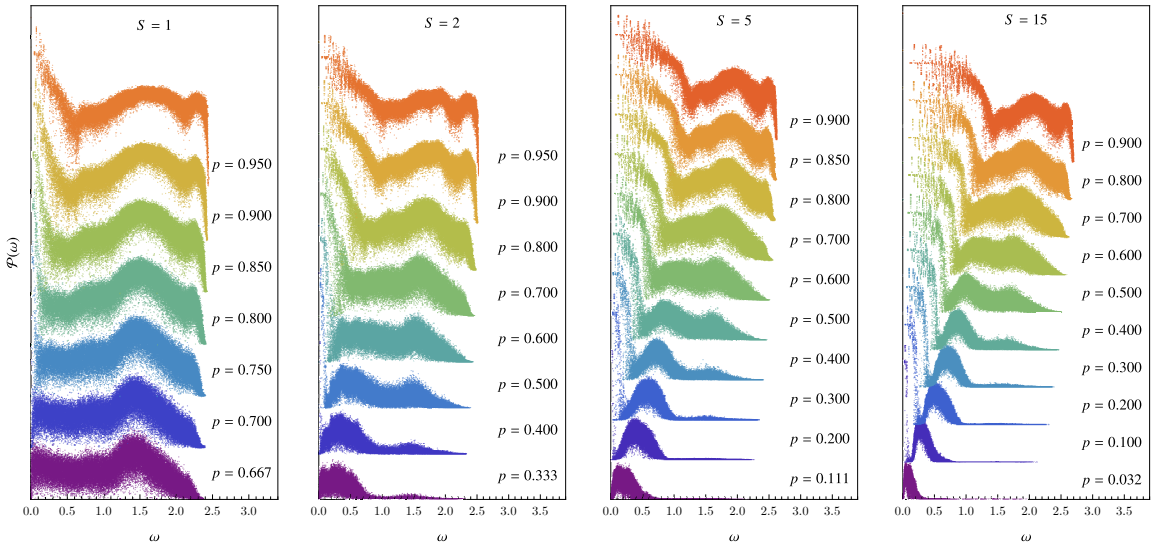

Fig. 3.17 The participation ratios $\mathcal{P}(\omega)$ for the long-range triangular lattice for different interaction ranges $S = 1$, $S = 2$, $S = 5$, and $S = 15$.

transition between the localised modes, signified by a very low value of the participation ration and the delocalised modes moves to higher frequencies. This transition is associated with the Ioffe-Regel limit [83, 6], which points to the threshold where the spatial extension of quasi-localised modes becomes comparable to the spacing between defects in the system. The Ioffe-Regel transition therefore consists of a crossover from weak to strong scattering of vibrational modes. As discussed in the Introduction, it was recently established that elastic correlation in glasses modify the scattering mechanism of vibrational modes which shows in a deviation from the Rayleigh scattering regime [42]. This regime is characterised by a $|\boldsymbol{q}|^3$ scaling of the width $\Gamma(\boldsymbol{q})$ of the dynamic structure factor $S(\boldsymbol{q}, \omega)$ in two dimensions at low frequencies, which governs the attenuation of vibrational modes via the scattering at disorder. In Ref. [42] it was reported that power-law correlations in the material lead to a logarithmic correction factor to the Rayleigh scattering law. It is, however, noteworthy that the mere presence of long-range bonds with a power-law decay of the stiffness can lead to a logarithmic correction of the dispersion relation for one-dimensional linear chains without disorder. This is explained in Appendix C. For this reason it would be very interesting to map out the consequences of long-range interactions for the Ioffe-Regel transition in order to clarify the effect of the long-range bonds on the propagation dynamics of the vibrational excitations. This means that to obtain further insights into the physics behind the altered scattering mechanism reported in Ref. [42], the behaviour of $\Gamma(\boldsymbol{q})$ has to be studied for our model system in dependence on the interaction range and degree of bond-depletion.

Chapter 4

Approximate description of vibrational and viscoelastic properties

The analysis of the spectral density of dynamical matrices and their eigenvector characteristics is the key component when describing mechanical and thermodynamical properties of disordered solids within the framework of non-affine lattice dynamics. However, for a very large number of particles needed to model a system realistically, direct diagonalisation ceases to be a viable method to obtain the eigenfrequencies and eigenmodes. This is the case because the memory requirement for numerically computing the eigenvalues, and in particular the eigenvectors, of the Hessian matrix become extremely high for systems larger than $N = 10^4$. Therefore, if we want to conduct an analysis of the properties of the eigenfrequency spectrum and the corresponding eigenvectors, we have to resort to an approximation scheme.

One prominent candidate, which we introduce in this chapter is the so-called kernel polynomial method (KPM) for the analysis of eigenvalues and eigenvectors of very large sparse matrices based on the expansion of the eigenvalue spectral density into Chebyshev polynomials [96]. The approximation then consists of a truncation of the series expansion at finite order and a consecutive stochastic approximation of the series coefficients. The KPM has been successfully applied to a variety of different physical problems, most importantly the approximation of dynamical correlation functions in both classical and quantum systems. For example, in Ref. [5] the dynamic structure factor and spatial eigenvector correlation function of amorphous silicon were analysed based on a normal mode analysis. Furthermore, the KPM was used to compute the Green's function and the dynamical optical conductivity of fermionic quantum systems [96]. The goal of the

present chapter is to apply the kernel polynomial method to the problem of computing the viscoelastic response of a disordered system following the theoretical framework of non-affine lattice dynamics described in Chapter 1. This approach is based on approximating the non-affine correlator $\Gamma(\omega)$ using KPM which has not been described before. In addition to that, introducing compositional disorder into the system, i.e. allowing for variations of the particles masses has a non-trivial effect on the frequency-dependent viscoelastic spectrum. This necessitates an extension of the non-affine expression for the frequency-dependent shear modulus Eq. (1.48) based on the generalised eigenvalue problem in order to facilitate an accurate description in the presence of compositional disorder by explicitly taking into account the contributions from different masses. As an example, the problem will be studied for the case of a heteropolymer model consisting of three different masses.

4.1 Vibrational density of states from KPM

The focus in the first section will be to describe the general framework needed to set up the KPM algorithm for the computation of the eigenfrequency spectrum of a generic Hessian matrix. We consider a real-valued function $f(x)$ on the interval $[a, b]$. The core idea behind the kernel polynomial approximation is to expand the function $f(x)$ into a series of Chebyshev polynomials of the second kind $U_k(x)$ [96], i.e.

$$f(x) = \sum_{n=0}^{\infty} \alpha_k U_k(x). \tag{4.1}$$

Introducing the weighted scalar product on the interval $[-1, 1]$,

$$\langle f | \, g \rangle_\xi = \int_{-1}^{1} \xi(x) f(x) g(x) \, \mathrm{d}x \tag{4.2}$$

the Chebyshev polynomials of the second kind are orthogonal with respect to the weight $w(x) = \pi\sqrt{1 - x^2}$, i.e.

$$\langle U_k | \, U_l \rangle_w = \frac{\pi^2}{2} \delta_{k,l} \tag{4.3}$$

where $\delta_{k,l}$ represents the Kronecker delta. Hence, the expansion coefficients α_k appearing in Eq. (4.1) are given by

$$\alpha_k = \frac{2}{\pi} \int_{-1}^{1} \sqrt{1 - x^2} U_k(x) f(x) \, \mathrm{d}x. \tag{4.4}$$

In addition, the Chebyshev polynomials $U_k(x)$ can be computed using the recurrence relations

$$\begin{aligned} U_0(x) &= 1 \\ U_1(x) &= 2x \\ U_k(x) &= 2xU_{k-1}(x) - U_k(x) \end{aligned} \tag{4.5}$$

or, equivalently, can be defined through their trigonometric representation

$$U_k(x) = \frac{\sin\left[(k+1)\arccos x\right]}{\sqrt{1-x^2}}. \tag{4.6}$$

Having laid out the groundwork, we can now proceed to consider the problem of expanding the vibrational density of states defined as

$$\rho(\omega) = \frac{1}{N}\sum_i \delta(\omega - \omega_i). \tag{4.7}$$

into Chebyshev polynomials. The function $\rho(\omega)$ is the distribution of eigenfrequencies which result from the generic eigenvalue problem $\mathbf{H}\boldsymbol{x}_i = \lambda_i \boldsymbol{x}_i$. Usually the matrix $\mathbf{H}$ represents the Hessian matrix of an interacting particle system, where the eigenvalue represent the vibrational eigenfrequencies, i.e. $\lambda_i = \omega_i^2$. Since the set of eigenvalues $\{\lambda_i\}_{i\in 1,\dots,3N}$ of the underlying $3N \times 3N$ Hessian matrix are just the squared eigenfrequencies, we can use the variable transformation $\lambda = \omega^2$ and write the DOS as

$$\rho(\omega) = \frac{2\omega}{3N}\sum_i \delta(\omega^2 - \omega_i^2) = \frac{2\omega}{3N}\sum_i \delta(\lambda - \lambda_i). \tag{4.8}$$

In order to allow for the KPM treatment, the support of the function $\rho(\omega)$ has to be mapped onto the interval $[-1, 1]$, to permit the expansion in terms of Chebyshev polynomials. We thus have to express the DOS in terms of a rescaled variable $\widetilde{\lambda}$, such that the original support of eigenvalues $[\lambda_{\min}, \lambda_{\max}]$ is mapped onto $[-1, 1] \ni \widetilde{\lambda}$. This can

be achieved by a linear transformation of the eigenvalue problem, which is given by [96]

$$\begin{aligned}\widetilde{H} &= \frac{H - \mathbb{1}b}{a} \\ \widetilde{\lambda} &= \frac{\lambda - b}{a} \\ a &= \frac{\lambda_{\max} - \lambda_{\min}}{2 - \varepsilon} \\ b &= \frac{\lambda_{\max} + \lambda_{\min}}{2}.\end{aligned}$$

where ε is a small parameter which serves the function to stabilise the convergence of the kernel polynomial method against unwanted fluctuations at the edges of the support of the eigenvalue spectrum, known as Gibbs oscillations. Using this transformation we can express the DOS as

$$\rho(\omega) = \frac{2\omega}{3N} \frac{2 - \varepsilon}{\lambda_{\max} - \lambda_{\min}} \sum_j \delta(\widetilde{\lambda} - \widetilde{\lambda}_j). \tag{4.9}$$

We now apply the abovementioned approach and expand the δ-function appearing in Eq. (4.9) in terms of the Chebyshev polynomials $U_k(\widetilde{\lambda})$. Making use of the relation $\int f(y)\delta(x - y)\,\mathrm{d}y = f(x)$, we can express the δ-function as [5]

$$\delta(\widetilde{\lambda} - \widetilde{\lambda}_p) = \frac{2}{\pi}\sqrt{1 - \widetilde{\lambda}^2} \sum_{k=0}^{\infty} U_k(\widetilde{\lambda}) U_k(\widetilde{\lambda_p}). \tag{4.10}$$

Plugging in the trigonometric definitions of the Chebyshev polynomials, we can proceed to write series expansion as [5]

$$\rho(\omega) = \frac{4\omega}{3N\pi} \frac{2 - \varepsilon}{\lambda_{\max} - \lambda_{\min}} \sum_{k=0}^{\infty} \mu_k \sin\left[(k+1)\arccos\widetilde{\lambda}\right] \tag{4.11}$$

where we have introduced the Chebyshev moments defined by

$$\mu_k = \frac{1}{3N} \sum_{j=1}^{3N} U_k(\widetilde{\lambda}_j). \tag{4.12}$$

The approximation then essentially consists of truncating the infinite series at a finite order such that

$$\delta(\widetilde{\lambda} - \widetilde{\lambda}_j) \approx \frac{2}{\pi}\sqrt{1 - \widetilde{\lambda}^2} \sum_{k=0}^{K} \gamma_k U_k(\widetilde{\lambda}_j) U_k(\widetilde{\lambda}). \tag{4.13}$$

At this point the damping factor γ_k has to be introduced to counteract so-called Gibbs oscillations. The damping induced by γ_k effectively truncate the series expansion gradually to avoid the oscillatory fluctuations which would appear if the sum were truncated abruptly [5, 96]. By substituting this truncated series into the expression for the DOS in Eq. (4.9) we obtain the approximate vDOS as

$$\rho(\omega) = \frac{4\omega}{3N\pi} \frac{2-\varepsilon}{\lambda_{\max} - \lambda_{\min}} \sum_{k=0}^{K} \gamma_k \mu_k \sin\left[(k+1)\arccos\widetilde{\lambda}\right] \tag{4.14}$$

where K denotes the degree of the approximation which basically sets the resolution of the algorithm for approximating the δ-peaks which constitute the vDOS.

The above summation can be carried out numerically. It now remains to treat the moments μ_k. Considering Eq. (4.12), we observe that the moments μ_k can be written as

$$\mu_k = \frac{1}{3N} \sum_{p=1}^{3N} \langle \boldsymbol{p} |\, U_k(\widetilde{\mathbf{H}})\, | \boldsymbol{p} \rangle \tag{4.15}$$

where $|\boldsymbol{p}\rangle$ represents the normalised eigenvector of the rescaled Hessian matrix $\widetilde{\mathbf{H}}$. The central point of the KPM is that the above trace can be approximated stochastically very accurately if the matrix $\widetilde{\mathbf{H}}$ becomes very large [96]. This means that instead of evaluating the trace over the full set of all eigenvectors we initialise a number of normalised Gaussian random vectors $|\boldsymbol{u}_0\rangle$ which we want to use for the evaluation of the above trace. To see how this works, let us first expand one realisation of the Gaussian random vector in terms of the eigenvectors of the matrix $\widetilde{\mathbf{H}}$, i.e.

$$|\boldsymbol{u}_0\rangle = \sum_p |\boldsymbol{p}\rangle\langle \boldsymbol{p}|\, \boldsymbol{u}_0\rangle = \sum_p \alpha_p\, |\boldsymbol{p}\rangle\,. \tag{4.16}$$

Hence, using this expansion we obtain for the matrix elements

$$\langle \boldsymbol{u}_0 |\, U_k(\widetilde{\mathbf{H}})\, | \boldsymbol{u}_0 \rangle = \sum_{p=1}^{3N} |\alpha_p|^2\, U_k(\widetilde{\lambda}_p) \tag{4.17}$$

which holds by virtue of the orthonormality of the eigenvectors. The components of the random vector $|\boldsymbol{u}_0\rangle$ in an arbitrary basis, i.e. both the components $u_{0,i}$ and α_p, are independently and identically distributed. They have zero expectation value and unit variance, i.e. $\langle\!\langle \alpha_p \rangle\!\rangle = 0$ and $\langle\!\langle \alpha_p^* \alpha_q \rangle\!\rangle = \delta_{p,q}/(3N)$, where $\langle\!\langle \ldots \rangle\!\rangle$ denotes the expectation value with respect to the Gaussian probability distribution. Therefore, taking the

expectation value of Eq. (4.17), we obtain

$$\begin{aligned}\left\langle\!\!\left\langle \langle \boldsymbol{u}_0 | \, U_k(\widetilde{\mathbf{H}}) \, | \boldsymbol{u}_0 \rangle \right\rangle\!\!\right\rangle &= \sum_{p=1}^{3N} \langle\!\langle |\alpha_p|^2 \rangle\!\rangle U_k(\widetilde{\lambda}_p) \\ &= \frac{1}{3N} \sum_{p=1}^{3N} U_k(\widetilde{\lambda}_p) = \mu_k \end{aligned} \tag{4.18}$$

since the random vectors $\boldsymbol{u}_0$ are normalised to one, which entails that $\langle\!\langle |\alpha_p|^2 \rangle\!\rangle = 1/(3N)$ [5]. This means in conclusion that we can stochastically approximate the Chebyshev moments as $\mu_k \approx \langle\!\langle \langle \boldsymbol{u}_0 | \, U_k(\widetilde{\mathbf{H}}) \, | \boldsymbol{u}_0 \rangle \rangle\!\rangle$. Setting $|\boldsymbol{u}_k\rangle = U_k(\widetilde{\mathbf{H}}) \, |\boldsymbol{u}_0\rangle$ and $m_k = \langle \boldsymbol{u}_0 | \, \boldsymbol{u}_k \rangle$ we see that after averaging over many realisations of the random vector $|\boldsymbol{u}_0\rangle$, m_k will converge to μ_k, i.e. $\langle\!\langle m_k \rangle\!\rangle \to \mu_k$ [5]. The relative error of the stochastic approximation of the trace is of the order $\mathcal{O}(\sqrt{RN})$ [96], where R is the number of random vectors drawn from the Gaussian ensemble. Therefore, starting from $|\boldsymbol{u}_0\rangle$ we can consecutively compute the Chebyshev moments μ_k by applying the recurrence relation defining the Chebychev polynomials. In the first iteration, $|\boldsymbol{u}_1\rangle$ is obtained by using Eq. (4.5)

$$|\boldsymbol{u}_1\rangle = \widetilde{\mathbf{H}} \, |\boldsymbol{u}_0\rangle \tag{4.19}$$

and by further applying the recurrence relation this continues to

$$|\boldsymbol{u}_k\rangle = 2\widetilde{\mathbf{H}} \, |\boldsymbol{u}_{k-1}\rangle - |\boldsymbol{u}_{k-2}\rangle \, . \tag{4.20}$$

In the remaining part of this chapter we will now consider the application and extension of the kernel polynomial approximation to study the vibration and mechanical properties of disordered condensed matter systems.

4.2 Approximation of the non-affine correlator $\Gamma(\omega)$

Having laid out the KPM for computing approximations to the vDOS $\rho(\omega)$, it remains to adapt the approach for estimating the non-affine correlator $\Gamma(\omega)$ in order to allow for a full analysis using non-affine lattice dynamics. Since the relevant quantity appearing the expression for complex viscoelastic shear modulus is the product of the Γ-correlator and the density states $\rho(\omega)$, we now set out to derive the expressions necessary for the application of the KPM. Setting aside the averaging over frequency shells, $\Gamma(\omega)$ is defined as the squared norm of the projection of the eigenvectors of the Hessian matrix onto

the affine force field of the disordered particle system, i.e. $|\langle \boldsymbol{\Xi}|\, \boldsymbol{p}\rangle|^2$, where again $|\boldsymbol{p}\rangle$ represents an eigenvector of the Hessian matrix.

Since the ansatz of the KPM starts with the decomposition of the δ-function, we will directly access the distribution of the product of $|\langle \boldsymbol{\Xi}|\, \boldsymbol{p}\rangle|^2$ and $\rho(\omega)$ with the KPM. With this expectation in mind, we start by considering the function which will approximate the above product, i.e.

$$\begin{aligned}\mathcal{J}(\omega) =& \frac{2\omega}{3N}\frac{2-\varepsilon}{\lambda_{\max}-\lambda_{\min}}\sum_p \langle \boldsymbol{\Xi}|\, \boldsymbol{p}\rangle\langle \boldsymbol{p}\,|\boldsymbol{\Xi}\rangle\, \delta(\widetilde{\lambda}-\widetilde{\lambda}_p)\\ =& \frac{4\omega}{3N\pi}\frac{2-\varepsilon}{\lambda_{\max}-\lambda_{\min}}\sum_{k=0}^{\infty}\gamma_k\mu_k \sin\Big[(k+1)\arccos\widetilde{\lambda}\Big]\end{aligned} \tag{4.21}$$

where now the expansion coefficients μ_k take the form

$$\mu_k = \frac{1}{3N}\sum_p \langle \boldsymbol{\Xi}|\, \boldsymbol{p}\rangle\langle \boldsymbol{p}\,|\boldsymbol{\Xi}\rangle\, U_k(\widetilde{\lambda}_p). \tag{4.22}$$

In analogy to Eq. (4.15), we now want to pull in the Chebyshev polynomial $U_k(\widetilde{\lambda}_p)$ into the scalar product above in order to make use of the relation $U_k(\widetilde{\lambda}_p)\,|\boldsymbol{p}\rangle = U_k(\widetilde{\mathbf{H}})\,|\boldsymbol{p}\rangle$. We continue by first rearranging Eq. (4.22) and then apply the above relation, which yields

$$\begin{aligned}\mu_k =& \frac{1}{3N}\sum_p \langle \boldsymbol{p}\,|\boldsymbol{\Xi}\rangle\, \langle \boldsymbol{\Xi}|\, \boldsymbol{p}\rangle U_k(\widetilde{\lambda}_p)\\ =& \frac{1}{3N}\sum_p \langle \boldsymbol{p}\,|\boldsymbol{\Xi}\rangle\, \langle \boldsymbol{\Xi}|\, U_k(\widetilde{\mathbf{H}})|\boldsymbol{p}\rangle\end{aligned} \tag{4.23}$$

In this form we again have a trace at hand which we can tackle using the stochastic approximation introduced earlier. We again expand the random vector $|\boldsymbol{u}_0\rangle$ with respect to the eigenvector of the transformed Hessian $\widetilde{\mathbf{H}}$ and write the statistical average of the trace as

$$\Big\langle\!\Big\langle \langle \boldsymbol{u}_0\,|\boldsymbol{\Xi}\rangle\langle \boldsymbol{\Xi}|\, U_k(\widetilde{\mathbf{H}})\,|\boldsymbol{u}_0\rangle \Big\rangle\!\Big\rangle = \Big\langle\!\Big\langle \sum_{p,q}\alpha_p^*\alpha_q \langle \boldsymbol{p}\,|\boldsymbol{\Xi}\rangle\langle \boldsymbol{\Xi}|\, U_k(\widetilde{\mathbf{H}})\,|\boldsymbol{q}\rangle \Big\rangle\!\Big\rangle. \tag{4.24}$$

Since the components of the random vector fullfill $\langle\!\langle \alpha_p\alpha_q\rangle\!\rangle = \delta_{p,q}/(3N)$ the above equation is reduced to

$$\Big\langle\!\Big\langle \langle \boldsymbol{u}_0\,|\boldsymbol{\Xi}\rangle\langle \boldsymbol{\Xi}|\, U_k(\widetilde{\mathbf{H}})\,|\boldsymbol{u}_0\rangle \Big\rangle\!\Big\rangle = \frac{1}{3N}\sum_p \langle \boldsymbol{p}\,|\boldsymbol{\Xi}\rangle\langle \boldsymbol{\Xi}|\, U_k(\widetilde{\mathbf{H}})\,|\boldsymbol{p}\rangle = \mu_k \tag{4.25}$$

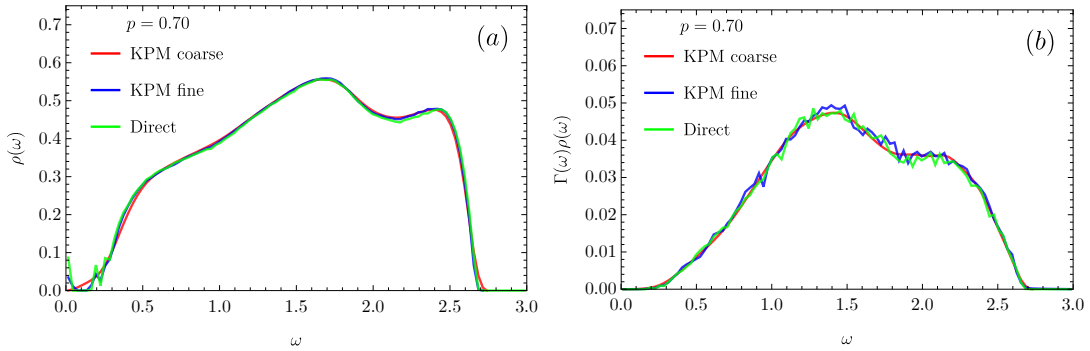

Fig. 4.1 Comparison of the results obtained from the KPM with the results from direct diagonalisation. The polynomial degree of the coarse and fine KPM curve is $K = 50$ and $K = 300$, respectively.

which takes us back to Eq. (4.22) and therefore is the desired result. Using the same notation as for the KPM discussion of the density of states, i.e. $|\boldsymbol{u}_k\rangle = U_k(\widetilde{\mathbf{H}})\,|\boldsymbol{u}_0\rangle$, we conclude that the expression

$$m_k = \langle \boldsymbol{u}_0\,|\boldsymbol{\Xi}\rangle\langle\boldsymbol{\Xi}|\,U_k(\widetilde{\mathbf{H}})\,|\boldsymbol{u}_0\rangle \tag{4.26}$$

is the correct approximate Chebyshev moment which stochastically converges to μ_k, in the sense that $\langle\!\langle m_k \rangle\!\rangle \to \mu_k$.

As we observe in the numerical computations, the convergence rate for the function $\mathcal{J}(\omega)$ is dramatically slower than for $\rho(\omega)$. This means a significantly larger number R of sample random vectors has to be drawn in order to achieve a good approximation. The reason for this might be the fact that the components of the vector $\boldsymbol{\Xi}$ are distributed across a rather wide range in comparison to the zero mean, unit variance distribution of the elements of the random vector $|\boldsymbol{u}_0\rangle$. The variance for example for the polymer system discussed later is of the order 10^4. This high degree of fluctuations is inherited by the product $\langle \boldsymbol{u}_0|\,\Xi\rangle$ and thus slows down the convergence rate of the KPM algorithm. In fact, the distribution of the components of $\boldsymbol{\Xi}$ is roughly Gaussian for each individual coordinate. However, the crucial difference is that not only is the distribution of the values centred at 0 but is actually exactly constrained to be zero, since the system is in a global force equilibrium.

4.3 First comparison with direct diagonalisation

As a first application, to prove the methodology, we investigate the applicability of the kernel polynomial method to the problem of computing the complex viscoelastic response

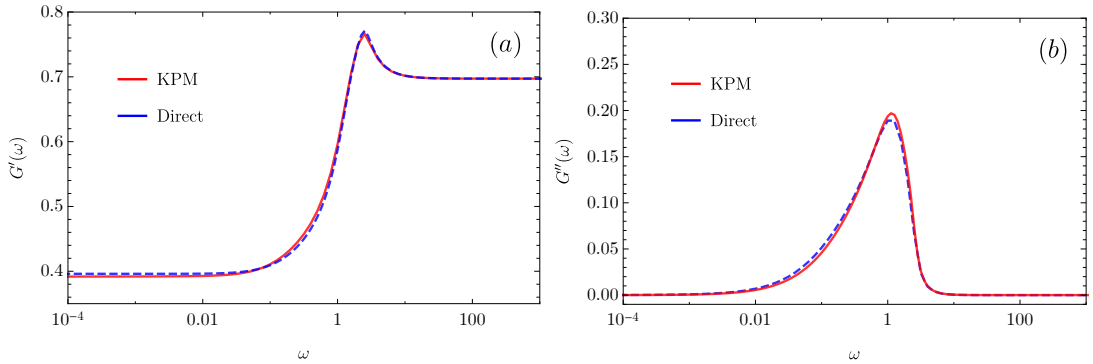

Fig. 4.2 The complex viscoelastic modulus $G^*(\omega) = G'(\omega) + iG''(\omega)$ obtained using the KPM and direct diagonalisation for the depleted fcc crystal with bond-occupation probability $p = 0.70$ and friction $\nu = 1$.

of a depleted fcc crystal. This requires that we compute the vibrational density of states as well as the frequency correlator of the non-affine elastic correction, the $\Gamma(\omega)$-function.

We have computed $D(\omega)$ and $\Gamma(\omega)$ with KPM using two different resolutions to compare the convergence behaviour of the approximation functions. The *coarse* approximation uses polynomials up to a degree of 50, and the *fine* approximation uses polynomials up to degree 300. For both the coarse and fine approximation we work with 10000 samples of the basis vector u_0 to achieve a good convergence of the random trace average. The depleted fcc crystal at hand has a bond-occupation probability of $p = 0.7$, consists of $N = 4000$, and 5 realisations at this point. From Fig. 4.1(a) we can see that the high-frequency part of the vDOS computed by direct diagonalisation is well represented by KPM for both the coarse and fine setups. However, at low frequencies close to $\omega = 0$ it becomes obvious that the coarse version of KPM cannot wrap the finer details of the DOS. This feature of KPM will become crucial later in this chapter when we consider the approximation of the vibrational properties of a polymer melt. The Hessian matrix there inherently exhibits negative eigenvalues, i.e. the approximation needs to have a fine enough resolution to capture the transition into the negative support of the spectrum.

The situation looks similar when computing the frequency correlator $\Gamma(\omega)$ with the KPM. However, here we observe that the KPM even when using the higher polynomial degree does not converge very well to the result obtained by direct diagonalisation. This can the traced back to the fact that in the KPM algorithm there appears a scalar product between a Gaussian random vector and the affine force field, which is fixed for a given configuration. This inevitably leads to an large increase in fluctuations. The distribution of the elements is Gaussian-like but has a very large variance, compared to

the $\mathcal{N}(0,1)$-distributed elements of the random vector appearing in the KPM. As we will see later, a rather large number of iterations is needed to converge the kernel polynomial approximation to a high degree in the case of the $\Gamma(\omega)$-correlator.

With regard to accessing the viscoelastic response of the depleted fcc system this does not appear to be a big problem. As we can see in Fig. 4.2, showing the complex-valued viscoelastic modulus $G^*(\omega) = G'(\omega) + iG''(\omega)$, the match between the result obtained using the KPM with the finer resolution of $K = 300$ exhibits a very good match with the viscoelastic response computed from the vDOS and $\Gamma(\omega)$ via direct diagonalisation.

4.4 Application to polymer systems

In this section we will combine the approximation technique of the KPM and the extension of the non-affine formalism to multi-component systems in order to study the contributions from different masses to the vDOS, the non-affine correlator $\Gamma(\omega)$, and eventually the dynamic viscoelastic response to an external oscillatory shear strain. The goal of this approach is to have a tool at hand which allows to extract the viscoelastic response of a large multi-component system, possibly with temperature as a system parameter. This approach could be very useful for studying the viscoelastic and vibrational properties of the glass transition of a multi-component polymeric systems both in the setting of coarse-grained and atomistic molecular dynamics simulations.

4.4.1 Multi-component polymer model system

We want to move forward from the picture of a zero-temperature disordered crystal to more complex systems. In particular, we are interested in the applicability of non-affine lattice dynamics to the description for the linear viscoelastic response of polymeric systems at non-zero temperatures. In addition to that we will use the extension of the non-affine framework to multi-component polymer chains. The complex modulus $G^*(\omega)$ will be obtained both directly from a molecular dynamics simulation and from the solution of the equations of motion of non-affine lattice dynamics. The two main goals are to set up the framework for computing the vibrational and viscoelastic properties of disordered multi-component systems and the adaptation of the kernel polynomial method to this problem.

The model system of choice for this purpose is a that of a coarse-grained polymer system consisting of linear chains of 100 monomers which are generated using LAMMPS [91]. In particular, the polymer chain under consideration consist of three different mass

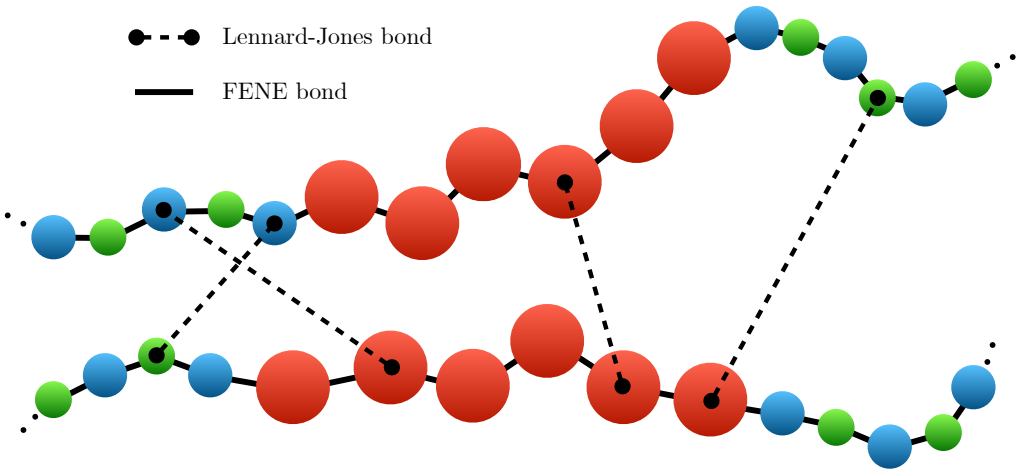

Fig. 4.3 Sketch of two polymer chains as they appear in the model system. Some of the Lennard-Jones bonds between the chains are depicted as dashed lines. The FENE bonds along the polymer chain are represented as solid lines.

species, where the three masses are chose as $m_1 = 1$, $m_2 = 3$ and $m_3 = 10$. The geometry of the chain is such that the six heavy monomers of mass m_3 are placed at the centre of each chain. On the remaining sites along the polymer chain particles of masses m_1 and m_2 are placed in alternating fashion, as illustrated in Fig. 4.3.

The polymer chains are embedded in a three-dimensional box subject to periodic boundary conditions and the Kremer-Grest model is used to describe the interactions within and between the polymers [55]. In the Kremer-Grest model each constituent monomer is allowed to interact via a Lennard-Jones potential

$$U_{\mathrm{LJ}}(r) = 4\epsilon\left[\left(\frac{\sigma}{r}\right)^{12} - \left(\frac{\sigma}{r}\right)^{6} - \left(\left(\frac{\sigma}{r_c}\right)^{12} - \left(\frac{\sigma}{r_c}\right)^{6}\right)\right] \tag{4.27}$$

where the parameters are chosen as $\varepsilon = 1$, $\sigma = 1$. The cutoff radius of the potential is set to $r_c = 2.5$. In addition, the Kremer-Grest model contains attractive along-the-chain bonds, as depicted in Fig. 4.3. This interaction is mediated by a finite extensible nonlinear elastic (FENE) potential given by [55]

$$U_{\mathrm{FENE}}(r) = -\frac{Kr_0^2}{2}\ln\left[1 - \left(\frac{r}{r_0}\right)^2\right]. \tag{4.28}$$

The interaction parameters of the FENE interaction are $K = 30$ and $r_0 = 1.5$. A Langevin thermostat was used for the molecular dynamics simulations where particles experience a viscous damping force proportional to the velocity. The corresponding damping constant ξ, which is related to the damping term appearing in the lattice dynamical equation of

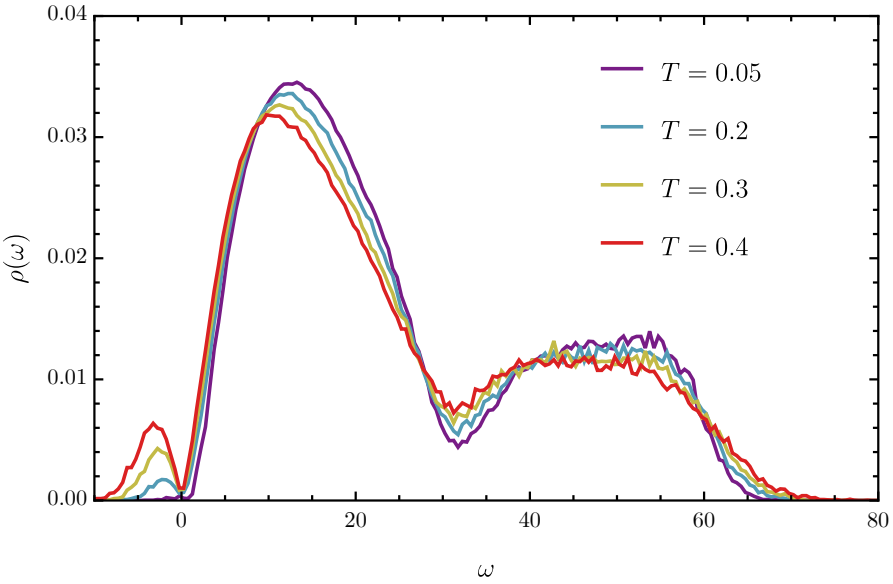

Fig. 4.4 The vibrational density of states of a system of polymer chains as described in the main text with $m_1 = m_2 = m_3$ at he different temperature. The value $T = 0.4$ corresponds to the glass transition temperature of this system. For visual clarity the imaginary frequencies have been shifted to the negative real axis by setting $\mathrm{Im}\,\omega \to -\omega$.

motion by $\xi = m\nu$. Using dimensionless LJ units in terms of the mass m, length d and energy ϵ, we set $\sigma = 1$ and $\epsilon = 1$, which results in a fundamental unit of time given by $\tau = \sqrt{m\sigma^2/\epsilon}$. The system is equilibrated in a melted state at $T^* = 1$, maintaining zero external pressure using a Nose-Hoover barostat. Subsequently, the system is cooled by decreasing T^* at a rate $\tau_c \sim \mathcal{O}(10^5)\tau$. The details of the simulations are the same as in Ref. [91] and were carried out by Vladimir Palyulin.

4.4.2 Instantaneous normal modes and non-affine lattice dynamics

One of the essential points of non-affine lattice dynamics is the diagonalisation of the dynamical or Hessian matrix $\mathbf{H}$ which allows for the expansion of the affine force field $\boldsymbol{\Xi}$ and displacements $\delta\boldsymbol{r}$ with respect to the eigenbasis of $\mathbf{H}$ and the subsequent description of the complex viscoelastic moduli $G^*(\omega)$. In the bond-depleted fcc crystal, whose viscoelastic response we briefly characterised in the previous section, we have assumed in addition to zero temperature that the interactions between the particles are harmonic. The zero temperature assumption in a lattice without internal stresses means that the configuration $\boldsymbol{R} = \{\boldsymbol{r}_1, \ldots \boldsymbol{r}_N\}$ of the crystal permanently resides in a minimum of the potential energy landscape $U(\boldsymbol{R})$. Consequently, the vibrational dynamics of the crystal

is fully described by the eigenmodes of the underlying Hessian matrix **H**. In the case of a polymer system whose monomers interact via Lennard-Jones and FENE bonds at a finite temperature the situation is vastly more complex and the configuration of all monomers will practically never be in a minimum of the potential energy landscape [53].

The central idea is to generate configurations of the polymer system via MD simulations and consider one sample of these configurations at an instant of time t_0. From this configuration the Hessian matrix is computed and can be used as the starting point for an analysis using non-affine lattice dynamics. This concept of obtaining the dynamical matrix from a snapshot configuration was pioneered by Rahman et al. [75]. Therefore, each snapshot of the system at different times t_0 corresponds a different configuration with a different Hessian matrix, and consequently a different set of eigenvectors or normal modes. For this reason they are called instantaneous normal normal modes (INM). Since a given microscopic configuration will rapidly evolve, it is inherent in the approach of using configurational snapshot that the resulting dynamics governed by the INM can only be a good approximation on short time scales [85].

Regions of the potential energy landscape then exhibit saddles and barriers, which allow for transition between different configurations. Applying the harmonic approximation in this case means that the resulting Hessian matrix ceases to be a positive semi-definite matrix. Consequently, the eigenvalue spectrum of the Hessian will have some negative eigenvalues, which indicate a negative curvature of $U(\boldsymbol{R})$. The positive part of the eigenvalue spectrum corresponds to vibrational modes which oscillate around the harmonic minima, while the negative part corresponds to saddles and barriers in the potential energy landscape [51]. These parts with negative curvature are linked to instabilities in the energy landscape where the system does not oscillate around a minimum but finds a direction in which it can transition to a different configuration. Clearly, these directions in the potential energy landscape are necessary for diffusive motion and dissipative structural relaxation through barrier hopping [52], which is connected to the loss of mechanical stability at the onset of the glass transition. In addition to that, resorting to the analogy of a simple harmonic oscillating motion of the amplitude proportional to $\mathrm{e}^{-i\omega t}$, imaginary frequencies are linked to the damping of the oscillation, thereby dissipating energy. It has been established for a model Lennard-Jones supercooled liquid that the fraction of unstable modes is directly related to the self-diffusion constant of the system as a function of temperature [52]. Increasing the temperature and the corresponding fluctuations increases the instantaneous deviations of the convex harmonic energy minima, and hence also enhances the fraction of unstable modes.

An example of the appearance of imaginary eigenfrequencies is provided in Fig. 4.4. The plot shows the evolution of the eigenfrequency spectrum of the instantaneous Hessian with increasing the temperature. The spectra belong to a system of polymer chain as described above with the different that the masses of all particles are set to one. In this case, the DOS is computed by ensemble averaging over 5 realisations for each given temperature. We can clearly observe how at the lowest temperature $T = 0.05$ the DOS $\rho(\omega)$ virtually contains no imaginary modes, here plotted on the negative part of the axis. Increasing the temperature towards the glass transition temperature $T = 0.4$ the fraction of the imaginary frequencies drastically increases and appear together with a shift of the main Lennard-Jones peak to lower frequencies.

4.5 Generalised eigenvalue problem and weight functions

In order to set up the non-affine formalism for the multi-component polymer system and to write the corresponding expressions for the complex viscoelastic modulus $G^*(\omega)$, we have to deal with a more generalised situation where not all particles in the system have the same mass. In other words, instead of the simple eigenvalue problem introduced in Chapter 1, we now need to solve the generalised eigenvalue problem

$$\omega_p^2 \mathbf{M} \boldsymbol{u}_p = \mathbf{H} \boldsymbol{u}_p. \tag{4.29}$$

The mass matrix $\mathbf{M}$ is a $N \times N$ block matrix, where each 3×3 block assigns the mass m_i to the particle with label i. We transform this equation by multiplying with $\mathbf{M}^{-1/2}$ from the left, which gives

$$\omega_p^2 \mathbf{M}^{1/2} \boldsymbol{u}_p = \mathbf{M}^{-1/2} \mathbf{H} \boldsymbol{u}_p \tag{4.30}$$

and by inserting $\mathbb{1} = \mathbf{M}^{-1/2}\mathbf{M}^{1/2}$ on the right hand side this becomes

$$\omega_p^2 \widetilde{\boldsymbol{u}}_p = \widetilde{\mathbf{H}} \widetilde{\boldsymbol{u}}_p \tag{4.31}$$

where we have defined $\widetilde{H} = \mathbf{M}^{-1/2}\mathbf{H}\mathbf{M}^{-1/2}$ and $\widetilde{\boldsymbol{u}}_p = \mathbf{M}^{1/2}\boldsymbol{u}_p$. A natural question to ask at this point is whether we can compute physical quantities of the multi-component system in a way so that we can identify the contributions from the different mass species. For this purpose it is very useful to introduce the eigenvector weight functions of different mass types. We will use them to express and compute the partial density of states

(pDOS) and they will reappear later in this chapter when we compute the viscoelastic response of the heteropolymer to an external oscillatory shear strain.

To better understand how the eigenvector weight functions arise it is a good idea to consider the definition of the local density of states. Starting from the standard definition of the eigenvalue distribution $\rho(\lambda) = 1/(3N)\sum_p \delta(\lambda - \lambda_p)$. Assuming that we have some complete set of orthonormal eigenvectors $\{|\boldsymbol{p}\rangle\}$, i.e. $\langle \boldsymbol{p}\,|\boldsymbol{q}\rangle = \delta_{p,q}$ we can write the eigenvalue distribution as

$$\begin{aligned}\rho(\lambda) =& \frac{1}{3N}\sum_{p}\langle \boldsymbol{p}\,|\boldsymbol{p}\rangle\,\delta(\lambda-\lambda_p)\\ =& \frac{1}{3N}\sum_{p,i}\langle \boldsymbol{p}\,|\boldsymbol{i}\rangle\langle \boldsymbol{i}|\,\boldsymbol{p}\rangle\delta(\lambda-\lambda_p)\end{aligned} \tag{4.32}$$

where in the last step we have projected the eigenvectors of the particle basis using the projector $\mathbb{1} = |\boldsymbol{i}\rangle\langle\boldsymbol{i}|$. Thus, $\langle \boldsymbol{p}\,|\boldsymbol{i}\rangle\langle\boldsymbol{i}|\,\boldsymbol{p}\rangle = |\boldsymbol{p}_i^2|$, the projection of the eigenvector onto the particle coordinate $\boldsymbol{i}$ provides the proportionality factor of the contribution of the vibrational motion of the i^{th} degree of freedom to the full vibrational density of states. Collecting the particles which belong to a certain mass species would then provide us with a weight function which informs us about the mass-resolved contributions to the vDOS. However, in our current setting, we cannot straightforwardly apply this since the generalised eigenvectors $\boldsymbol{u}_p$ are orthogonal with respect to the mass-weighted scalar product, i.e. $\langle \boldsymbol{u}_p|\,\mathbf{M}\,|\boldsymbol{u}_q\rangle = \delta_{p,q}$. To define the generalised eigenvector weight function correctly, let us first introduce an index set $\mathcal{M}_n$ for each mass type. This means the set $\mathcal{M}_n$ denotes the set of labels of the particles with mass type n. Considering the norm of generalised eigenvector $\boldsymbol{u}_p$ and expressing in terms of the eigenvectors $\widetilde{\boldsymbol{u}}_p$ we get

$$\begin{aligned}\langle \boldsymbol{u}_p|\,\boldsymbol{u}_p\rangle =& \sum_i \langle \boldsymbol{u}_p\,|\boldsymbol{i}\rangle\langle\boldsymbol{i}|\,\boldsymbol{u}_p\rangle = \sum_i \langle\widetilde{\boldsymbol{u}}_p|\mathbf{M}^{-1/2}\,|\boldsymbol{i}\rangle\langle\boldsymbol{i}|\,\mathbf{M}^{-1/2}|\widetilde{\boldsymbol{u}}_p\rangle\\ =& \sum_i \frac{1}{m_i}\,|\langle\widetilde{\boldsymbol{u}}_p|\,\boldsymbol{i}\rangle|^2\end{aligned} \tag{4.33}$$

where $\langle\widetilde{\boldsymbol{u}}_p|\,\boldsymbol{i}\rangle = \widetilde{\boldsymbol{u}}_{p,i}$ represent the i^{th} component of the eigenvector $\widetilde{\boldsymbol{u}}_p$. This means in order to define the correct weight function in terms of the generalised eigenvectors we need to normalise the contributions $\langle \boldsymbol{u}_p\,|\boldsymbol{i}\rangle\langle\boldsymbol{i}|\,\boldsymbol{u}_p\rangle$ with $\langle \boldsymbol{u}_p|\,\boldsymbol{u}_p\rangle$. This is best seen by using the projections $\mathbb{1} = \sum_n \mathbf{P}_n$, which project on the vector components which belong to the different mass species given by the index set $\mathcal{M}_n$. Consequently, Eq. (4.33) can

be written as

$$\sum_n \langle \boldsymbol{u}_p | \mathbf{P}_n | \boldsymbol{u}_p \rangle = \sum_n \frac{1}{m_n} \langle \widetilde{\boldsymbol{u}}_p | \mathbf{P}_n | \widetilde{\boldsymbol{u}}_p \rangle. \tag{4.34}$$

This means that the correct weight function of, for example, mass species 1 is defined by

$$\chi_1(\omega) = \frac{\langle \boldsymbol{u}_p | \mathbf{P}_1 | \boldsymbol{u}_p \rangle}{\langle \boldsymbol{u}_p | \, \boldsymbol{u}_p \rangle} = \frac{\frac{1}{m_1} \langle \widetilde{\boldsymbol{u}}_p | \mathbf{P}_1 | \widetilde{\boldsymbol{u}}_p \rangle}{\sum_n \frac{1}{m_n} \langle \widetilde{\boldsymbol{u}}_p | \mathbf{P}_n | \widetilde{\boldsymbol{u}}_p \rangle}. \tag{4.35}$$

These considerations are summarised by the constituting relation of the generalised frequency-dependent weight functions of mass type n given by

$$1 = \sum_n \sum_{i \in \mathcal{M}_n} \frac{\left\| \boldsymbol{u}_{p,i}(\omega_p) \right\|^2}{\left\| \boldsymbol{u}_p(\omega_p) \right\|^2} = \sum_n \chi_n(\omega). \tag{4.36}$$

It is now possible to insert this unity in front of the δ-function in the expression of the DOS, and hence obtain a resolution of the DOS into different mass contributions. In this sense, the partial density of states (pDOS) of mass type n takes the form

$$\rho_n(\omega) = \chi_n(\omega)\rho(\omega) = \frac{1}{3N} \sum_{p=1}^{3N} \chi_n(\omega) \delta(\omega - \omega_p). \tag{4.37}$$

4.6 Viscoelastic response in the multi-component system

We have already seen in Chapter 1 how to compute the linear viscoelastic response of a disordered system to an oscillatory shear strain from non-affine lattice dynamics. We will now extend this framework to the case of multi-component systems. The starting point again is the equation of motion

$$\mathbf{M}\ddot{\boldsymbol{r}}(t) + \mathbf{C}\dot{\boldsymbol{r}}(t) + \mathbf{H}\boldsymbol{r}(t) = \boldsymbol{f}(t) \tag{4.38}$$

where in this case $\ddot{\boldsymbol{r}}$ represents the full configuration of the a system, i.e. it is a $3N$ vector. It is possible to rewrite the generalised eigenvalue problem given in Eq. (4.29) in matrix form by introducing the matrix $\boldsymbol{\Phi}$, which has the eigenvectors appearing in Eq. (4.29) as columns. The generalised eigenvalue problem can then be expressed in

terms of the relations

$$\begin{aligned} \mathbf{\Phi}^T \mathbf{M} \mathbf{\Phi} &= \mathbb{1} \\ \mathbf{\Phi}^T \mathbf{H} \mathbf{\Phi} &= \mathbf{\Omega}^2 \end{aligned} \tag{4.39}$$

where we have defined the eigenfrequency matrix $\mathbf{\Omega} = \mathrm{diag}(\omega_1, \ldots, \omega_{3N})$. In order to solve this equation we now resort to a coordinate transformation [90]. This means we set $\boldsymbol{r} = \mathbf{\Phi} \boldsymbol{q}$ and multiply Eq. (4.38) from the left with $\mathbf{\Phi}^T$ to obtain

$$\mathbf{\Phi}^T \mathbf{M} \mathbf{\Phi} \ddot{\boldsymbol{q}} + \mathbf{\Phi}^T \mathbf{C} \mathbf{\Phi} \dot{\boldsymbol{q}} + \mathbf{\Phi}^T \mathbf{H} \mathbf{\Phi} \boldsymbol{q} = \boldsymbol{g} \tag{4.40}$$

with $\boldsymbol{g} = \mathbf{\Phi}^T \boldsymbol{f}$ being the generalised driving force. We see that the first and third term are taken care of by virtue of the orthogonality relations Eq. (4.29), which constitute the generalised eigenvalue problem, yielding

$$\ddot{\boldsymbol{q}} + \mathbf{\Phi}^T \mathbf{C} \mathbf{\Phi} \dot{\boldsymbol{q}} + \mathbf{\Omega}^2 \boldsymbol{q} = \boldsymbol{g}. \tag{4.41}$$

In this form the system of equations is not decoupled because the open question remains how to proceed with the second term involving the matrix product $\mathbf{\Phi}^T \mathbf{C} \mathbf{\Phi}$. In general, we cannot find a solution of the coupled system, so at this point of the analysis we need to work with the assumption that $\mathbf{\Phi}^T \mathbf{C} \mathbf{\Phi}$ is a diagonal matrix. In physical terms, this assumption reflects the idea that the damping is not correlated across different eigenmodes. A standard approach is to assume mass-proportional damping $\mathbf{C} \propto \mathbf{M}$, which automatically decouples the equations of motion [90]. As we will see later this situation is relevant for the comparison of the viscoelastic response with molecular dynamics simulations. Alternatively, it would also be an option to approximate the full friction matrix $\mathbf{C}$ with a diagonal matrix and check under which conditions the off-diagonal elements are small enough. For now, continuing with $d_k = (\mathbf{\Phi}^T \mathbf{C} \mathbf{\Phi})_{kk}$ we can express Eq. (4.41) in its decoupled form as

$$\ddot{q}_k + d_k \dot{q}_k + \omega_k^2 q_k = g_k. \tag{4.42}$$

Using a Fourier transform to map the equation to frequency-space, we arrive at

$$\widetilde{q}_k = \frac{\widetilde{g}_k}{-\omega^2 + i\omega d_k + \omega_k^2}, \tag{4.43}$$

where $\widetilde{\boldsymbol{r}} = \boldsymbol{\Phi}\widetilde{\boldsymbol{q}}$. It has been established in Chapter 1 that the stress response of the system to a strain η is related to the displacement fields $\boldsymbol{r}$ via

$$\Delta\widetilde{t}_\eta(\omega) = G_\mathrm{A}\widetilde{\eta}(\omega) - \frac{1}{V}\sum_{i=1}^{N}\boldsymbol{\Xi}_i^T\cdot\widetilde{\boldsymbol{r}}_i \tag{4.44}$$

where the summation extends over all particles and the vectors $\boldsymbol{\Xi}$ and $\widetilde{\boldsymbol{r}}$ are the $3N$-dimensional affine force and displacement field, respectively, as a function of the driving frequency ω.

Making use of the same basis transformation as above we can substitute the expression Eq. (4.43) into second term of Eq. (4.44), i.e.

$$\begin{aligned}\frac{1}{V}\sum_{i=1}^{N}\boldsymbol{\Xi}_i\cdot\widetilde{\boldsymbol{r}}_i =& \frac{1}{V}\sum_{i=1}^{N}\boldsymbol{\Xi}_i^T\cdot\left(\sum_p\boldsymbol{\Phi}_{ip}\widetilde{\boldsymbol{q}}_p\right)\\ =& \frac{1}{V}\sum_i\sum_p\boldsymbol{\Xi}_i^T\boldsymbol{\Phi}_{ip}\frac{\widetilde{\boldsymbol{g}}_p}{-\omega^2+i\omega d_p+\omega_p^2}.\end{aligned} \tag{4.45}$$

In frequency space the generalised force vector is given as $\widetilde{\boldsymbol{g}}_p = \sum_j\boldsymbol{\Phi}_{pj}^T\widetilde{\boldsymbol{f}}_j$. Since the driving force is defined as $\boldsymbol{f}(t) = \boldsymbol{\Xi}\,\widetilde{\eta}\sin\omega t$, we continue the above expression with

$$\begin{aligned}\frac{1}{V}\sum_{i=1}^{N}\boldsymbol{\Xi}_i^T\cdot\widetilde{\boldsymbol{r}}_i =& \frac{1}{V}\sum_{i,j}\sum_p\frac{\boldsymbol{\Xi}_i^T\boldsymbol{\Phi}_{ip}\boldsymbol{\Phi}_{pj}^T\boldsymbol{\Xi}_j}{-\omega^2+i\omega d_p+\omega_p^2}\widetilde{\eta}(\omega)\\ =& \frac{1}{V}\sum_{i,j}\sum_p\frac{\left(\boldsymbol{\Phi}_{pi}^T\boldsymbol{\Xi}_i\right)^T\cdot\left(\boldsymbol{\Phi}_{pj}^T\boldsymbol{\Xi}_j\right)}{-\omega^2+i\omega d_p+\omega_p^2}\widetilde{\eta}(\omega).\end{aligned} \tag{4.46}$$

The matrix product defined via $\widehat{\boldsymbol{\Xi}}_p = \sum_i\boldsymbol{\Phi}_{pi}^T\boldsymbol{\Xi}_i$ and its transposed counterpart represent the basis transformation of the affine force field into the generalised eigenbasis. Eventually, this allows us to write Eq. (4.44) as

$$\Delta\widetilde{t}_\eta(\omega) = G_\mathrm{A}\widetilde{\eta}(\omega) - \frac{1}{V}\sum_p\frac{\boldsymbol{\Xi}_p^T\cdot\boldsymbol{\Xi}_p}{-\omega^2+i\omega d_p+\omega_p^2}\widetilde{\eta}(\omega). \tag{4.47}$$

This is the final result and describes the complex viscoelastic shear modulus in the setting of the generalised eigenvalue problem of a multi-component disordered system through $\Delta\widetilde{t}_\eta(\omega) = G^*(\omega)\widetilde{\eta}(\omega)$ in the linear regime.

4.7 The KPM in the multi-component setting

The essential tool for extracting the contribution to the vibrational density of states and the non-affine correlator originating from different mass contributions are the weight function $\chi_n(\omega)$. In order to treat $\chi_n(\omega)$ with the kernel polynomial approximation we have to slightly alter the scheme which we have used before for the single-mass density of states.

Conceptually, in the current setting the starting point for the KPM always involves summations over δ-peaks. In the case of the quantities $\chi_n(\omega)$ and $\Gamma(\omega)$ the sum contains an additional weighting factor depending on the eigenvector in order to expand and approximate the desired function. This means that to the end of treating $\chi_n(\omega)$ with the KPM we start from the basic expression for the DOS, i.e.

$$\rho(\omega) = \frac{1}{3N} \sum_{p=1}^{3N} \delta(\omega - \omega_p), \tag{4.48}$$

and subsequently insert the normalised weight specified in Eq. (4.35) in front of $\delta(\omega - \omega_p)$. The weight in question consists of the two parts $\langle \boldsymbol{u}_p | \mathbf{P}_n | \boldsymbol{u}_p \rangle$ and $\langle \boldsymbol{u}_p | \, \boldsymbol{u}_p \rangle$ for the numerator and the denominator of $\chi_n(\omega)$, respectively. Starting with $\langle \boldsymbol{u}_p | \mathbf{P}_n | \boldsymbol{u}_p \rangle$, the function resulting from the KPM is an approximation to this factor multiplied by some distribution. Since we want to compute the bare weight function $\chi_n(\omega)$, we need to divide this by the KPM approximation for $\langle \boldsymbol{u}_p | \mathbf{P}_n | \boldsymbol{u}_p \rangle$, such that the correct normalisation is guaranteed and that we obtain the bare weight function $\chi_n(\omega)$.

To implement this idea we start with the numerator in Eq. (4.35) and define the auxiliary function $\widetilde{\chi}_n(\omega)$

$$\widetilde{\chi}_n(\omega) = \frac{1}{3N} \sum_{p=1}^{3N} \sum_{i \in \mathcal{M}_n} \langle \boldsymbol{u}_p \, | \boldsymbol{i} \rangle \langle \boldsymbol{i} | \, \boldsymbol{u}_p \rangle \delta(\omega - \omega_p), \tag{4.49}$$

which in this form is amenable to the expansion in terms of Chebyshev polynomials. Carrying out the analogous steps as for the single-mass density of states above, we now map the support of the eigenvalue spectrum of the generalised eigenvalue problem onto the interval $[0, 1]$ and continue with

$$\widetilde{\chi}_n(\omega) = \frac{4\omega}{3\pi N} \frac{2 - \varepsilon}{\lambda_{\max} - \lambda_{\min}} \sum_{k=0}^{\infty} \mu_k \sin\Big[(k+1) \arccos \widetilde{\lambda}\Big], \tag{4.50}$$

where the corresponding Chebyshev moments are now written as

$$\mu_k = \frac{1}{3N} \sum_p \sum_{i \in \mathcal{M}_n} \langle \boldsymbol{u}_p \, | \boldsymbol{i} \rangle \langle \boldsymbol{i} | \, \boldsymbol{u}_p \rangle U_k(\widetilde{\lambda}_p). \tag{4.51}$$

To pull the polynomials $U_k(\widetilde{\lambda}_p)$ inside of the scalar product we now have to be cautious since we are dealing with generalised eigenvectors. By virtue of the fact that in the above expression only the eigenvector components of the mass species n are projected out it is possible to write the term $\langle \boldsymbol{u}_p \, | \boldsymbol{i} \rangle \langle \boldsymbol{i} | \, \boldsymbol{u}_p \rangle$ appearing in the above summation as $\frac{1}{m_n} \langle \widetilde{\boldsymbol{u}}_p \, | \boldsymbol{i} \rangle \langle \boldsymbol{i} | \, \widetilde{\boldsymbol{u}}_p \rangle$ because the vectors $\boldsymbol{i}$ are eigenvectors of the mass matrix $\mathbf{M}$ with eigenvalue m_n. As a consequence we can make use of the relation $U_k(\widetilde{\lambda}_p) \, | \widetilde{\boldsymbol{u}}_p \rangle = U_k(\widetilde{\mathbf{H}}) \, | \widetilde{\boldsymbol{u}}_p \rangle$ and continue with

$$\mu_k = \frac{1}{3N} \sum_p \sum_{i \in \mathcal{M}_n} \langle \boldsymbol{u}_p \, | \boldsymbol{i} \rangle \langle \boldsymbol{i} | \; U_k(\widetilde{\mathbf{H}}) \boldsymbol{u}_p \rangle \tag{4.52}$$

by reabsorbing the factor m_n into the generalised eigenvector. Subsequently, making use of the stochastic evaluation of this trace with the Gaussian random vectors $\boldsymbol{x}_0$, the Chebyshev moment in Eq. (4.51) are approximated by averaging the quantity

$$m_k = \sum_{i \in \mathcal{M}_n} \langle \boldsymbol{x}_0 \, | \boldsymbol{i} \rangle \langle \boldsymbol{i} | \, \boldsymbol{x}_k \rangle = \langle \boldsymbol{x}_0 | \, \mathbf{P}_n \, | \boldsymbol{x}_k \rangle \, , \tag{4.53}$$

where $\mathbf{P}_n$ represents the projector of the particle species n. The approximate Chebyshev moments converge to the actual Chebyshev moments μ_k, i.e. $\langle\!\langle m_k \rangle\!\rangle \to \mu_k$. Due to the fact that random vectors $\boldsymbol{x}_k$ are supposed to represent the generalised eigenvector of the multi-component system, it would be incorrect to use normalised Gaussian random vector as before. To achieve the correct stochastic approximation of the Chebyshev moments μ_k we multiply a normalised random vector $\boldsymbol{\xi}_0$ with inverse square root of the mass matrix $\mathbf{M}$. As a result the initial random seed of the KPM algorithm in this case is the random vector $\boldsymbol{x}_0 = \mathbf{M}^{-1/2} \boldsymbol{\xi}_0$. The same reasoning is applicable to the denominator of Eq. (4.35). The first step again is an auxiliary function given by

$$\chi_{\mathrm{norm}}(\omega) = \frac{1}{3N} \sum_{p=1}^{3N} \langle \boldsymbol{u}_p | \boldsymbol{u}_p \rangle \delta(\omega - \omega_p), \tag{4.54}$$

where we use the subscript to signal that this is the KPM approximation function for the normalisation factor of the weight function $\chi_n(\omega)$. Going through the same steps as

for $\widetilde{\chi}_n(\omega)$, the final result in terms of the associated approximate Chebyshev moment is

$$m_k = \langle \boldsymbol{x}_0 | \boldsymbol{x}_k \rangle, \tag{4.55}$$

which converges to the true Chebyshev moments appearing the in expansion of $\chi_{\text{norm}}(\omega)$

$$\mu_k = \frac{1}{3N} \sum_p \langle \boldsymbol{u}_p | U_k(\widetilde{\mathbf{H}}) \boldsymbol{u}_p \rangle \tag{4.56}$$

in the statistical average as $\langle\!\langle m_k \rangle\!\rangle \to \mu_k$. Having set up the KPM approximation for these two ingredients we subsequently obtain the weight functions $\chi_n(\omega)$ as the quotient of the two converged auxiliary functions. i.e.

$$\chi_n(\omega) = \frac{\widetilde{\chi}_n(\omega)}{\chi_{\text{norm}}(\omega)} \tag{4.57}$$

which is defined on the support of the eigenvalue spectrum of the Hessian matrix with the condition that $\chi_{\text{norm}}(\omega) \neq 0$.

4.7.1 Results and comparison with KPM

The system under investigation in this section is probed at the temperature $T = 0.05$, that is in a temperature regime well below the glass transition, which is at $T = 0.40$ for our system. We have chosen this regime to avoid complications from high temperature effects, so to say as a proving ground for the multi-component non-affine formalism in combination with the simulation snapshot as an input configuration. In recent work, however, it has been established for a single-mass polymer system that the combination of an instantaneous normal mode analysis together with the non-affine formalism is capable of producing a very good match with viscoelastic response data obtained from simulation [91].

For the eigenanalysis via direct diagonalisation a system consisting of $N = 5000$ particles was generated using LAMMPS. The resulting configuration was then used to construct the Hessian matrix for this specific snapshot. The analysis using the KPM was done on a system with the same parameters but of significantly larger in size of $N = 50000$ particles. We have checked that the results for the viscoelastic response of the system obtained with the KPM from the small and large system give similar results provided that the Chebyshev algorithm is sufficiently converged. Clearly, there will be slight variations in the vDOS and $\Gamma(\omega)$ due to the fact that different snapshots of the melt are considered. It is in any case beneficial to use the larger system size for the KPM,

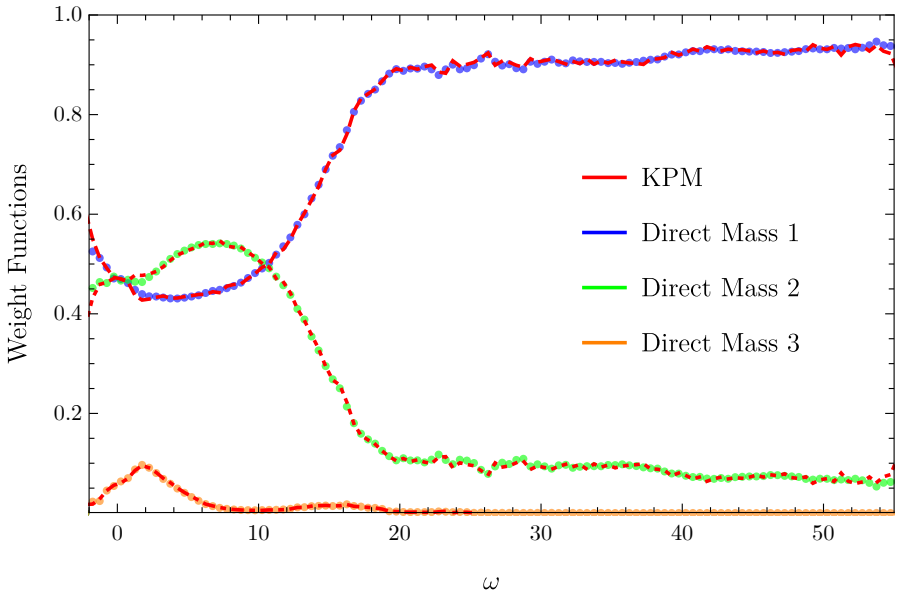

Fig. 4.5 Here we show the weight function of the three mass contributions for $T = 0.05$ as defined in Eq. (4.36). The coloured points show the data obtained from direct diagonalisation for the three weight functions $\chi_n(\omega)$, $n = 1, 2, 3$. The dotted, dashed, and dash-dotted red lines show the approximation to the weight function using the KPM.

since it ensures a better convergence rate. In addition, the fidelity of the approximation will be provided down to lower frequencies due to the larger system size. We now proceed to the discussion of the results with the eigenfrequency spectrum $\rho(\omega)$ and non-affine correlator $\Gamma(\omega)$ obtained both from direct diagonalisation and KPM.

The weight functions $\chi_n(\omega)$ plotted in Fig. 4.5 are the central result of this section. For a given mass species they represent the contribution from that species to the full eigenvector of the system at a given eigenfrequency. First, we notice that the KPM is capable of producing a very accurate approximation for $\chi_n(\omega)$. It should be noted however that the polynomial degree necessary for a good match with the weight functions computed with direct diagonalisation around $\omega = 0$ is comparatively high. The reason for this is that close to $\omega = 0$ the eigenfrequency distribution rapidly drops to zero, which means that there are only a few modes present in the vicinity of $\omega = 0$. In the KPM, the δ-peaks which constitute the spectrum $\rho(\omega)$ are approximated by a distribution of finite-width [5]. The resolution capability of the approximation is set by the maximum degree of the Chebyshev polynomials used in the truncated series expansion of $\rho(\omega)$. Hence, in order to correctly account for the placement and relative frequency of the very low-lying eigenfrequencies a high-degree polynomials are required.

We specified earlier that a polynomial degree of $K = 300$ was sufficient to produce a good approximation for the depleted fcc crystal. Now the a polynomial degree of around 3000 is required to also capture the extremely low eigenmodes. Nevertheless, the convergence is achieved with only a few averaging iterations using the sampling from Gaussian random vectors.

We can observe in Fig. 4.5 that at zero frequency the contributions from mass m_1 and m_2, are equal, i.e. $\chi_1(0) = \chi_2(0) = 0.47$. This value reflects the fraction of particles of different masses in the polymer chains. These values can physically be understood in the sense that the zero-frequency mode reflects a global translation of the system. The contribution to the corresponding zero-frequency eigenvector therefore has to be equal for every single particle, since this global zero-frequency displacement is independent of the mass of the particle. This leads to the zero-frequency eigenvector $\boldsymbol{u}(\omega_p = 0)$ reflecting the relative frequencies of the members of the different mass species [87].

The weight function of particles of mass species 3, $\chi_3(\omega)$ has significant contribution only at relatively low frequencies. This is an expected behaviour, because mass 3 particles, being the heaviest and least frequent particles in the polymer chain, cannot participate significantly in vibrational motions of high frequency due their relatively high inertia. At low frequencies the weight functions of mass 1 and 2 yield about the same contribution, and cross over at a frequency which roughly corresponds to the to the first large Lennard-Jones peak of the vDOS. Going to higher frequencies the weight function of mass 1, $\chi_1(\omega)$, increases and saturates, giving the majority of the vibrational weight function at the largest frequency available in the system. In the high-frequency limit, we observe that most of the contribution to the overall weight function comes from the lightest particles of species 1.

From the knowledge of the weight functions $\chi_n(\omega)$ we can straightforwardly compute the partial densities of states for each mass species by using Eq. (4.37). The comparison of the results for the pDOS obtained from direct diagonalisation and KPM for our system at $T = 0.05$ are shown in Figs. 4.6 (b)-(d). The full vDOS depicted in panel (a) of the same Figure perfectly matches with the results obtained from direct diagonalisation. Note that the fluctuations in the double peak at high-frequency are markedly lower in the case of the KPM result since they were computed from the much larger polymer system consisting of $N = 50000$ particles. In addition to the large Lennard-Jones peak at low-frequencies we notice that in comparison to the shape of the vDOS of the single-mass polymer system in Fig. 4.4, the high-frequency FENE peak has split into two subpeaks. In Fig. 4.7 we show how the three partial densities of states contribute in relation to the full vDOS. It is interesting to observe that this double peak is comprised almost

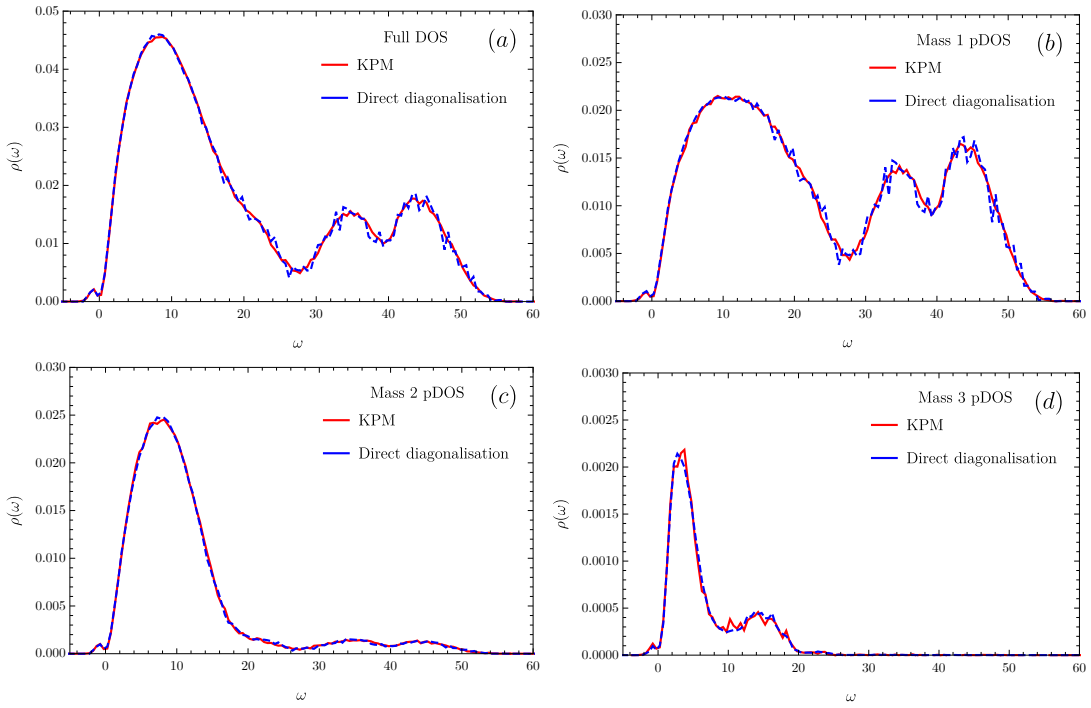

Fig. 4.6 This Figure shows the full vDOS of the $T = 0.05$ three-mass polymer glass together with the three partial DOS contributions from the three masses $m_1 = 1$, $m_2 = 3$ and $m_3 = 10$. Note the scale difference of the pDOS for mass 3.

exclusively of modes from the lightest mass $m_1 = 1$, likely representing fast oscillations of the m_1 with respect to the three times heavier m_2, which due to their interaction remain relatively immobile. To check this assertion an analysis of the vibrational modes along the corresponding eigenvector direction would be necessary.

Achieving convergence for the non-affine correlator $\Gamma(\omega)$ with the kernel polynomial method is much more problematic than for the DOS. The cause for this difficulty stems from the fact that the random vector used in the approximation of the Chebyshev moments μ_k is projected on the affine force field vector, which itself is an inherently random quantity due to the structural disorder of the polymer configuration. As a consequence, larger fluctuations occur which need more iterations to be smoothed out. To achieve a good approximation using the KPM for the vDOS $\rho(\omega)$, usually between 10-100 averaging iterations are required. In case of the non-affine correlator $\Gamma(\omega)$, between 10^3 to 10^4 iterations are needed to converge the algorithm to a reasonable degree, depending also on the desired resolution. We show the results obtained for the multi-component non-affine correlator in Fig. 4.8. Both the correlator $\Gamma(\omega)$ itself and the product with the vDOS, $\Gamma(\omega)\rho(\omega)$, which is the direct output of the KPM algorithm, are shown. Again the agreement between the method of direct diagonlisation and KPM is

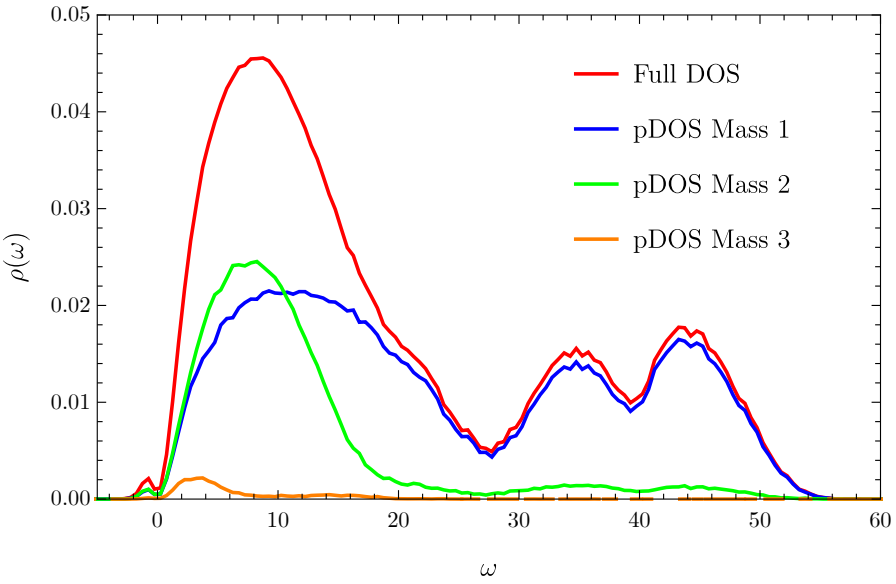

Fig. 4.7 The full KPM vDOS in terms of the three pDOS contributions.

excellent. As noted above, the non-affine correlator is a comparatively noisy quantity. We should therefore bear in mind that in this section only one realisation of the polymer system is considered. Employing ensemble averaging over many realisation, however, it is expected that $\Gamma(\omega)$ is self-averaging and converges to its thermodynamic limiting distribution [57].

4.7.2 The viscoelastic response of the multi-component polymer

The final goal of the current approach is to develop a theoretical framework to allow for the numerical computation of the linear viscoelastic response for disordered systems consisting of different mass species. In particular, we desired to modify the kernel polynomial method such that it allows us to approximate the complex modulus $G^*(\omega)$ for systems which are to large to be amenable for a treatment using direct diagonalisation.

Having discussed the weight function $\chi_n(\omega)$, the partial densities of states and the non-affine frequency correlator $\Gamma(\omega)$, we are now in the position to test the non-affine formalism for the heteropolymer in terms of its ability to produce correct predictions of the linear viscoelastic response when compare to the results obtained directly from the molecular dynamics simulation. These simulation results serve as a benchmark for complex shear modulus $G^*(\omega) = G'(\omega) + G''(\omega)$ computed from the non-affine theory. This is done by applying a small amplitude simple oscillatory shear strain to the simulation

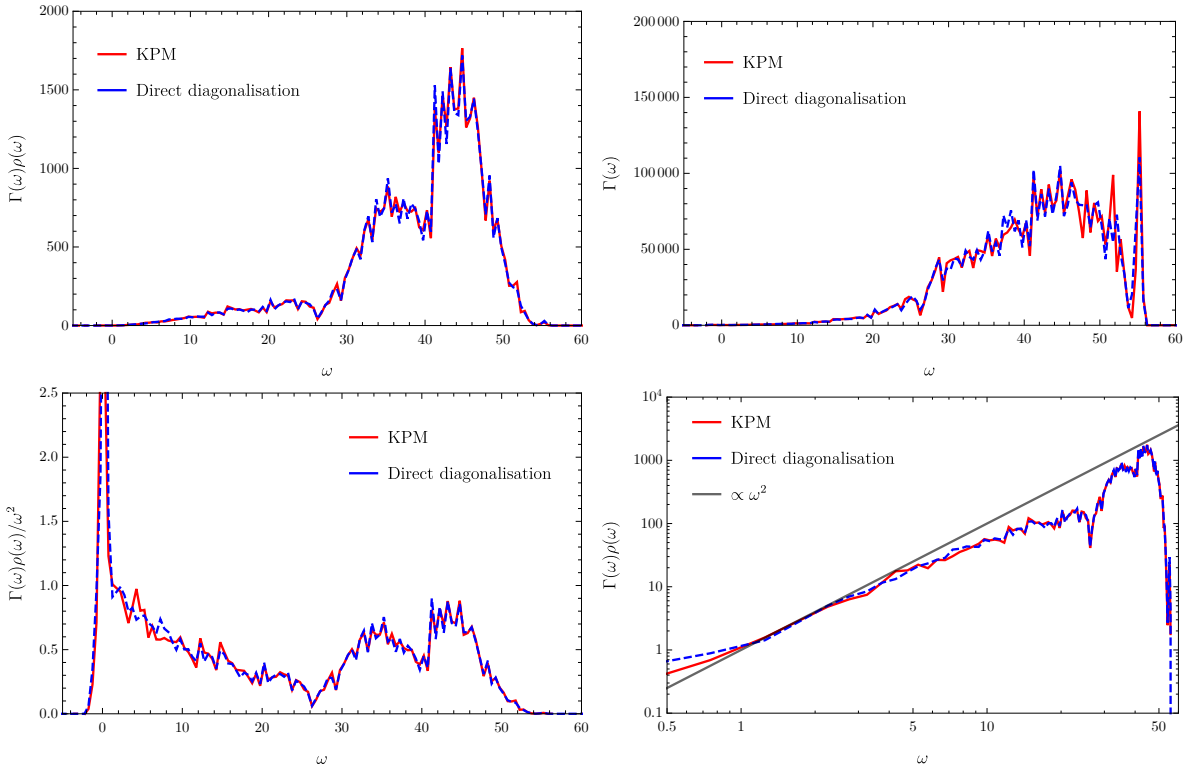

Fig. 4.8 Comparison of results from direct diagonalisation and KPM. The upper left panel shows the product of the DOS $\rho(\omega)$ and the non-affine correlator $\Gamma(\omega)$. The lower left panel shows the rescaled product $\Gamma(\omega)\rho(\omega)/\omega^2$. The upper right panel shows the non-affine correlator $\Gamma(\omega)$ in a log-linear. The lower right panel shows $\Gamma(\omega)\rho(\omega)$ in the log-linear scale with a ω^2-scaling as reference.

box and subsequently recording the stress vs. strain curves. The oscillatory strain is given by $\eta(\omega) = \tilde{\eta}\sin(\omega t)$ and the resulting stress is $\sigma = \sigma_0 \sin(\omega t + \delta)$, where as introduce above, ω represent the driving frequency of the oscillatory shear strain and δ is the phase lag between stress and strain. The complex modulus is then given in terms of the phase lag δ as [91]

$$G' = \frac{\eta_0}{\sigma_0}\cos\delta, \qquad G'' = \frac{\eta_0}{\sigma_0}\sin\delta. \tag{4.58}$$

The computation of the complex modulus from the simulation were carried out by Vladimir Palyulin. The results for the simulated mechanical spectroscopy and the results obtained from direct diagonalisation and KPM are shown in Fig. 4.9.

Firstly, it can be observed that the match between direct diagonalisation and KPM is very good for both the storage and loss modulus, $G'(\omega)$ and $G''(\omega)$, respectively. The only significant deviation occurs below $\omega = 0.10$. This can be attributed to the fact that

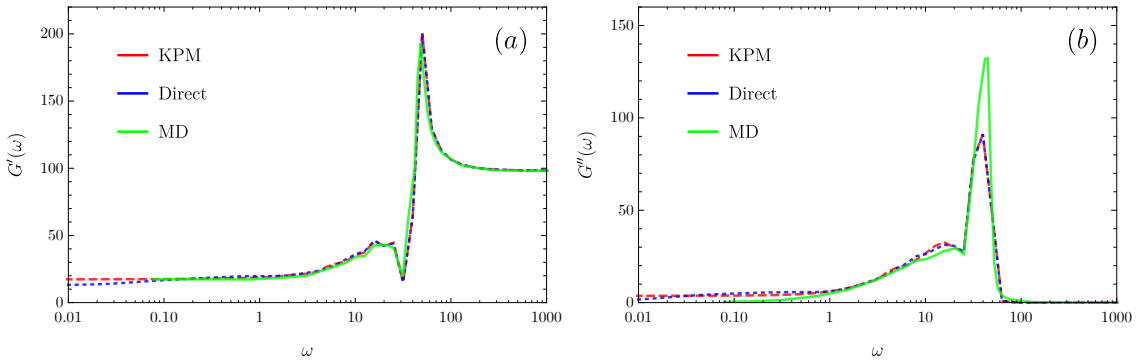

Fig. 4.9 The complex viscoelastic modulus $G(\omega) = G'(\omega) + iG''(\omega)$. Comparison between results obtained via the KPM, direct diagonalisation and molecular dynamics simulations at $T = 0.05$.

the KPM results were obtained for a much larger system relative to direct diagonalisation which minimises finite size effects and allows for a higher accuracy at lower frequencies. In the frequency range below $\omega = 0.10$ there is no data available from the MD simulations. Comparing the theoretical results with the simulations, we can observe that the theory reproduces the MD results for $G'(\omega)$ very accurately throughout the entire frequency range, as shown in Fig. 4.9(a). However, considering the behaviour of the loss modulus $G''(\omega)$ in Fig. 4.9(b), it is evident that the theoretical description deviates from the simulation results, most clearly around the main relaxation peak at $\omega \approx 38$ which is possibly rooted in the approximations inherent to the theoretical approach. We have seen that the combined approach using non-affine lattice dynamics and the KPM to compute the linear viscoelastic response is based on the harmonic approximation of the interaction potentials and the assumption of quasi-static shear strain. Clearly, these assumptions will not be reflected by the simulation, to a varying degree depending on the temperature of the system the frequency of the oscillatory shear under consideration. Even though the data shown in Fig. 4.9 was obtained at a relatively low temperature, there will be temperature-dependent, anharmonic contributions, which are not described by the theoretical model due to its harmonic nature. In particular, this will become evident at low frequencies and high temperatures. Increasing the temperature has the consequence that the system is prone to large-scale plastic rearrangements corresponding to the low-frequency part in the viscoelastic spectrum. These plastic events which eventually result in viscous flow are capture by the simulation but not the theoretical description. As a consequence, is can be expected that the accuracy of the theory deteriorates with increasing temperature in particular in the low-frequency regime and this will be particularly visible in the behaviour if the loss modulus $G''(\omega)$ which reflects

the dissipation mechanism. On the other hand, it can be expected that the high-frequency limit of $G^*(\omega)$ is accurately described the present framework. The reason for this is that even at higher temperatures closer to the melting transition, high-frequency oscillatory excitations do not explore the anharmonic region of the interaction potential. More investigations will be needed to figure out precisely the cause for the deviations, for example, by systematically investigating the contribution to the full viscoelastic moduli which come from non-affine displacement event with large amplitudes, in particular those which are linked to eigenmodes in the negative part of the spectrum to explore the energy dissipation mechanism. In view of this, it can be concluded that the KPM can be valuable to amend finite system size effects and therefore to obtain results even at very low frequencies.

Despite its limitations, this approach promises to be useful not only for resolving the different contributions from different mass species to the overall linear viscoelastic response, but should have further applications. Instead of working with projections of the eigenvectors to obtain contributions from different mass species, we could analyse the contribution of vibrational modes in terms of their directionality. For example, in the polymer melt the obvious choice would be to separate the vibrational motion into contribution which go along and perpendicular to the direction of the polymer chain.

Chapter 5

Linking the interatomic repulsion strength to the viscoelasticity of metallic glasses

5.1 Introduction

Understanding the mechanism which governs the emergence of mechanical stability at the glass transition of supercooled metallic liquids [70] calls for deeper insights into the connection between the fragility index, which quantifies how rapidly the viscosity varies at the onset of the transition, and the interatomic interaction. As previous work suggested [7, 43] mechanical stability in amorphous solids is crucially linked to the repulsive part of the interatomic interaction potential. For example, it was possible to find a concrete link between the interaction properties and the viscosity for repulsively interacting colloidal suspensions [65]. By increasing the concentration of colloidal particles in the suspension to a critical value, the system undergoes a glass transition at which point the viscosity of the suspension increases by several orders of magnitudes. Using colloids of varying softness, the experiments in Ref. [65] showed that the rise of viscosity at the glass transition is more drastic the harder the colloids are, i.e. the more repulsive the interaction between particles is. Put differently, decreasing the softness of the colloidal particles, the suspension transitions from a strong to a fragile glass former.

However, no consensus has been reached on whether for different types of glass formers, i.e. colloidal, molecular, and metallic, the interatomic repulsion softness generally correlates with strong glasses [65] or with fragile glasses [81]. The question therefore is whether for metallic glass-forming liquids it is possible to find a principle similar to the

one established for colloidal suspensions connecting the repulsive interaction between the microscopic constituents and the resulting behaviour of the viscosity. In this chapter, we derive an analytical closed-form relation between the fragility index of metallic glass formers and the short-ranged repulsive part of the interatomic interaction given by pseudopotential theory. This fundamental relation is obtained from a one-parameter theory fit to experimental rheological data of supercooled metallic melts. Resorting to this combination of theory and experiments, it is established that interatomic repulsion softness in metals goes along with strong glasses and low fragility. Surprisingly, given the difference in energy scale of many orders of magnitude and the nature of the microscopic interaction, this finding is in full agreement with the correlation observed experimentally for soft colloidal glasses by Mattsson, Weitz and co-workers [65].

Finally, we establish a quantitative link between our analysis and the theory of shear transformation zones to estimate the size of the cooperatively rearranging regions in good agreement with the findings in Ref. [59].

5.2 Shear modulus of glasses

The starting point for linking the shear modulus and the atomic connectivity analytically is the theoretical framework of non-affine elastic response [57, 102, 19]. The standard affine approximation of the classical Born-Huang theory is not applicable to amorphous as well as other non-centrosymmetric lattices [2]. This problem arises due to the lack of local inversion symmetry in amorphous solids. As a consequence, the deformation forces which are transmitted to an atom by its bonded neighbours do not balance each other by mirror symmetry. The resulting forces, which act on every atom, are released through additional non-affine motions on top of the standard affine displacements dictated by the macroscopic strain. In other words, the continuum assumption that the macroscopic deformation scales down to the microscopic lattice does not generally hold for amorphous systems. Structural disorder and non-affine motions can be taken into account using the theory of non-affine elastic response. For an amorphous solid under a shear strain γ, we can express the free energy of deformation as $F(\gamma) = F_{\mathrm{A}}(\gamma) - F_{\mathrm{NA}}(\gamma)$ [100]. The two terms represent the standard affine contribution to the free energy, provided by the framework of Born-Huang lattice dynamics [10, 101], and the non-affine contribution, respectively. Resorting to an eigenfunction decomposition of the non-affine contribution, it is possible to derive an analytic expression for the shear modulus of an amorphous

lattice. As discussed in Chapter 1, the result for the shear modulus is given by

$$G = G_{\mathrm{A}} - G_{\mathrm{NA}} = G_{\mathrm{A}} - \sum_{i,j} \boldsymbol{\Xi}_i^T \, \mathbf{H}_{ij}^{-1} \, \boldsymbol{\Xi}_j, \tag{5.1}$$

where $\mathbf{H}_{ij} = (\partial U/\partial \boldsymbol{r}_i \partial \boldsymbol{r}_j)_{\gamma\to 0}$ represents the standard dynamical matrix of the solid [4], U the internal energy of the system and $\boldsymbol{\Xi}_i$ the affine force field acting on the atoms due to the shear deformation [57]. The expression for the affine shear modulus G_{A}, in the above equation can be obtained in the following way [10, 99]. An expansion of the free energy, where the macroscopic strain is scaled down to the atomic displacements, yields the famous Born-Huang formula for the shear modulus in the harmonic approximation as

$$G_{\mathrm{A}} = \frac{\kappa R_0^2}{V} \sum_{\langle i,j \rangle} n_{ij}^x n_{ij}^y n_{ij}^x n_{ij}^y, \tag{5.2}$$

where κ denotes the spring constant of an harmonic bond, and R_0 the equilibrium lattice constant. The bond-orientation unit vector $\hat{\boldsymbol{n}}_{ij} = (\cos\varphi \sin\theta, \sin\varphi \sin\theta, \cos\theta)$ connects the nearest-neighbour atoms i and j. In a lattice of N atoms every bond contributes a term proportional to the geometric factor $\langle n_{ij}^x n_{ij}^y n_{ij}^x n_{ij}^y \rangle$ to the above lattice sum. This average is to be evaluated for a prescribed angular distribution of the bond orientations [99]. Introducing the average number of mechanical bonds per atom Z (atomic connectivity), the mean-field estimate gives $G_A = (N/2V)\kappa R_0^2 Z \langle n_{ij}^x n_{ij}^y n_{ij}^x n_{ij}^y \rangle$. Assuming an isotropically random distribution of bond orientations, the average over the components of the bond orientation vectors yields the numerical factor 1/15. Thus, we can establish an explicit expression for the affine shear modulus as

$$G_{\mathrm{A}} = \frac{1}{30V} N \kappa R_0^2 Z. \tag{5.3}$$

As shown in Ref. [102], assuming a central-force interaction and introducing the atomic packing fraction $\phi = vN/V$, with v a characteristic rigid-core volume, Eq. (5.1) can be evaluated analytically as

$$G = G_{\mathrm{A}} - G_{\mathrm{NA}} = \frac{1}{5\pi} \frac{\kappa}{R_0} \phi (Z - Z_c). \tag{5.4}$$

The non-affinity of the amorphous solid is encoded in the quantity $-Z_c$, which denotes the critical number of bonds at which the shear modulus vanishes by virtue of the non-affine softening mechanism. This expression still does not include the direct contribution of thermal effects to the elastic response. Thermal vibrations in fact soften the shear

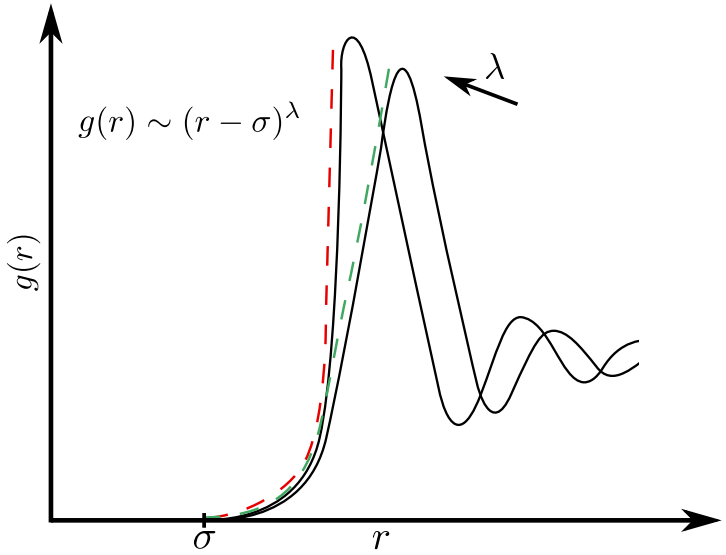

Fig. 5.1 Approximation of the repulsive part of the first peak of $g(r)$ using two different values for the steepness λ. An increase in λ is linked to a steeper slope of $g(r)$.

modulus by an additional negative term $-3(N/V)kT\partial^2(\ln \hbar\omega/kT)/\partial\gamma^2$ [102, 36]. For many materials, including metallic and polymer materials, this contribution is very small compared to the other terms in Eq. (5.4). It determines a decreasing trend of G with T which is negligible compared to the combined effect of non-affinity and thermal expansion [60].

5.3 Modelling the temperature dependence of the shear modulus

The crucial effect which controls the temperature dependence of the shear modulus is the change in atomic connectivity Z due to Debye-Grüneisen thermal expansion [102]. Approaching the glass transition temperature T_g from below, this effect is responsible for the loss of mechanical stability. We will show that the same effect is responsible for the decrease of the high-frequency shear modulus with increasing T in the supercooled liquid above T_g. The atomic packing fraction ϕ is reduced upon increasing the temperature T, an effect mediated by the thermal expansion coefficient defined as $\alpha_T = \frac{1}{V}(\partial V/\partial T) = -\frac{1}{\phi}(\partial\phi/\partial T)$. Integrating this, we see that the atomic packing fraction evolves with T according to $\log(1/\phi) = \alpha_T\, T + c$. For an amorphous metal, a decrease in Z arises if the separation between two particles is larger than the typical length scale of attraction defined by the first minimum of the interatomic pseudopotential $r_{\min}$. For example, if

the separation of an atom from one of its caged nearest-neighbours exceeds $r > r_{\min}$, the neighbour effectively leaves the coordination shell or cage [102], and no longer contributes to the cage elasticity.

When increasing T, the average spacing between atoms in the coordination shell becomes larger, and the probability of nearest neighbours leaving the connectivity shell increases. It is then possible to use the radial distribution function $g(r)$ to relate the change in packing fraction $\delta\phi$, due to an externally imposed change in temperature δT, to the change in connectivity δZ. Following along the lines of Ref. [102], the change of atomic connectivity $\delta Z = Z - Z_c$, relative to the critical stability (isostatic) point Z_c, can be calculated when the density of the system increases by an increment $\delta\phi = \phi - \phi_c$ according to

$$Z - Z_c \sim \int_1^{1+\delta\phi} r^2 g(r)\,\mathrm{d}r, \tag{5.5}$$

where r represents a dimensionless distance defined with respect to the rigid-core diameter σ. Since the radial distribution function $g(r)$ is not known in analytical form for real materials, we introduce an approximation scheme. The basic idea is to represent the repulsive side of the first peak of $g(r)$ by means of the power-law approximation $g(r) \sim (r-\sigma)^{\lambda}$. In this way, the parameter λ characterises the steepness of the left-hand side of the first-peak of the radial distribution function. The dashed lines shown in Fig. 5.1 represent the power-law approximation to the actual radial distribution function.

We know that the potential of mean force [63] between two atoms is related to the radial distribution function by $V_{\mathrm{m}}/kT = -\ln g(r) \sim -\ln(r-\sigma)^{\lambda}$, where the ion-core diameter σ indicates the mutual separation between two ions at which the interaction energy is practically infinite. If the separation between two ions is small, V_{m} reduces to the short-range part of the ion-ion repulsion. Hence, λ is proportional to the steepness of the short-range effective repulsion and inversely proportional to the softness of the pseudopotential, which scales as $1/\lambda$.

Subsequently, with the power-law approximation for $g(r)$ in Eq. (5.5), the change in connectivity becomes a function of the repulsion steepness λ: $\delta Z \sim \delta\phi^{1+\lambda}$. When decreasing the temperature by $\delta T < 0$, the atomic packing fraction grows by $\delta\phi = -\phi\alpha_T\delta T > 0$. Consequently, the connectivity Z increases more strongly for steeper pseudopotentials than for the softer counterpart. Analogously, an increase of temperature, $\delta T > 0$, causes the atomic connectivity to decrease more abruptly with T for a steep ion-ion repulsion, and more gradually for a softer interaction.

5.4 High-frequency limit of the shear modulus

Experimental measurements of the viscosity and shear modulus of supercooled liquid metals at the glass transition can be obtained using ultrasonic techniques, which probe the material response at frequencies in the GHz range [49]. These high frequencies exceed the typical relaxation frequency of a metallic glass by several orders of magnitude [94]. Under such conditions, the response to an applied oscillatory shear strain generally is dominated by the instantaneous quasi-affine limit of the shear modulus. For frequencies ω much larger than the inverse of the Maxwell relaxation time τ, that is for $\omega\tau \gg 1$, the shear modulus cannot decay through a non-affine relaxation process. This situation is sketched in Fig. 5.2 together with the low-frequency case, where the non-affine decay is possible.

At high frequency, the atoms cannot leave their affine positions to reach the non-affine equilibrium positions, as the deformation is too quickly reverted. Hence, the elastic response at GHz frequencies is predominantly affine, as can be seen by taking the infinite-frequency limit of Eq. (1.49). Considering Eq. (5.4), this means that the shear modulus is reduced to its affine contribution in the sense that $G \xrightarrow{\omega\to\infty} G_{\mathrm{A}}$. Consequently, in this regime the expression for G is proportional to Z [10], but no longer depends on the critical connectivity Z_c. Therefore, it holds true that $\delta Z \to Z$ and $\delta\phi \to \phi$. Setting Z_c and ϕ_c to zero is the defining feature of the high-frequency quasi-affine limit [101]. Going back to Eq. (5.1), we recognise that in the regime $\omega\tau \gg 1$ this leaves us with $G = \frac{1}{5\pi}\frac{\kappa}{R_0}\phi Z$. We recall that the packing fraction depends on T, $\phi(T) \sim \mathrm{e}^{-\alpha_T T}$ and, thus, we obtain $Z(T) \sim \mathrm{e}^{-(1+\lambda)\alpha_T T}$. Upon replacing this result in the above equation for G, we find that the T-dependence of the shear modulus is dictated by

$$G(T) \sim \frac{1}{5\pi}\frac{\kappa}{R_0}\exp\Big[-(2+\lambda)\alpha_T T\Big]. \tag{5.6}$$

The high-frequency shear modulus now explicitly depends on the softness of the interaction potential, and on the thermal expansion coefficient α_T. Both these crucial effects are reflections of the anharmonicity of the elastic response.

As already hinted above, we note that in general there is also a phonon contribution to the shear modulus proportional to $kT\mathrm{e}^{-\alpha_T T}$. However, this contribution is typically negligible with respect to the one in Eq. (5.6) [60], even more so, if one considers, as it will be shown below, that typical values of λ are in the range $100 - 400$.

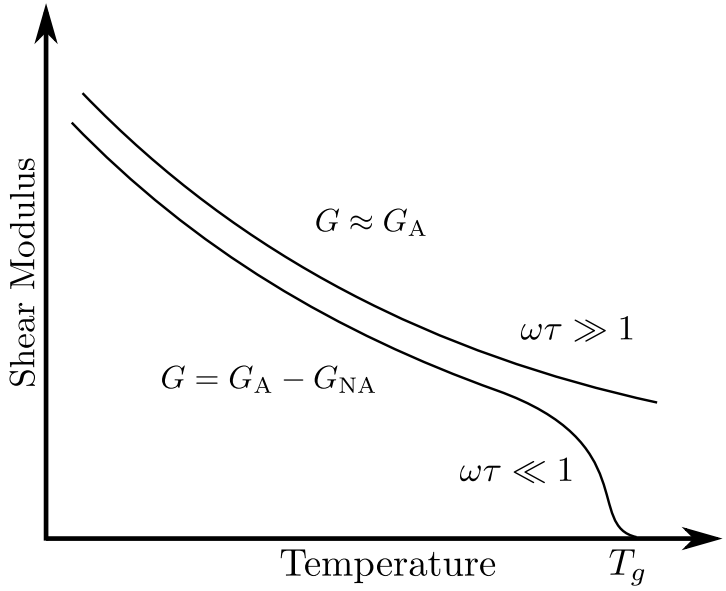

Fig. 5.2 In the high-frequency regime the affine shear modulus represents a good approximation to the actual behaviour of the shear modulus $G = G_{\mathrm{A}} - G_{\mathrm{NA}}$.

5.5 Interatomic repulsion and fragility

The above expression for the high-frequency affine shear modulus can be rewritten as

$$G(T) = C_G \exp\left\{\left[\alpha_T T_g(2+\lambda)\left(1 - \frac{T}{T_g}\right)\right]\right\}, \tag{5.7}$$

where $C_G = \frac{\varepsilon}{5\pi}\frac{\kappa}{R_0}\mathrm{e}^{-\alpha_T T_g(2+\lambda)}$ is a prefactor independent of T. The constant ε stems from the integration of α_T and from the dimensional prefactor in the power-law ansatz for $g(r)$. All the parameters in this expression, which are given in Tab. 5.1, are fixed by the experimental protocol, apart from the fitting parameter λ related to the ion-ion repulsion steepness. The thermal expansion coefficient α_T and the glass transition temperature T_g are material specific parameters. In addition, the parameter C_G represents at the glass transition temperature measured in experiment.

With Eq. (5.7) at hand, we can generate a one-parameter fit to the experimental data provided from Ref. [49], which accurately captures the data sets for the three metallic glass alloys, as can be seen from Fig. 5.3. The different slope of the three depicted curves reflects the fact that the repulsion steepness λ in Eq. (5.7) controls the behaviour of $G(T)$. A decreasing λ, among the different alloys, correlates with a slower decrease of the shear modulus upon increasing the temperature.

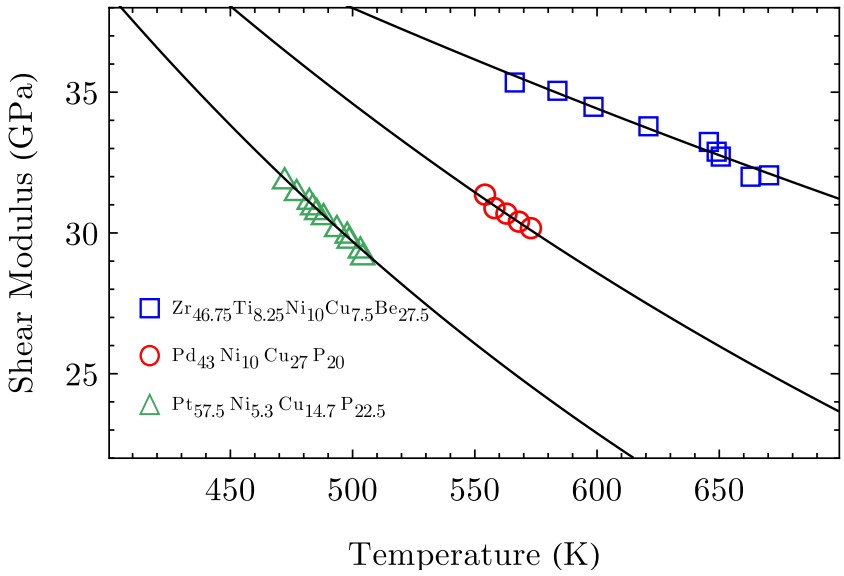

Fig. 5.3 The experimental data points for various glass-forming alloys from [49] and the respective fitting curves for the shear modulus. The solid lines are the one-parameter fitting curves obtained using the expressions Eqs. (5.7). The values used for the fittings are reported in Tab. 5.1.

Furthermore, we can use our model for the high-frequency shear modulus to evaluate the activation energy $E(T)$ involved in restructuring the glassy cage and, hence, the viscosity η of the melts. Within the framework of the shoving or elastic model of the glass transition [88, 29, 26, 24], the activation energy for local cooperative rearrangements is $E(T) = G_{\mathrm{A}} V_{\mathrm{c}}$. The characteristic atomic volume V_{c} appearing here is accessible through the theoretical fitting to the viscosity data, although its value is approximately specified by the atomic composition of the alloy. Replacing the expression for the activation energy in the Arrhenius relation given by the shoving model of the glass transition, and using Eq. (5.7) for the high-frequency shear modulus G_{A} inside $E(T)$, we obtain the following analytical expression for the viscosity,

$$\frac{\eta(T)}{\eta_0} = \exp\left\{\frac{V_c C_G}{k\,T}\exp\left\{\left[(2+\lambda)\alpha_T T_g\left(1-\frac{T}{T_g}\right)\right]\right\}\right\}, \tag{5.8}$$

where η_0 is a normalisation constant. It is important to note how the double-exponential form of the viscosity versus T arises. The first exponential stems from the elastic activation described in the framework of the shoving model, whereas the second exponential is due to the Debye-Grüneisen thermal expansion rooted in lattice-dynamical considerations, and ultimately related to anharmonicity.

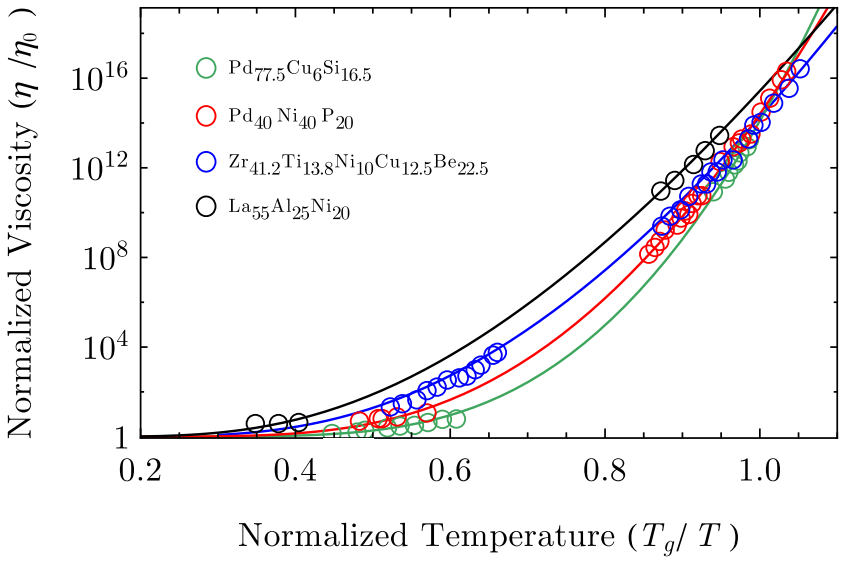

Fig. 5.4 The experimental data points for various glass-forming alloys from [49] and the respective fitting curves for the viscosity. The solid lines are the fitting curves obtained using the expressions Eqs. (5.8). The values used for the fittings are reported in Tab. 5.1.

We compare the theoretical predictions to the experimental data of Ref. [49] in Fig. 5.4. In this case there is also an excellent agreement between theory and experiment with the adjustable parameters being λ, the steepness of the short-ranged ion-ion repulsion, and V_c, the characteristic atomic volume.

Table 5.1 Summary of the experimental data

Alloy	$T_g(K)$	$10^2\alpha_T T_g$	λ	C_G (GPa)	$V_c(10^{-27}m^3)$	$m(\lambda)$	m
$Zr_{46.75}$ $Ti_{8.25}$ $Ni_{10}Cu_{7.5}$ $Be_{27.5}$	597[49]	0.591	99.7	34.52	—	—	—
Pd_{43} Cu_{27} Ni_{10} P_{20}	567[49]	0.935[50]	115.9	30.44	—	—	—
$Pt_{57.5}$ $Ni_{5.3}$ $Cu_{14.7}$ $P_{22.5}$	489[49]	0.776	164.2	30.56	—	—	—
La_{55} Al_{25} Ni_{20}	465[50]	0.711[50]	196.2	15.4 [94]	0.0148	37.16	$37^{[49]}_{450K}$ $33^{[72]}_{462K}$
$Zr_{41.2}$ $Ti_{13.8}$ Ni_{10} $Cu_{12.5}$ $Be_{22.5}$	623[50]	0.617[50]	276.4	33.2[49]	0.0085	38.74	$40^{[49]}_{613K}$ $39^{[95]}_{648K}$
Pd_{40} Ni_{40} P_{20}	551[50]	0.856[50]	286.5	36.5 [94]	0.0069	49.91	$50^{[49]}_{560K}$ $41^{[15]}_{580K}$
$Pd_{77.5}$ Cu_6 $Si_{16.5}$	625[50]	0.865[50]	381.2	32.9 [94]	0.0084	60.04	$61^{[49]}_{634K}$ $52^{[15]}_{635K}$

With the model developed above, we are in the position to relate the atomic-scale properties of the interaction between ions to the experimentally observable macroscopic response of the material. We now consider the behaviour of the viscosity in Fig. 5.4 together with the corresponding behaviour of the interaction parameter λ for various alloys in Tab. 5.1. Evidently, upon approaching the glass transition, the slope of the viscosity $\eta(T)$ is controlled by the interatomic repulsion steepness λ, which depends on the atomic composition of the alloy. A steeper pseudopotential repulsion between two nearest-neighbour ions goes hand in hand with a steeper rise of viscosity, when T is increased. This observation leads us straight to connecting the softness of the potential to the fragility of metallic glasses. The fragility is given as the slope of the viscosity evaluated at the glass transition temperature T_g, i.e. $m = \left(\frac{\partial \log_{10}(\eta/\eta_0)}{\partial(T_g/T)}\right)\Big|_{T=T_g}$ [3]. Using the analytical expression for η, Eq. (5.8), we obtain a simple relation between the fragility m and the steepness of the interatomic repulsion λ given by

$$m(\lambda) = \frac{1}{\ln 10}\frac{V_c C_G}{kT_g}\Big[1 + (2+\lambda)\alpha_T T_g\Big]. \tag{5.9}$$

Metallic glasses with a steeper repulsive part of the interatomic interaction are thus more fragile. The values of the fragility obtained for the various alloys of Ref. [49] are listed in Tab. 5.1, together with the fitted values of the interatomic repulsion steepness λ. Good agreement is also found with independent experimental measurements of m from the literature. Intriguingly, this prediction is in full agreement with the experimental findings of Ref. [65]. In that work the softness of the interparticle potential was varied in a model colloidal glass, where the energy scale is orders of magnitude smaller than in metals. The model also can capture the behaviour of m observed in simulation studies of Lennard-Jones glasses, where the attractive anharmonicity controls the fragility via the thermal expansion coefficient and, by construction, a high anharmonicity is accompanied by a low repulsion steepness [9].

5.6 Extracting pseudopotentials from experimental data

Given the schematic form of the repulsive short-range part of the interaction, $-\ln(r-\sigma)^{\lambda}$, used in the fitting, it is desirable to map this semi-empirical repulsion onto a physically realistic interatomic pseudopotential. This can be achieved by using an Ashcroft-type pseudopotential for modelling the Thomas-Fermi screened interionic Coulomb repul-

sion [35] and, in addition, a Born-Mayer interaction term which accounts for the effect of electron-overlap and Pauli exclusion repulsion between valence-electron shells of two interacting ions [69]. A short discussion of this matter can be found in Appendix D. This combination of the two contributions to the interaction is the most meaningful choice for the present situation, as discussed in [89].

The softness of the pseudopotential is predominantly controlled by the Born-Mayer parameters, because electron-overlap repulsion between valence electrons is more energetic over a broader length scale compared to the Ashcroft contribution, as illustrated in Appendix D. Physically, a slower decay of the electron-overlap repulsion with distance reflects the softness of the effective interaction. The glass stability, however, is optimised by the coexistence of both softness and substantial repulsion, as is the case for technologically important alloys, like binary Zr-Cu alloys [76].

Microscopically, it is the strongly anisotropic density distribution of d-shell electrons, due to the quadrupolar d-wave symmetry, which provides significant softness (upon taking a spherical average), compared to the more isotropic electron density distribution of elements whose outer shells are dominated by s-electrons. Hence, the form of the pseudopotentials may explain the difference in stability and fragility based on the composition of the alloy. In our model, this effect is expressed by the energy-scale of the Born-Mayer repulsion B. In particular, we find that B correlates linearly with the fragility index m, as shown in Fig. 5.5 (b). This correlation reflects the fact that d-shell orbitals effectively soften the interatomic repulsion, whereas s-shell electrons are associated with steeper repulsion and higher fragility.

The second effect which is captured by this approach is the ion-size mismatch. If smaller metal atoms are added to larger atoms, fragility decreases and strong glasses can be formed. This mechanism which affects multi-component alloys is analysed and discussed in [28]. Again, this is the consequence of an effectively softer interatomic repulsion. Smaller atoms of metalloids like P, B or Si can easily come closer to larger ions like Pd, La, Zr or Cu by fitting into the voids of the quadrupolar d-shell structure. In general, this topological effect also leads to a softer average pseudopotential. This connection between macroscopic flow behaviour, encoded in m, and electronic structure is an important step towards a unifying framework for understanding and controlling mechanical properties of metallic glasses on the atomic scale.

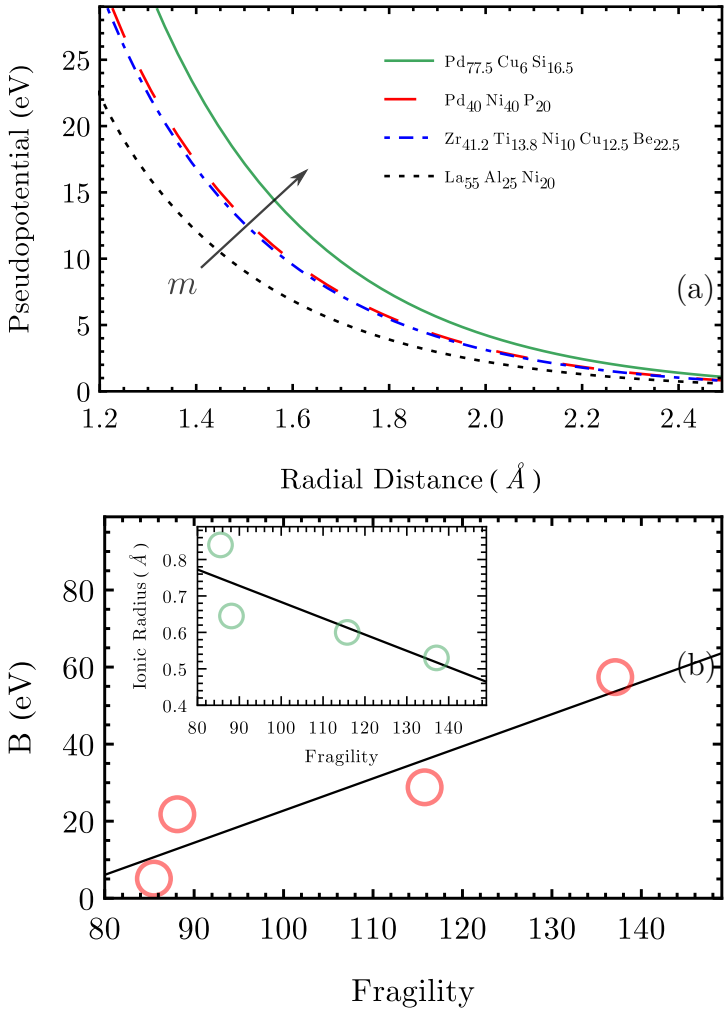

Fig. 5.5 (a) The Ashcroft-Born-Mayer pseudopotential is depicted for four different glass-forming alloys. The fragility m increases with the pseudopotential steepness. (b) The value of the Born-Mayer energy scale increases linearly with the fragility. Also, it is observed that the average ionic diameter decreases linearly with the fragility.

5.7 Connection with cooperative shear events

As already pointed out, the energy necessary to trigger a shoving event is $E(T) = G_{\mathrm{A}}(T)V_c$. Importantly, the characteristic atomic volume V_c is not the volume change which is connected to a shoving event. This quantity, also called the activation volume ΔV, is connected to V_c and the initial shoving volume V via the relation

$$V_c = \frac{2}{3}\frac{(\Delta V)^2}{V}, \tag{5.10}$$

which can be derived in the framework of the elasticity theory of an isotropic expanding sphere [26].

It is widely believed that shear transformation zones (STZs) are the fundamental plastic entities responsible for the yielding mechanism in metallic glasses. STZs are clusters of atoms which can cooperatively rearrange under shear stress, and are directly connected to the local accumulation of free volume [58]. It is in this sense that the activation of STZs allows the involved atoms to rearrange more easily under shear stress. Assuming that the initial shoving volume V corresponds to the volume of a STZ, we find a direct relation between the characteristic volume V_c and the activation volume ΔV in the following way. According to Ref. [48], the total energy barrier W between two basins in the potential energy landscape can be evaluated to give $W \approx (1/320)\, G_{\mathrm{A}}\Omega$, see Appendix D. We assume that W in the cooperative shear model is approximately equal to the shoving energy, that is $W \approx E$. It directly follows that $G_{\mathrm{A}}V_c \approx (1/320)G_{\mathrm{A}}\Omega$, which leads us to conclude that the effective volume of a STZ is $\Omega \approx 320V_c$.

It is physically meaningful that the effective STZ volume Ω is approximately equivalent to the initial shoving volume V, henceforth calling it V_{STZ}. Using the identification $\Omega \approx V_{\mathrm{STZ}} \approx 320V_c$, we can use the values for V_c to extract values for STZ volumes from our theoretical analysis and compare them to experimental results for V_{STZ} from Ref. [59]. We find that the calculated STZ volumes for the respective alloys are in very good agreement with the experimental results for similar alloys, which is displayed in Tab.2. Moreover, using $V_{\mathrm{STZ}} \approx 320V_c$ together with Eq. (5.10), we obtain a relation between the activation volume and the characteristic volume V_c given by $\Delta V \approx \sqrt{480}\, V_c$. With the values for V_c from the viscosity fitting, we can calculate the activation volume for the corresponding alloys to be in the range $151 - 324\,\mathring{A}^3$. For a Pd-based metallic glass, an activation volume of $106\mathring{A}^3$ was found experimentally [44], which is not too far from our estimate for the alloys discussed here.

Elsewhere the activation volume for $Zr_{41.2}$ $Ti_{13.8}$ $Cu_{12.5}$ Ni_{10} $Be_{22.5}$ is determined to be $75\,\mathring{A}^3$ [79]. For the same alloy, we calculate the value for the activation volume from the corresponding V_c with the result $\Delta V = 186\,\mathring{A}^3$, which is about 2.5 times larger in comparison. This difference may be explained by the different deformation protocols (shear amplitude, applied stress rate, etc.), in the respective experiments. It is argued in Refs. [31, 105] that a higher degree of applied stress leads to an increase of the size of the individual flow units, which means that both the STZ volume and the activation volume tend to increase.

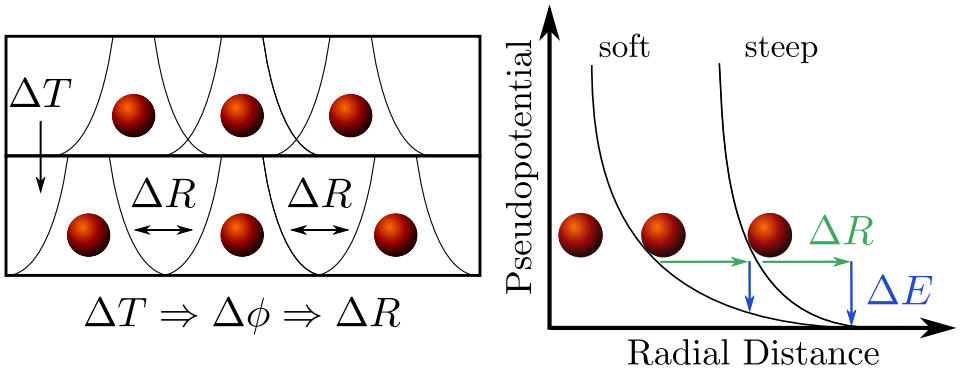

Fig. 5.6 (Left) The distance between the atoms decreases as the temperature is increased leading to a smaller overlap of the effective interaction potentials. (Right) The growth of the cage by ΔR when increasing the temperature by ΔT and the corresponding loss of stabilising energy ΔE. The potentials are shifted for the sake of clarity.

Table 5.2 Experimental and theoretical STZ volumes

Alloy	$V_c\,(\mathrm{nm}^3)$	$\Omega\,(\mathrm{nm}^3)$
$Pd_{40}\ Ni_{40}\ P_{20}$	0.0069	2.21
$Pd_{48}\ Ni_{32}\ P_{20}$	-	2.36[59]
$Zr_{41.2}\ Ti_{13.8}\ Ni_{10}\ Cu_{12.5}\ Be_{22.5}$	0.0085	2.72
$Zr_{46.75}\ Ti_{8.25}\ Ni_{10}\ Cu_{7.5}\ Be_{27.5}$	-	3.13[59]
$La_{55}\ Al_{25}\ Ni_{20}$	0.0148	4.74
$La_{55}\ Al_{25}\ Ni_{20}$	-	5.31[59]

5.8 Conclusion

The basic mechanism controlling the mechanical response in the high-frequency regime and the fragility of liquid metals close to vitrification can be summarised in the following way. Due to thermal expansion, an increase in the temperature leads to a decreasing atomic packing fraction and, thus, to a decrease of atomic connectivity.

The latter effect softens the material, causing the shear modulus to decrease with T. The rate of this process is controlled by the steepness of the repulsive short-range interatomic interaction. This mechanism propagates to the viscosity, and it controls its temperature dependence and leads to fragile behaviour with steep interatomic repulsion, and to strong glasses when the repulsion is softer. In an amorphous solid we can picture this situation by considering a reference atom which is surrounded by a number of neighbouring atoms, forming a disordered cage. The repulsive interaction between these particles provides stability to the cage. When the temperature is increased, a corresponding change of packing fraction takes place, implying that the disordered cage around the reference atom becomes larger and less stable, see Fig. 5.6.

With this moving farther apart of the nearest neighbours from the reference atom, the local stabilising energy felt by the atoms decreases due to a smaller overlap of the repulsive interatomic interactions by ΔE. At the onset of the glass transition, the stabilising effect of the atomic cage breaks down, which ultimately leads to the vanishing of the zero-frequency shear modulus at T_g. It is the steepness of the repulsive pseudopotential which controls how rapidly or abrupt the stabilising energy decreases as the temperature is increased. For an alloy whose constituents exhibit a steeper interatomic repulsion, this process of destabilisation will be more abrupt resulting in a faster variation of the shear modulus and viscosity with T and, correspondingly, to a more fragile glass. Taken together, this allows us to conclude that in the present framework the principle connecting softness and fragility found experimentally for colloidal glass formers in Ref. [65] is transferable to metallic glass-forming liquids.

We also show that the steepness of the interatomic repulsion for various metallic alloys can be mapped one-to-one onto a pseudopotential with two contributions. The overall softness of the pseudopotential is mainly controlled by Born-Mayer repulsion stemming from the overlap of valence-shell electrons. A direct relation of linear proportionality between the fragility index m and the Born-Mayer energy B is obtained from the fitting to experimental data. Lower values of B may correlate with mixtures of elements having outer electrons in d-shells, as is the case of Cu in Zr-Cu alloys, or with the concentration of metalloid in metal-metalloid mixtures. Systematic studies in the future using ab-initio simulations may shed light on the link with the detailed electronic structure.

Furthermore, we connect the characteristic atomic volume V_c with the size of STZs. In this regard, STZs appear to be regions in the amorphous solid with a relatively low average atomic connectivity Z. These regions are prone to elastic stress accumulation, leading to an increase in individual shoving events, which eventually results in macroscopic plasticity. While there exists a clear linear relation between the fragility and the repulsive steepness λ, the correlation between the size of a STZ and the fragility exhibits no simple form and remains to be understood in future investigations. Another matter of ongoing debate is the temperature dependence of the parameter λ, which characterises the strength of the repulsive part of the interaction. In a recent study the temperature independence of λ was questioned on the basis of simulations and experiments involving various metallic glass alloys and also led to different conclusions about the relation between the fragility and λ [73]. This, however, is at variance with the simulation results in Ref. [56], where the temperature independence of λ for a CuZr binary alloy was demonstrated.

References

[1] Abrahamson, A. A. (1969). Born-Mayer-type interatomic potential for neutral ground-state atoms with $Z = 2$ to $Z = 105$. *Physical Review*, 178(1):76–79.

[2] Alexander, S. (1998). Amorphous solids: their structure, lattice dynamics and elasticity. *Physics Reports*, 296(2-4):65–236.

[3] Angell, C. A., Ngai, K. L., McKenna, G. B., McMillan, P. F., and Martin, S. W. (2000). Relaxation in glassforming liquids and amorphous solids. *Journal of Applied Physics*, 88(6):3113.

[4] Ashcroft, N. W. and Mermin, N. D. (1976). *Solid State Physics*. Holt, Rinehart and Winston, New York.

[5] Beltukov, Y. M., Fusco, C., Parshin, D. A., and Tanguy, A. (2016). Boson peak and Ioffe-Regel criterion in amorphous siliconlike materials: The effect of bond directionality. *Physical Review E*, 93(2):023006.

[6] Beltukov, Y. M. and Parshin, D. A. (2011). Theory of sparse random matrices and vibrational spectra of amorphous solids. *Physics of the Solid State*, 53(1):151–162.

[7] Bennett, C., Polk, D., and Turnbull, D. (1971). Role of composition in metallic glass formation. *Acta Metallurgica*, 19(12):1295–1298.

[8] Binder, K. and Kob, W. (2011). *Glassy Materials and Disordered Solids: An Introduction to Their Statistical Mechanics*. World Scientific.

[9] Bordat, P., Affouard, F., Descamps, M., and Ngai, K. L. (2004). Does the interaction potential determine both the fragility of a liquid and the vibrational properties of its glassy state? *Physical Review Letters*, 93(10):105502.

[10] Born, M. and Huang, K. (1954). *Dynamical Theory of Crystal Lattices*. Oxford University Press.

[11] Born, M. and Huang, K. (1988). *Dynamical Theory of Crystal Lattices Oxford Classic Texts in the Physical Sciences*. Clarendon Press, Oxford.

[12] Böttger, H. (1983). *Principles of the Theory of Lattice Dynamics*. Physik-Verlag.

[13] Braun, P. V., Rinne, S. A., and García-Santamaría, F. (2006). Introducing defects in 3D photonic crystals: State of the art. *Advanced Materials*, 18(20):2665–2678.

[14] Broedersz, C. P., Mao, X., Lubensky, T. C., and Mackintosh, F. C. (2011). Criticality and isostaticity in fibre networks. *Nature Physics*, 7(12):983–988.

[15] Chen, H. (1978). Alloying effect on the viscous flow in metallic glasses. *Journal of Non-Crystalline Solids*, 29(2):223–229.

[16] Chikkadi, V., Wegdam, G., Bonn, D., Nienhuis, B., and Schall, P. (2011). Long-Range Strain Correlations in Sheared Colloidal Glasses. *Physical Review Letters*, 107(19):198303.

[17] Chowdhury, S., Abraham, S., Hudson, T., and Harrowell, P. (2016). Long range stress correlations in the inherent structures of liquids at rest. *The Journal of Chemical Physics*, 144(12):124508.

[18] Crawford, J. H. and Slifkin, L. M., editors (1975). *Point Defects in Solids*. Springer US, Boston, MA.

[19] Dasgupta, R., Joy, A., Hentschel, H., and Procaccia, I. (2013). Derivation of the Johnson-Samwer $T^{2/3}$ temperature dependence of the yield strain in metallic glasses. *Physical Review B*, 020101:2–5.

[20] Dean, P. (1972). The vibrational properties of disordered systems: Numerical studies. *Reviews of Modern Physics*, 44(2):127–168.

[21] DeGiuli, E., Laversanne-Finot, A., Düring, G., Lerner, E., and Wyart, M. (2014). Effects of coordination and pressure on sound attenuation, boson peak and elasticity in amorphous solids. *Soft Matter*, 10(30):5628.

[22] Düring, G., Lerner, E., and Wyart, M. (2013). Phonon gap and localization lengths in floppy materials. *Soft Matter*, 9(1):146–154.

[23] Duxbury, M. T. P. (2002). *Rigidity Theory and Applications*. Springer US.

[24] Dyre, J. (2006). Colloquium: The glass transition and elastic models of glass-forming liquids. *Reviews of Modern Physics*, 78(3):953–972.

[25] Dyre, J., Olsen, N., and Christensen, T. (1996). Local elastic expansion model for viscous-flow activation energies of glass-forming molecular liquids. *Physical Review B*, 53(5):2171–2174.

[26] Dyre, J. C. (1998). Source of non-Arrhenius average relaxation time in glass-forming liquids. *Journal of Non-Crystalline Solids*, 235-237:142–149.

[27] Economou, E. N. (2006). *Green's Functions in Quantum Physics*, volume 7.

[28] Egami, T. (2002). Nano-glass Mechanism of Bulk Metallic Glass Formation. *Materials Transactions*, 43(3):510–517.

[29] Eyring, H. (1936). Viscosity, Plasticity, and Diffusion as Examples of Absolute Reaction Rates. *The Journal of Chemical Physics*, 4(4):283.

[30] Faber, T. E. (1972). *Introduction to the theory of liquid metals*. Cambridge University Press.

[31] Fan, Y., Iwashita, T., and Egami, T. (2014). How thermally activated deformation starts in metallic glass. *Nature Communications*, 5(May):5083.

[32] Feng, S., Thorpe, M. F., and Garboczi, E. (1985a). Effective-medium theory of percolation on central-force elastic networks. *Physical Review B*, 31(1):276–280.

[33] Feng, S., Thorpe, M. F., and Garboczi, E. (1985b). Effective-medium theory of percolation on polymer networks. *Physical Review B*, 31(2):1–8.

[34] Feng, S., Thorpe, M. F., and Garboczi, E. (1985c). Effective-medium theory of percolation on polymer networks. *Physical Review B*, 31(2):1–8.

[35] Finnis, M. (2003). *Interatomic forces in condensed matter*. Oxford University Press.

[36] Frenkel, Y. I. (1955). *Kinetic theory of liquids*. Dover.

[37] Ganguly, S. and Sengupta, S. (2017). Excess vibrational modes of a crystal in an external non-affine field. *Journal of Chemical Sciences*, 129(7):891–897.

[38] Ganguly, S., Sengupta, S., and Sollich, P. (2015). Statistics of non-affine defect precursors: tailoring defect densities in colloidal crystals using external fields. *Soft Matter*, 11(22):4517–4526.

[39] Ganguly, S., Sengupta, S., Sollich, P., and Rao, M. (2013). Nonaffine displacements in crystalline solids in the harmonic limit. *Physical Review E - Statistical, Nonlinear, and Soft Matter Physics*, 87(4):042801.

[40] Garboczi, E. J. and Thorpe, M. F. (1985). Density of states for random-central-force elastic networks. *Physical Review B*, 32(7):4513–4518.

[41] Gaydaenko, V. and Nikulin, V. (1970). Born-Mayer interatomic potential for atoms with Z = 2 to Z = 36. *Chemical Physics Letters*, 7(3):360–362.

[42] Gelin, S., Tanaka, H., and Lemaître, A. (2016). Anomalous phonon scattering and elastic correlations in amorphous solids. *Nature Materials*, 15(11):1177–1181.

[43] Hafner, J. (1987). *From Hamiltonians to Phase Diagrams*, volume 70 of *Springer Series in Solid-State Sciences*. Springer Berlin Heidelberg, Berlin, Heidelberg.

[44] Heggen, M., Spaepen, F., and Feuerbacher, M. (2005). Creation and annihilation of free volume during homogeneous flow of a metallic glass. *Journal of Applied Physics*, 97(3):033506.

[45] Imhof, A. (2003). Three-Dimensional Photonic Crystals Made from Colloids. *Nanoscale Materials*, pages 423–454.

[46] Jacobs, D. J. and Thorpe, M. F. (1996). Generic rigidity percolation in two dimensions. *Physical Review E*, 53(4):3682–3693.

[47] Jänich, K. (2005). *Mathematik 1 Geschrieben für Physiker*. Springer-Verlag Berlin Heidelberg.

[48] Johnson, W. and Samwer, K. (2005). A Universal Criterion for Plastic Yielding of Metallic Glasses with a $(T/T_g)^{2/3}$ Temperature Dependence. *Physical Review Letters*, 95(19):195501.

[49] Johnson, W. L., Demetriou, M. D., Harmon, J. S., Lind, M. L., and Samwer, K. (2007). Rheology and Ultrasonic Properties of Metallic Glass-Forming Liquids: A Potential Energy Landscape Perspective. *MRS Bulletin*, 32(08):644–650.

[50] Kato, H., Chen, H. S., and Inoue, a. (2008). Relationship between thermal expansion coefficient and glass transition temperature in metallic glasses. *Scripta Materialia*, 58(12):1106–1109.

[51] Keyes, T. (1994). Unstable modes in supercooled and normal liquids: Density of states, energy barriers, and self-diffusion. *J. Chem. Phys.*, 101(6):5081.

[52] Keyes, T. (1996). Instantaneous Normal Mode Approach to Liquid State Dynamics. (5).

[53] Keyes, T. (2006). *Normal Mode Analysis: Theory and applications to biological and chemical systems*. Chapman & Hall.

[54] Kirkpatrick, S. (1973). Percolation and Conduction. *Reviews of Modern Physics*, 45(4):574–588.

[55] Kremer, K. and Grest, G. S. (1990). Dynamics of entangled linear polymer melts: A molecular-dynamics simulation. *The Journal of Chemical Physics*, 92(8):5057–5086.

[56] Lagogianni, A. E., Krausser, J., Evenson, Z., Samwer, K., and Zaccone, A. (2016). Unifying interatomic potential, $g(r)$, elasticity, viscosity, and fragility of metallic glasses: analytical model, simulations, and experiments. *Journal of Statistical Mechanics: Theory and Experiment*, 2016(8):084001.

[57] Lemaître, A. and Maloney, C. (2006). Sum Rules for the Quasi-Static and Visco-Elastic Response of Disordered Solids at Zero Temperature. *Journal of Statistical Physics*, 123(2):415–453.

[58] Li, L., Homer, E., and Schuh, C. (2013). Shear transformation zone dynamics model for metallic glasses incorporating free volume as a state variable. *Acta Materialia*, 61(9):3347–3359.

[59] Liu, S., Wang, Z., Peng, H., Yu, H., and Wang, W. (2012). The activation energy and volume of flow units of metallic glasses. *Scripta Materialia*, 67(1):9–12.

[60] Lüthi, B. (2005). *Physical Acoustics in the Solid State*, volume 148 of *Solid State Sciences*. Springer-Verlag, Berlin/Heidelberg.

[61] Maloney, C. and Lemaître, A. (2004). Universal breakdown of elasticity at the onset of material failure. *Physical Review Letters*, 93(19):5–8.

[62] Maloney, C. and Lemaître, A. (2006). Amorphous systems in athermal, quasistatic shear. *Physical Review E*, 74(1):016118.

[63] March, N. H. (2005). *Liquid metals: concepts and theory*. Cambridge University Press.

[64] Marruzzo, A., Schirmacher, W., Fratalocchi, A., and Ruocco, G. (2013). Heterogeneous shear elasticity of glasses: the origin of the boson peak. *Scientific Reports*, 3(1):1407.

[65] Mattsson, J., Wyss, H. M., Fernandez-Nieves, A., Miyazaki, K., Hu, Z., Reichman, D. R., and Weitz, D. a. (2009). Soft colloids make strong glasses. *Nature*, 462(7269):83–6.

[66] Mazzacurati, V., Ruocco, G., and Sampoli, M. (1996). Low-frequency atomic motion in a model glass. *Europhysics Letters (EPL)*, 34(9):681–686.

[67] Milkus, R. and Zaccone, A. (2016). Local inversion-symmetry breaking controls the boson peak in glasses and crystals. *Physical Review B*, 93(9):094204.

[68] Mizuno, H., Mossa, S., and Barrat, J.-L. (2014). Acoustic excitations and elastic heterogeneities in disordered solids. *Proceedings of the National Academy of Sciences*, 111(33):11949–11954.

[69] Mott, N. F. and Jones, H. (1958). *The theory of the properties of metals and alloys*. Courier Dover Publications.

[70] Na, J. H., Demetriou, M. D., Floyd, M., Hoff, A., Garrett, G. R., and Johnson, W. L. (2014). Compositional landscape for glass formation in metal alloys. *Proceedings of the National Academy of Sciences of the United States of America*, 111(25):9031–6.

[71] Neudecker, M. and Mayr, S. (2009). Dynamics of shear localization and stress relaxation in amorphous $Cu_{50}Ti_{50}$. *Acta Materialia*, 57(5):1437–1441.

[72] Okumura, H., Inoue, A., and Masumoto, T. (1993). Heating rate dependence of two glass transitions and phase separation for a $La_{55}Al_{25}Ni_{20}$ amorphous alloy. *Acta Metallurgica et Materialia*, 41(3):915–921.

[73] Pueblo, C. E., Sun, M., and Kelton, K. F. (2017). Strength of the repulsive part of the interatomic potential determines fragility in metallic liquids. *Nature Materials*, 16(8):792–796.

[74] Qi, M., Lidorikis, E., Rakich, P. T., Johnson, S. G., Joannopoulos, J. D., Ippen, E. P., and Smith, H. I. (2004). A three-dimensional optical photonic crystal with designed point defects. *Nature*, 429(6991):538–542.

[75] Rahman, A., Mandell, M. J., and McTague, J. P. (1976). Molecular dynamics study of an amorphous Lennard-Jones system at low temperature. *The Journal of Chemical Physics*, 64(4):1564–1568.

[76] Samwer, K. and Löhneysen, H. v. (1982). Amorphous superconducting Zr_xCu_{1-x}: Electronic properties, stability, and low-energy excitations. *Physical Review B*, 26(1):107–123.

[77] Schirmacher, W. (2006). Thermal conductivity of glassy materials and the “boson peak". *Europhysics Letters (EPL)*, 73(6):892–898.

[78] Schirmacher, W., Scopigno, T., and Ruocco, G. (2015). Theory of vibrational anomalies in glasses. *Journal of Non-Crystalline Solids*, 407:133–140.

[79] Schuh, C., Hufnagel, T., and Ramamurty, U. (2007). Mechanical behavior of amorphous alloys. *Acta Materialia*, 55(12):4067–4109.

[80] Scossa-Romano, E. (2010). *Nonaffine elastic response of random spring networks*. PhD thesis, ETH Zurich.

[81] Sengupta, S., Vasconcelos, F., Affouard, F., and Sastry, S. (2011). Dependence of the fragility of a glass former on the softness of interparticle interactions. *The Journal of Chemical Physics*, 135(19):194503.

[82] Shannon, R. D. (1976). Revised effective ionic radii and systematic studies of interatomic distances in halides and chalcogenides. *Acta Crystallographica Section A*, 32(5):751–767.

[83] Sidebottom, D. L. (2013). *Fundamentals of condensed matter and crystalline physics*. Cambridge University Press.

[84] Stickler, B. A. and Schachinger, E. (2016). *Basic Concepts in Computational Physics*. Springer International Publishing, Cham.

[85] Stratt, R. M. (1995). The Instantaneous Normal Modes of Liquids. *Accounts of Chemical Research*, 28(5):201–207.

[86] Tanguy, A., Leonforte, F., and Barrat, J. L. (2006). Plastic response of a 2D Lennard-Jones amorphous solid: Detailed analysis of the local rearrangements at very slow strain rate. *European Physical Journal E*, 20(3):355–364.

[87] Taraskin, S. N. and Elliott, S. R. (1997). Connection between the true vibrational density of states and that derived from inelastic neutron scattering. *Physical Review B*, 55(1):117–123.

[88] Tobolsky, A., Powell, R. E., and Eyring, H. (1943). Elastic-viscous properties of matter. *Frontiers in Chemistry*, 1:125–190.

[89] Torrens, I. M. (1972). *Interatomic Potentials*. Elsevier.

[90] Veselić, K. (2011). Damped oscillations of linear systems: A mathematical introduction. *Lecture Notes in Mathematics*, 2023:1–226.

[91] Vladimir V. Palyulin, Christopher Ness, Rico Milkus, Robert M. Elder, Timothy W. Sirk and Zaccone, A. (2017). Quantitative prediction of dynamic viscoelastic response of amorphous polymers across the glass transition. *Preprint*.

[92] Wagner, H., Bedorf, D., Küchemann, S., Schwabe, M., Zhang, B., Arnold, W., and Samwer, K. (2011). Local elastic properties of a metallic glass. *Nature Materials*, 10(6):439–442.

[93] Wang, W., Dong, C., and Shek, C. (2004). Bulk metallic glasses. *Materials Science and Engineering: R: Reports*, 44(2-3):45–89.

[94] Wang, W. H. (2012). The elastic properties, elastic models and elastic perspectives of metallic glasses. *Progress in Materials Science*, 57(3):487–656.

[95] Waniuk, T., Busch, R., Masuhr, A., and Johnson, W. (1998). Equilibrium viscosity of the $Zr_{41.2}Ti_{13.8}Cu_{12.5}Ni_{10}Be_{22.5}$ bulk metallic glass-forming liquid and viscous flow during relaxation, phase separation, and primary crystallization.

[96] Weiße, A., Wellein, G., Alvermann, A., and Fehske, H. (2006). The kernel polynomial method. *Reviews of Modern Physics*, 78(1):275–306.

[97] Wu, B., Iwashita, T., and Egami, T. (2015). Anisotropic stress correlations in two-dimensional liquids. *Physical Review E*, 91(3):032301.

[98] Yoshimoto, K., Jain, T. S., Workum, K. V., Nealey, P. F., and de Pablo, J. J. (2004). Mechanical Heterogeneities in Model Polymer Glasses at Small Length Scales. *Physical Review Letters*, 93(17):175501.

[99] Zaccone, A., Blundell, J. R., and Terentjev, E. M. (2011). Network disorder and nonaffine deformations in marginal solids. *Physical Review B*, 84(17):174119.

[100] Zaccone, A., Schall, P., and Terentjev, E. M. (2014). Microscopic origin of nonlinear nonaffine deformation in bulk metallic glasses. *Physical Review B*, 90(14):140203.

[101] Zaccone, A. and Scossa-Romano, E. (2011). Approximate analytical description of the nonaffine response of amorphous solids. *Physical Review B*, 83(18):184205.

[102] Zaccone, A. and Terentjev, E. M. (2013). Disorder-Assisted Melting and the Glass Transition in Amorphous Solids. *Physical Review Letters*, 110(17):178002.

[103] Zargar, R., DeGiuli, E., and Bonn, D. (2016). Scaling for hard-sphere colloidal glasses near jamming. *EPL (Europhysics Letters)*, 116(6):68004.

[104] Zargar, R., Russo, J., Schall, P., Tanaka, H., and Bonn, D. (2014). Disorder and excess modes in hard-sphere colloidal systems. *EPL (Europhysics Letters)*, 108(3):38002.

[105] Zhang, M., Wang, Y., and Dai, L. (2015). Bridging shear transformation zone to the atomic structure of amorphous solids. *Journal of Non-Crystalline Solids*, 410:100–105.

[106] Zhao, Q., Finlayson, C. E., Snoswell, D. R. E., Haines, A., Schäfer, C., Spahn, P., Hellmann, G. P., Petukhov, A. V., Herrmann, L., Burdet, P., Midgley, P. A., Butler, S., Mackley, M., Guo, Q., and Baumberg, J. J. (2016). Large-scale ordering of nanoparticles using viscoelastic shear processing. *Nature Communications*, 7:11661.

Appendix A

The coherent potential approximation

A.1 Effective-medium theory for central-force spring networks

We start with the N-particle Hamiltonian in d dimensions (e.g. of the triangular lattice)

$$\mathcal{H} = \mathcal{H}_0 + \mathcal{V} \tag{A.1}$$

where

$$\mathcal{H}_0 = \mathcal{H}_{\boldsymbol{p}} + \mathcal{H}_{\boldsymbol{u}} \tag{A.2}$$

where $\boldsymbol{p}$ and $\boldsymbol{u}$ are the Nd-dimensional momentum and displacement vector, respectively. For ease of notation, we write the $\boldsymbol{u}$ as

$$|\boldsymbol{u}\rangle = (\boldsymbol{u}_1, \ldots, \boldsymbol{u}_N) \tag{A.3}$$

with the property

$$\langle i|\boldsymbol{u}\rangle = \boldsymbol{u}_i. \tag{A.4}$$

In the harmonic approximation $\mathcal{H}_{\boldsymbol{u}}$ is given by

$$\mathcal{H}_{\boldsymbol{u}} = \frac{1}{2} \sum_{\langle i,j \rangle} k_{ij} \left[(\boldsymbol{u}_i - \boldsymbol{u}_j) \cdot \hat{\boldsymbol{r}}_{ij} \right]^2 \tag{A.5}$$

where $\langle i, j \rangle$ means summing over next neighbors and $\hat{\boldsymbol{r}}_{ij}$ are the unit bond vectors. Introducing the $dN \times dN$ dynamical matrix $\mathcal{M}$ we may write

$$\mathcal{H}_{\boldsymbol{u}} = \langle \boldsymbol{u} | \, \mathcal{M} \, | \boldsymbol{u} \rangle \tag{A.6}$$

with

$$\mathcal{M} = \frac{1}{2} \sum_{\langle i,j \rangle} k_{ij} \hat{\boldsymbol{r}}_{ij} \hat{\boldsymbol{r}}_{ij}^T \left(|i\rangle - |j\rangle \right) \left(\langle i| - \langle j| \right) \tag{A.7}$$

$$= \sum_{\langle i,j \rangle} k_{ij} \hat{\boldsymbol{r}}_{ij} \hat{\boldsymbol{r}}_{ij}^T \mathcal{P}_{ij} \tag{A.8}$$

and define for later use the bond projector $\mathcal{P}_{ij} = \frac{1}{2} \left(|i\rangle - |j\rangle \right) \left(\langle i| - \langle j| \right)$ [54]. Accordingly we define the Green's function of the system as

$$\mathcal{G}(\omega) = \left[\mathcal{M} - m\omega^2 \right]^{-1} \tag{A.9}$$

Following [21, 22], one way to introduce EMT and compute the disorder-averaged Green's functions is to introduce an effective spring constant k_{eff} and write $k_{ij} = k_{\text{eff}} + (k_{ij} - k_{\text{eff}})$ and, correspondingly, decompose the dynamical matrix as $\mathcal{M} = \mathcal{M}_0 + \delta\mathcal{M}$ such that

$$\mathcal{M}_0 = \sum_{\langle i,j \rangle} k_{\text{eff}} \hat{\boldsymbol{r}}_{ij} \hat{\boldsymbol{r}}_{ij}^T \mathcal{P}_{ij} \tag{A.10}$$

and

$$\delta\mathcal{M} = \sum_{\langle i,j \rangle} (k_{ij} - k_{\text{eff}}) \hat{\boldsymbol{r}}_{ij} \hat{\boldsymbol{r}}_{ij}^T \mathcal{P}_{ij}. \tag{A.11}$$

We then can write the Green's function as $\mathcal{G} = \mathcal{G}_0 + \mathcal{G}_0 \mathcal{T} \mathcal{G}_0$, where $\mathcal{G}_0 = [\mathcal{M}_0 - m\omega^2]^{-1}$ is the Green's function of the effective medium. The matrix $\mathcal{T}$ is the scattering matrix

and given by $\mathcal{T} = \delta\mathcal{M}\left[1 - \mathcal{G}_0\delta\mathcal{M}\right]^{-1}$, or equivalently,

$$\mathcal{T} = \delta\mathcal{M} + \delta\mathcal{M}\mathcal{G}_0\delta\mathcal{M} + \delta\mathcal{M}\mathcal{G}_0\delta\mathcal{M}\mathcal{G}_0\delta\mathcal{M} + \ldots \tag{A.12}$$

$$= \delta\mathcal{M}\sum_{n=1}^{\infty}\left[\mathcal{G}_0\delta\mathcal{M}\right]^n. \tag{A.13}$$

Inserting the expression for $\delta\mathcal{M}$ into the above series expansion, we can split the sums over the NN-bonds into diagonal and off-diagonal parts. Since $\mathcal{P}_{ij}$ is a projection operator the contributions containing different powers of the projection can be collected and resummed. The result of this is

$$\mathcal{T} = \sum_{\langle i,j\rangle}\boldsymbol{T}_{ij} + \sum_{\langle i,j\rangle\neq\langle m,n\rangle}\boldsymbol{T}_{ij}\mathcal{G}_0\boldsymbol{T}_{mn} + \ldots \tag{A.14}$$

with

$$\boldsymbol{T}_{ij} = \frac{\left(|i\rangle - |j\rangle\right)\left(k_{ij} - k_{\text{eff}}\right)\left(\langle i| - \langle j|\right)}{1 - \left(k_{ij} - k_{\text{eff}}\right)\hat{\boldsymbol{r}}_{ij}^T\left(\langle i| - \langle j|\right)\mathcal{G}_0\left(|i\rangle - |j\rangle\right)\hat{\boldsymbol{r}}_{ij}}\hat{\boldsymbol{r}}_{ij}\hat{\boldsymbol{r}}_{ij}^T \tag{A.15}$$

We now want to determine the effective spring constant k_{eff} such that it mimics the average behavior of the disordered system [22], i.e. $\langle\mathcal{G}\rangle = \mathcal{G}_0$. This leads to the condition $\langle\mathcal{T}\rangle = 0$, which in the EMT is achieved by setting $\langle\boldsymbol{T}_{ij}\rangle = 0$. We evaluated the average over the disorder according to

$$0 = p\,\boldsymbol{T}_{ij}\Big|_{k_{ij}=k} + (1-p)\,\boldsymbol{T}_{ij}\Big|_{k_{ij}=0} \tag{A.16}$$

meaning that bond randomly removed with probability $1-p$. After some manipulations we can rewrite the above as

$$\hat{\boldsymbol{r}}_{ij}^T\cdot\Big(\left(\langle i| - \langle j|\right)\mathcal{G}_0\left(|i\rangle - |j\rangle\right)\Big)\cdot\hat{\boldsymbol{r}}_{ij} = \frac{k_{\text{eff}} - pk}{k_{\text{eff}}(k - k_{\text{eff}})}. \tag{A.17}$$

The un-disordered, effective lattice is isotropic and homogeneous so that the above equation is independent of the bond label i, j [54, 21]. Hence, $\langle i|\,\mathcal{G}_0\,|i\rangle = \langle j|\,\mathcal{G}_0\,|j\rangle$ and $\langle j|\,\mathcal{G}_0\,|i\rangle = \langle i|\,\mathcal{G}_0\,|j\rangle$. Using the relation $\mathcal{G}_0(\mathcal{M}_0 - m\omega^2) = 1$ and computing its trace we find

$$1 + \frac{m\omega^2}{d}\text{Tr}\mathcal{G}_0 = \frac{k_{\text{eff}}z}{d}\hat{\boldsymbol{r}}_{ij}^T\cdot\Big(\left(\langle i| - \langle j|\right)\mathcal{G}_0\left(|i\rangle - |j\rangle\right)\Big)\cdot\hat{\boldsymbol{r}}_{ij} \tag{A.18}$$

which corresponds to the final result obtained by Feng and Thorpe [32], except for the sign convention of the Green's function. Following [40] we set $\mathrm{Tr}\mathcal{G}_0 = G_{11}$, giving the magnitude of the site-diagonal Green's function. We can then combine the last two equations to obtain a simplified expression for G_{11} as

$$m\omega^2 G_{11} + 1 = \frac{k_{\mathrm{eff}}}{p^*}\left(\frac{k_{\mathrm{eff}} - pk}{k_{\mathrm{eff}}(k - k_{\mathrm{eff}})}\right) \tag{A.19}$$

where $p^* = 2d/z$ and which is now in a suitable form to be used for the numerical evaluation of G_{11} [40]. For the present purposes, we note that the Green's function G_{11} is given by

$$G_{11}(\omega^2, k_{\mathrm{eff}}) = \frac{1}{2mN}\sum_{\boldsymbol{k},i}\frac{1}{\omega^2 - \omega_i^2(\boldsymbol{q})} \tag{A.20}$$

where the $\boldsymbol{q}$-sum runs over the first Brillouin zone and i-sum over the branches of the dispersion relation of the underlying crystal obtained from as the eigenfunctions of the corresponding dynamical matrix. Finally the vibrational density D_{CPA} of states is obtained by the relation [40]

$$D_{\mathrm{CPA}}(\omega^2, k_{\mathrm{eff}}) = -\frac{1}{\pi}\mathrm{Im}G_{11}(\omega^2, k_{\mathrm{eff}}). \tag{A.21}$$

A.2 CPA for the three-dimensional fcc crystal

In order to quantitatively study the effective medium theory in the case for the 3D FCC we need to write down the dynamical matrix for the perfect FCC and determine the eigenfunctions $\omega_i^2(\boldsymbol{k})$. To keep the notation clean we set the spring constant, mass and lattice spacing to 1, i.e. $k = m = a = 1$. The resulting 3×3 dynamical matrix $\mathcal{D}$ is given

in terms of its components by

$$\begin{aligned}
\mathcal{D}_{11} =& -2\left(\cos\left(\frac{q_x}{2}\right)\left(\cos\left(\frac{q_y}{2}\right)+\cos\left(\frac{q_z}{2}\right)\right)-2\right)\\
\mathcal{D}_{22} =& -2\left(\cos\left(\frac{q_y}{2}\right)\left(\cos\left(\frac{q_x}{2}\right)+\cos\left(\frac{q_z}{2}\right)\right)-2\right)\\
\mathcal{D}_{33} =& 4-2\cos\left(\frac{q_z}{2}\right)\left(\cos\left(\frac{q_x}{2}\right)+\cos\left(\frac{q_y}{2}\right)\right)\\
\mathcal{D}_{12} =& \mathcal{D}_{21}=2\sin\left(\frac{q_x}{2}\right)\sin\left(\frac{q_y}{2}\right)\\
\mathcal{D}_{13} =& \mathcal{D}_{31}=2\sin\left(\frac{q_x}{2}\right)\sin\left(\frac{q_z}{2}\right)\\
\mathcal{D}_{23} =& \mathcal{D}_{32}=2\sin\left(\frac{q_y}{2}\right)\sin\left(\frac{q_z}{2}\right).
\end{aligned}$$

By diagonalizing $\mathcal{D}$ we can compute the three branches $\omega_i^2(\boldsymbol{q},k)$ of the dispersion relation. In order to solve the EMT equations (A.19) and (A.20) we replace the spring constant k in the dispersion relation with the spring constant of the effective medium k_{eff}. Since we need to solve (A.19) and (A.20) iteratively, we use $k_{\text{eff}}=1+i$ as a starting value. Then we compute the effective-medium Green's function$G_{11}(\omega^2,k_{\text{eff}}=1+i)$ by numerically summing the three branches of the dispersion relation over 10^5 points in the first Brillioun zone of the fcc crystal. The resulting Green's function is then substituted in Eq. (A.19) to obtain the new value for the effective spring constant k_{eff}. This process is repeated until convergence of k_{eff} reached, which happens after about 10 iterations.

Appendix B

The inversion-symmetry breaking parameter

Here we follow the exposition [67], which provides an argument for the normalisation of the ISB parameter. We start from a system with an arbitrary distribution of angles θ and ϕ (here they are the angles of the bonds with respect to some reference system - not the angles between bonds in the system). The only thing we can say in the framework of the affine force field is that for every bond vector $\hat{n}_{ij}$ exists a vector $\hat{n}_{ji} = -\hat{n}_{ij}$ appearing with the same relative frequency. We now write the general expression of $|\boldsymbol{\Xi}|^2$ as

$$|\boldsymbol{\Xi}|^2 \;=\; \kappa^2 r_0^2 \sum_i \sum_\alpha \left(\sum_{j\,nn\,i} \hat{n}_{ij}^\alpha \hat{n}_{ij}^x \hat{n}_{ij}^y \right)^2 \tag{B.1}$$

where $\alpha = x, y, z$ are the Cartesian coordinates. We can carry out those sums and regroup the terms to get

$$\begin{aligned} |\boldsymbol{\Xi}|^2 \;=\; \kappa^2 r_0^2 \Bigg(& \sum_{ij} \left(\hat{n}_{ij}^x \hat{n}_{ij}^y \right)^2 \\ & + \sum_i \sum_{k,l\,nn\,i} (\hat{n}_{ik} \cdot \hat{n}_{il})(\hat{n}_{ik} \cdot \hat{n}_{il})^x (\hat{n}_{ik} \cdot \hat{n}_{il})^y \Bigg) \end{aligned} \tag{B.2}$$

Now we implement the difference between the most random configuration, which we call isotropic in the case of the random network, and any other configuration that we want to calculate the ISB parameter for.

With no further restrictions, the second term in (B.2) is zero. We can explain this by the fact that, as said before, the probability to have any vector according to a given

angle distribution is equal to the probability to have the negative of this vector. In the framework of the scalar product this means that

$$\begin{aligned} & P((\hat{n}_{ik}\cdot\hat{n}_{il})(\hat{n}_{ik}\cdot\hat{n}_{il})^x(\hat{n}_{ik}\cdot\hat{n}_{il})^y) \\ & \qquad = \\ & P(-(\hat{n}_{ik}\cdot\hat{n}_{il})(\hat{n}_{ik}\cdot\hat{n}_{il})^x(\hat{n}_{ik}\cdot\hat{n}_{il})^y) \\ & \Rightarrow \langle(\hat{n}_{ik}\cdot\hat{n}_{il})(\hat{n}_{ik}\cdot\hat{n}_{il})^x(\hat{n}_{ik}\cdot\hat{n}_{il})^y\rangle \;=\; 0 \end{aligned} \tag{B.3}$$

In a hard sphere system we would have the restriction that $\hat{n}_{ik}\cdot\hat{n}_{il} < 0.5$ since two bonds from an atom i cannot have an angle smaller that $\pi/3$. This shifts the average in (B.3) to a negative value and lowers $|\boldsymbol{\Xi}|^2$. This also is the core mechanism of the ISB parameter. So what remains of $|\boldsymbol{\Xi}|^2$ in the total random case is

$$|\boldsymbol{\Xi}|^2_{\text{random}} \;=\; \kappa^2 r_0^2 \sum_{ij}\left(\hat{n}^x_{ij}\hat{n}^y_{ij}\right)^2. \tag{B.4}$$

So the ISB parameter becomes

$$F_{IS} \;=\; 1 \;-\; \frac{|\boldsymbol{\Xi}|^2}{\kappa^2 r_0^2 \sum_{ij}\left(\hat{n}^x_{ij}\hat{n}^y_{ij}\right)^2} \tag{B.5}$$

which reproduces the right behaviour of the ISB parameter. When we combine (B.5) and (B.2) we can get an even further simplified expression

$$\begin{aligned} F_{IS} \;&=\; -\frac{\sum_i \sum_{k,l\,nn\,i}(\hat{n}_{ik}\cdot\hat{n}_{il})(\hat{n}_{ik}\cdot\hat{n}_{il})^x(\hat{n}_{ik}\cdot\hat{n}_{il})^y}{\sum_{ij}\left(\hat{n}^x_{ij}\hat{n}^y_{ij}\right)^2} \\ &=\; -\frac{\sum_i \sum_{k,l\,nn\,i}\,\cos\alpha_{kl}\,(\hat{n}_{ik}\cdot\hat{n}_{il})^x(\hat{n}_{ik}\cdot\hat{n}_{il})^y}{\sum_{ij}\left(\hat{n}^x_{ij}\hat{n}^y_{ij}\right)^2}, \end{aligned} \tag{B.6}$$

where we have linked the inversion symmetry breaking parameter to the angular distribution of the angles α_{kl} between bonds in each cell of the system.
But one problem remains: We have defined our ISB parameter in the framework of xy shearing. So we weighted the symmetry in the xy plane higher than the symmetry in the other directions. To get a general parameter we have to include the other directions, represented by their corresponding affine force fields, as well. So we replace

$|\boldsymbol{\Xi}|^2 = \sum_{a,b=x,y,z} |\boldsymbol{\Xi}_{ab}|^2$. Therefore equation (B.4) and the numerator of (B.6) becomes

$$
\begin{aligned}
|\boldsymbol{\Xi}|^2_{\text{random}} &= \kappa^2 r_0^2 \sum_{ij} \sum_{ab} \left(\hat{n}^a_{ij} \hat{n}^b_{ij}\right)^2 \\
&= \kappa^2 r_0^2 \sum_{ij} \left(\left(\hat{n}^x_{ij}\right)^2 + \left(\hat{n}^y_{ij}\right)^2 + \left(\hat{n}^z_{ij}\right)^2 \right)^2 \\
&= NZ\kappa^2 r_0^2 \sum_{i} \sum_{k,l\,nn\,i} \sum_{ab} (\hat{n}_{ik} \cdot \hat{n}_{il})(\hat{n}_{ik} \cdot \hat{n}_{il})^a (\hat{n}_{ik} \cdot \hat{n}_{il})^b \\
&= \sum_{i} \sum_{k,l\,nn\,i} (\hat{n}_{ik} \cdot \hat{n}_{il}) \left((\hat{n}_{ik} \cdot \hat{n}_{il})^x + (\hat{n}_{ik} \cdot \hat{n}_{il})^y + (\hat{n}_{ik} \cdot \hat{n}_{il})^z \right)^2 \\
&= \sum_{i} \sum_{k,l\,nn\,i} (\hat{n}_{ik} \cdot \hat{n}_{il})^3
\end{aligned}
$$

The ISB parameter therefore becomes

$$
F_{IS} = -\frac{1}{NZ} \sum_{i} \sum_{k,l\,nn\,i} (\hat{n}_{ik} \cdot \hat{n}_{il})^3 = -\frac{1}{NZ} \sum_{i} \sum_{k,l\,nn\,i} (\cos \alpha_{kl})^3 \tag{B.7}
$$

It is important to notice that we count each angle twice. Due to the restriction $\cos \alpha_{kl} < 0.5$, the value $\langle (\cos \alpha_{kl})^3 \rangle$ is smaller than 1. So the sign of (B.7) is correct to produce a parameter $F_{\text{IS}} < 1$.

Appendix C

Dispersion relation of the linear chain with long-range interaction

We expect that there will be significant changes in the physics of a lattice dynamical system when interaction is extended from a mere nearest-neighbor interaction to long-range interactions. To obtain some insights, we will now compare the well-studied case of a linear chain with long-range interactions to the construction of the shelled triangular lattice.

Following the discussion in Ref. [4], we can define a linear chain with long-range interaction given by the harmonic potential energy

$$H_{\mathrm{LR}} = \sum_i \sum_n \kappa_n \Big[u(ia) - u((i+n)a)\Big]^2 \tag{C.1}$$

where the summation over the index i extends over the sites on the linear chain and the summation over n specifies the range of the long-range interaction and a is the nearest-neighbour distance. We choose a power-law dependence for the scaling of the distance-dependent spring constant, i.e. $\kappa_n = n^{-\alpha}$. We are interested in understanding the behaviour of the dispersion relation $\omega = \omega(q)$ when changing both the range and scaling exponent α of the interaction in the linear chain.

Let us first look at the dependence of the dispersion relation on the scaling exponent α. For this we plot $\omega(q)$ for a interaction distance of $n = 10^4$ for $\alpha = 2$ and $\alpha = 3$.

From Fig. C.1 we can observe that changing the exponent of the power-law of κ_n from 2 to 3 globally pushes the dispersion curve to lower values in the whole Brillouin zone, which is accompanied by a clear change of scaling in the low-momentum region of $\omega(q)$.

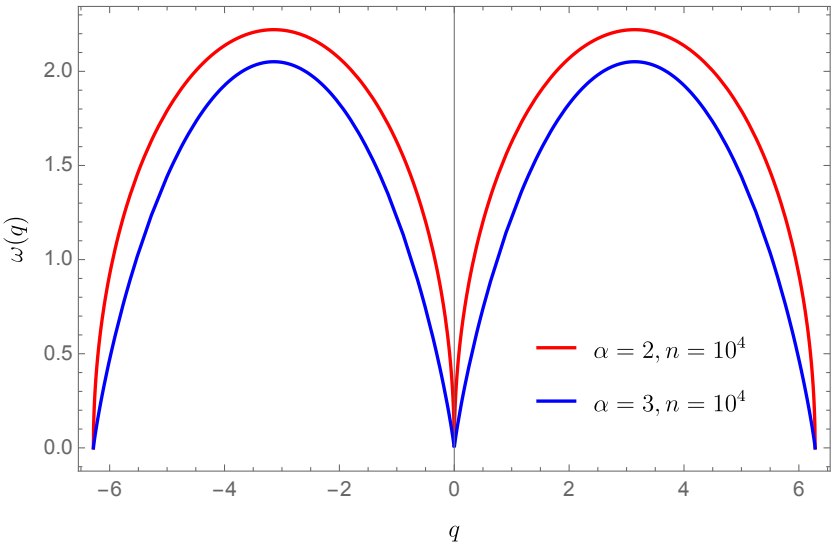

Fig. C.1 Shown are the dispersion relations $\omega(q)$ of the linear chain with long-range interaction up to the distance $10^4 a$ for two different exponents of the power-law decay of the interaction strength.

Turning to the behaviour of the dispersion relation when changing the range of the interaction κ_n, it becomes obvious that in the case of cubic decay the convergence to the asymptotic case is happening much faster than in the case of the squared decay.

In the case where $\alpha = 2$, it is possible to easily obtain a closed-form solution for the dispersion relation. Solving the equation of motion of the long-range linear chain we obtain the dispersion relation as [4]

$$\omega(q) = \left(\sum_{n>0} \frac{1}{n^p} \sin\left(\frac{qan}{2} \right)^2 \right)^{1/2} \tag{C.2}$$

$$= \left(\sum_{n>0} \frac{1}{2n^p} \left(1 - \cos\left(qan\right)\right) \right)^{1/2} . \tag{C.3}$$

2 In the case where $p = 2$ we can use the identity

$$\sum_{n>0} \frac{1}{n^2} \left(1 - \cos\left(qan\right)\right) = \frac{1}{4} \left(\pi^2 - (q - \pi)^2 \right), \tag{C.4}$$

(see Ref. [47] for a detailed proof) to express the dispersion relation as

$$\omega(q) = \sqrt{\frac{\pi^2 - (q - \pi)^2}{2}} \tag{C.5}$$

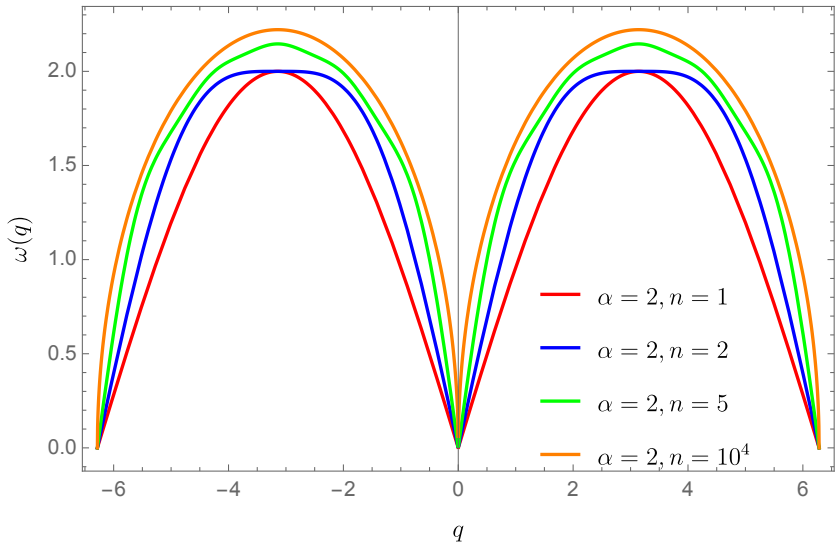

Fig. C.2 Comparison of the linear chain dispersion relation for fixed power-law exponent $\alpha = 2$ but for variable interaction range.

The closed form expression for general exponents p can't be obtained as easily. For this reason we will stick to the analysis of the behaviour at low values of q. First, consider the previous case of $p = 2$. In the low q-region, we transform the sum into an integral and subsequently obtain

$$\int_1^\infty \frac{1-\cos(qn)}{n^2} = 1 + \frac{\pi\,|q|}{2} - q\mathrm{Si}(q) - \cos(q) \tag{C.6}$$

where $\mathrm{Si}(k)$ denotes the Sine-integral. Expanding to linear order we get the asymptotic scaling of the dispersion relation as

$$\omega(q)\Big|_{\mathrm{p=2}} \sim \sqrt{\frac{\pi\,|q|}{2}}. \tag{C.7}$$

When we set $p = 3$ and transform the infinite sum to an integral we obtain

$$\int_1^\infty \frac{1-\cos(qn)}{n^2} = \frac{1}{2}(q(\sin(q) - q\mathrm{Ci}(q)) - \cos(q) + 1), \tag{C.8}$$

where $\mathrm{Ci}(q)$ is the Cosine-integral. In this case it does not suffice to linear order since the linear approximation of the above expression is identically zero. Hence, expanding

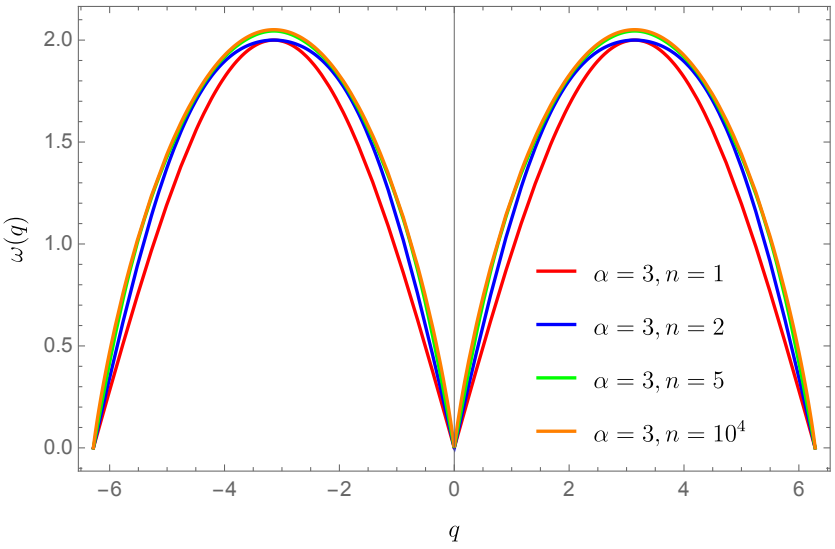

Fig. C.3 Comparison of the linear chain dispersion relation for fixed power-law exponent $\alpha = 3$ but for variable interaction range.

up to second order in q, we obtain the asymptotic scaling

$$\omega(q)\big|_{\mathrm{p}=3} \sim q\sqrt{\frac{3 - 2\gamma - 2\log q}{2}}, \tag{C.9}$$

γ being the Euler-Mascheroni constant.

Appendix D

Viscoelasticity of metallic glasses

D.1 The High-Frequency Shear Modulus in the Continuum Limit

Recalling the derivation in Chapter 1, the evaluation of the complex linear viscoelastic response to the shear modulus in Eq. (1.49) yields

$$G^*(\omega) = G_A + \frac{1}{V}\sum_p \frac{\widehat{\Xi}_p\,\widehat{\Xi}_p}{m\omega^2 - m\omega_p^2 - i\omega\nu}, \tag{D.1}$$

where $\widehat{\Xi}_p$ denotes the affine force field tensor and ω_p the eigenfrequencies of the system. In the continuum limit we can replace the sum over the p-states by an integration over the eigenfrequencies ω_p, that is

$$G^*(\omega) = G_\mathrm{A} + \int_0^{\omega_\mathrm{D}} \mathrm{d}\omega_p \frac{\rho(\omega_p)\Gamma(\omega_p)}{m\omega^2 - m\omega_p^2 - i\omega\nu}, \tag{D.2}$$

where $\rho(\omega_p)$ denotes the density of states and ω_D the Debye frequency. The function Γ represents the correlator on frequency shells given by $\Gamma(\omega) = \langle\widehat{\Xi}_p\,\widehat{\Xi}_p\rangle$, where the average is evaluated for all projections of Ξ on eigenvectors with eigenfrequency $\omega_p \in [\omega, \omega + \mathrm{d}\omega]$. We can express the shell correlator in a simple fashion due to the result in [101] as $\Gamma \sim \omega_p^2$. Also we will assume that the density of states is quadratic as in the Debye model given as $\rho(\omega_p) \sim \omega_p^2$.

Therefore the expression for the complex shear modulus reduces to

$$G^*(\omega) = G_\mathrm{A} + \int_0^{\omega_\mathrm{D}} \mathrm{d}\omega_p \frac{\omega_p^4}{m\omega^2 - m\omega_p^2 - i\omega\nu}. \tag{D.3}$$

Since we are interested in the shear modulus it suffices to consider the real part of the complex quantity G^*. The real part of the integrand above is easily seen to be

$$\frac{2m\omega_p^4\left(\omega^2-\omega_p^2\right)}{m^2\omega^4\left(1+\dfrac{\omega_p^4}{\omega^4}-2\dfrac{\omega_p^2}{\omega^2}\right)}. \tag{D.4}$$

Thus, we observe, that in the high-frequency limit, where $\omega \to \infty$, the above expression will converge to zero, leading to $\lim_{\omega\to\infty} \mathrm{Re}\, G^*(\omega) = G_A$. By virtue of this argument we can substitute the high-frequency shear modulus with the Born-Huang affine shear modulus G_A.

D.2 The Ashcroft-Born-Mayer potential

With the two contributions introduced in the main text, the Ashcroft-Born-Mayer pseudopotential is given by

$$V_{\mathrm{ii}}(r) = \frac{A\,\mathrm{e}^{-q_{\mathrm{TF}}(r-2a_0)}}{r-2a_0} + B\,\mathrm{e}^{-C(r-\bar{\sigma})}, \tag{D.5}$$

where a_0 is the Bohr radius and $\bar{\sigma}$ the average ionic core diameter of the alloy, which corresponds to the average size of the ionized atoms constituting the alloy. The average ionic core diameter is obtained by a averaging the respective ionic core diameter of the constituents with their contributing weights given by their volume ratios in the alloy. The values for the ionic core diameters of the atoms constituting the alloys are taken from Ref. [82]. The quantities A and B set the energy scales for the repulsive interaction from the Ashcroft and Born-Mayer term, respectively. The parameter q_{TF} is the inverse of the Thomas-Fermi screening length given by Thomas-Fermi theory, and its value is known for different types of alloys [93]. We choose a representative value for q_{TF} as $1.25\,\mathring{A}^{-1}$ according to the values reported in Ref. [93]. The ionic core diameter $\bar{\sigma}$ is obtained by a weighted average of the core diameters of the atoms constituting the alloys taken from [82], where the weights correspond to the ratios of the respective atoms.

The characteristic range $1/C$ of the valence-shell overlap repulsion is not known a priori. However, its typical values are less sensitive to the atomic composition than the parameters $\bar{\sigma}$, A and B. Different atoms have very similar values typically in the range $1-2.5\,\mathring{A}^{-1}$ [41].

Finally, A is the prefactor to the Ashcroft pseudopotential, which is the product of the electrostatic nuclear repulsion $Z_{\mathrm{ion}}^2 e^2$ and the Ashcroft factor $\cosh^2(q_{\mathrm{TF}}R_{\mathrm{core}})$ [30],

where R_{core} is a typical value for the atom-specific core radius and Z_{ion} the effective ionic charge number. The latter cannot be easily estimated from first-principles or from literature. Similarly, the prefactor B of the Born-Mayer term, can be rigorously evaluated only from the exchange integrals of the various overlapping electrons which belong to the valence shells of the two interacting ions. This calculation, even in approximate form, is not feasible except for simple crystals. Hence, we take both A and B as adjustable parameters in the mapping between our schematic logarithmic potential and the Ashcroft-Born-Mayer pseudopotential. We shall remark that the Born-Mayer prefactor B typically has non-trivial large variations from element to element across the periodic table, as shown in many ab initio simulations studies [41, 43]. Consistent with this known fact, it turns out that B is the most sensitive parameter in our analysis, in the sense that small variations in B can lead to large deviations in the fitting of the experimental data. Conversely, the Ashcroft prefactor A is not a sensitive parameter, and its values are not crucial for the match with experiments.

D.3 Pseudopotential Fitting

The values of the parameters which have been used to obtain fits to the logarithmic pseudopotential are documented in Table 1 of this Appendix. In Fig. D.1 we plotted a comparison between the Ashcroft-Born-Mayer pseudoptential and the potential of mean force. We see that the repulsive form of the potential of mean force is well approximated by the exponential functional form of the pseudopotential.

The values for both the Thomas-Fermi wave vector q_{TF} and the Pauli exclusion parameter are seen to vary very little for the different alloys. In contrast, the parameters which define the energy scale of the two contributions to the Ashcroft-Born-Mayer potential show a significant variation. Interestingly, this variation correlates with the steepness parameter λ defined earlier. In particular, a increasing values for the steepness λ coincide with an increase in the energy scale, which is defined by both the parameters A and B.

Also, we can deduce from Fig. D.1 and Tab. D.1 that the Born-Mayer term in the pseudopotential provides the dominant contribution to the repulsive effective potential at longer length scales. The screened Coulomb interaction represented by the Ashcroft term only comes into action at distances shorter than the screening length, where the electrostatic repulsion of the ionic core provides a harsh repulsive barrier.

D.4 Comparison of the Born-Mayer parameter with typical values

Our modelling of λ indicates clearly that, of the two contributions, it is the Born-Mayer electron-overlap repulsion the one which controls the qualitative behaviour, while the A parameter does not have much effect on the slope. This implies that the parameters of the Born-Mayer repulsion are those which control the interaction softness. Furthermore, if we recast the Born-Mayer interaction in the canonical form which is found in the molecular physics literature, Be^{-Cr}, for our Zr-based alloy we obtain $B \approx 15000\ eV$ which is not far from the value $B = 22000\ eV$ obtained in simulations of the interaction between two Zr atoms in the literature, e.g. Ref. [1]. This comparison confirms the robustness of our model, not only at the qualitative level, but also in capturing the right orders of magnitude of the microscopic forces. We believe that more detailed calculations using ab-initio methods can be done along this line in future work by ab-initio molecular dynamics specialists.

D.5 Cooperative shear events

The constitutive equation for the viscosity presented in the main text is based on the shoving model of glasses [26, 25]. The key idea behind this is that the interatomic repulsion is strong compared to the attractive forces. In a plastic flow event many atoms need to rearrange, which at constant volume has the consequence that the atoms involved are forced together [25]. Since this process is energetically unfavourable, it was suggested that the atoms may shove aside their neighbours to create free volume and accommodate the flow process.

It can be shown that the energy necessary to trigger a shoving event in a volume V is linearly proportional to the high-frequency shear modulus, with the constant of proportionality being the characteristic volume V_c, i.e. $E(T) = G_{\mathrm{A}}(T)V_c$ [25].

According to Ref. [48], the total energy barrier W between two basins in the potential energy landscape is given by $W = \frac{8}{\pi^2} G_{\mathrm{A}}\, \Omega \gamma_C^2 \xi$, where Ω represents the effective STZ volume and G_{A} the shear modulus. The critical shear strain γ_C is found be 0.036 ± 0.002 for all known metallic glasses and the correction factor ξ due to the matrix confinement of a STZ ranges between 2 and 4 [48]. After evaluating the expression for the potential energy barrier we get $W \approx (1/320)\, G_{\mathrm{A}}\Omega$. We assume that the energy barrier W in the cooperative shear model is approximately equal to the shoving energy, that is $W \approx E$. It directly follows that $G_{\mathrm{A}}V_c \approx (1/320) G_{\mathrm{A}}\Omega$, which leads us to conclude that the effective

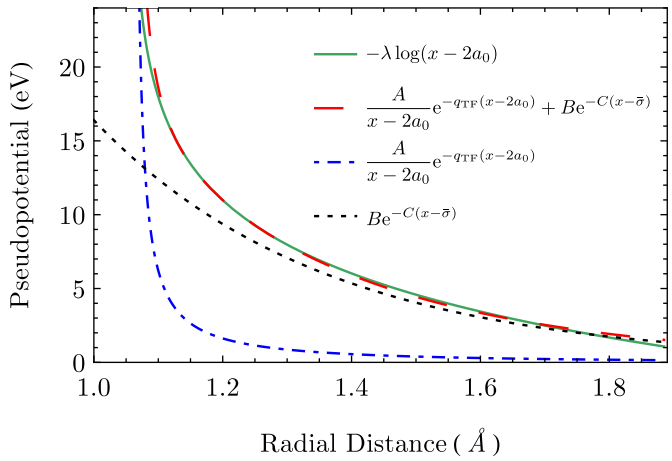

Fig. D.1 Comparison of the Ashcroft-Born-Mayer pseudopotential with the logarithmic potential of mean force (including the two separate contributions to the pseudopotential). The plot was generated for a repulsive steepness $\lambda = 99.7$.

Table D.1 Values used for the fitting of the Ashcroft-Born- Mayer pseudopotential to the logarithmic potential of mean force

λ	A (eV)	q_{TF} ($\mathring{A}^{-1}$)	B (eV)	C ($\mathring{A}^{-1}$)	$\bar{\sigma}$ ($\mathring{A}$)
196.2	0.37	1.7	5.1	2.8	1.68
276.4	0.39	1.7	21.8	2.8	1.29
286.5	0.42	1.7	28.8	2.8	1.20
381.2	0.48	1.7	57.4	2.8	1.056

volume of a STZ is $\Omega \approx 320 V_c$. It is physically meaningful that the effective STZ volume Ω is approximately equivalent to the initial shoving volume V, henceforth calling it V_{STZ}. Using the identification $\Omega \approx V_{\mathrm{STZ}} \approx 320 V_c$ together with Eq. (8) from the main text, we obtain a relation between the activation volume and the characteristic volume V_c given by $\Delta V \approx \sqrt{480}\, V_c$.

As explained in the main text, we use the characteristic volumes V_c from the viscosity fitting in the relation above to compare the resulting theoretical values for the STZ volume to experimental data.